MASTER THESIS

Modelling of batch-wise operation of European Sodium Fast Reactor and Breed&Burn Molten Salt Reactor

Valeria RAFFUZZI

Supervisors:
Dr. Jiří KŘEPEL
Dr. Konstantin MIKITYUK

Professor:
Prof. Horst-Michael PRASSER

A thesis submitted in fulfilment of the requirements of the Master degree in Nuclear Engineering

offered by

ETH Zürich - EPF Lausanne

Zürich, November 7, 2019

Abstract

Paul Scherrer Institute
Advanced Nuclear Systems

Master degree in Nuclear Engineering

Modelling of batch-wise operation of European Sodium Fast Reactor and Breed&Burn Molten Salt Reactor

by Valeria RAFFUZZI

The Generation IV International Forum promotes six advanced nuclear systems which could improve the fuel cycle sustainability. Two of these are the Sodium Fast Reactor and the Molten Salt Reactor, fast-spectrum designs which could be operated in batches and converge to an equilibrium state. The equilibrium fuel cycle is a useful reference to evaluate and compare the neutronic performances of different systems. The goal of this work is to contribute to model the equilibrium fuel cycle of the two Generation-IV systems mentioned above with focus on the development of efficient fast-running tools. Both of the systems are simulated in an open cycle with fixed fresh fuel composition and batch-wise refuelling. The applications of this work concern the evaluation of a radially infinite Serpent model of the European Sodium Fast Reactor (ESFR) and a parametric study aimed at reducing the dimensions of a Breed and Burn Molten Salt Reactor (MSR). The tool employed and extended is a Python based script, called Batch Burnup Procedure, applicable to both solid and liquid fuel systems. This routine calls the Monte Carlo code Serpent2 for burnup and transport simulations, and can automatize batch-wise refuelling by manipulating Serpent input and output files until equilibrium is reached. The reduced infinite ESFR model can reproduce precisely some features of the ESFR inner fuel region. To produce fine safety feedbacks maps of the core, however, extremely high statistics must be implemented to overcome the strong stochastic noise. In this work, Breed and Burn batch-wise operation was proven to be feasible for a U-Pu Chloride fuelled MSR if non-soluble fission products removal is adopted. The core dimensions were largely reduced by implementing a multi-fluid layout.

Contents

Abstract **iii**

1 Introduction **1**
1.1 Generation IV International Forum 1
1.1.1 SFR 2
1.1.2 MSR 2
1.2 Batch-wise reactor operation 2
1.3 Equilibrium state and simulation 3
1.3.1 EQL3D - ERANOS 3
1.3.2 EQL0D - Serpent 3
1.3.3 BBP - Serpent 4
1.4 Aim of the Thesis 4

2 Simulation Tools Applied **7**
2.1 Serpent 7
2.2 BBP - Batch Burnup Procedure 7
2.2.1 Burnup calculation 8
2.2.2 Safety parameters calculation 8

3 Application to European Sodium Fast Reactor **11**
3.1 European Sodium Fast Reactor 11
3.2 ESFR inner fuel reduced model 12
3.3 Batch-wise operation simulation 13
3.3.1 Transition towards equilibrium cycle 14
3.3.2 Comparison with full-core model results 18
3.4 Doppler Constant and Sodium Void Effect 21
3.4.1 Safety parameters evolution towards EOEC 23
3.4.2 Safety parameters mapping at EOEC 26
Doppler constant 26
Sodium void effect 29
3.4.3 Number of neutron histories and stochastic error . . . 31

4 Application to Breed & Burn Molten Salt Reactor **37**
4.1 Molten Chloride Fast Reactor 37
4.1.1 Breed & Burn fuel cycle 37
4.2 MCFR batch-wise operation model 39
4.3 Cell-level simulation 41
4.3.1 Fuel salt types 42
4.3.2 Non-soluble fission products removal strategy 43
4.3.3 Non-soluble fission products removal frequency 45

4.4 Core-level simulation 47
4.4.1 Minimal critical core dimensions 48
4.4.2 Two-fluid layout 50
4.4.3 Multi-fluid layout 55
4.4.4 Impact of moderation 55
4.4.5 Impact of refuelling strategy 58
4.5 Safety parameters evaluation 59

5 Summary and Conclusions **63**
5.1 Outlook 65

Acknowledgements **67**

A ESFR fertile blanket discretization **69**

B Behaviour of ESFR core periphery **71**

C ESFR safety parameters normalization **75**

D ESFR safety parameters mapping **77**
D.1 Doppler constant 78
D.2 Sodium void effect 80

Bibliography **85**

List of Abbreviations

ANS	**A**dvanced **N**uclear **S**ystems
B&B	**B**reed and **B**urn
BBP	**B**atch **B**urnup **P**rocedure
BOC	**B**eginning **O**f **C**ycle
BOL	**B**eginning **O**f **L**ife
CE	**C**onstant-**E**xtrapolation
CRAM	**C**hebyshev **R**ational **A**pproximation **M**method
EOC	**E**nd **O**f **C**ycle
BOEC	**B**eginning **O**f **E**quilibrium **C**ycle
EOEC	**E**nd **O**f **E**quilibrium **C**ycle
ESFR	**E**uropean **S**odium **F**ast **R**eactor
FIMA	**F**issions per **I**nitial **M**etal **A**tom
FP	**F**ission **P**roducts
GIF	**G**eneration IV **I**international **F**orum
IF	**I**nner **F**uel
LE	**L**inear-**E**xtrapolation
LE/LI	**L**inear-**E**xtrapolation **L**inear-**I**nterpolation
MCFR	**M**olten **C**hlorides **F**ast **R**eactor
MOX	**M**ixed **OX**ide
MSR	**M**olten **S**alt **R**eactor
OF	**O**uter **F**uel
ScRB	**S**emi-continuous **R**efuelling **B**urnup
SFR	**S**odium **F**ast **R**eactor
SMART	**S**afety **M**easures **A**ssessment and **R**esearch **T**ools
SPX	**S**uper**P**heni**X**
ULOF	**U**nprotected **L**oss **O**f **F**low

Chapter 1

Introduction

1.1 Generation IV International Forum

In January 2000, a group of governmental representatives from nine countries gathered to give birth to the Generation IV International Forum (GIF) [1]. The GIF aims at the institution of an international collaboration targeted at the research and development of six advanced nuclear systems, shown in Figure 1.1. Those reactor concepts have been selected among many since they are promising with respect to the goals set by the GIF:

- Sustainability
- Economics
- Safety and Reliability
- Proliferation Resistance and Physical Protection

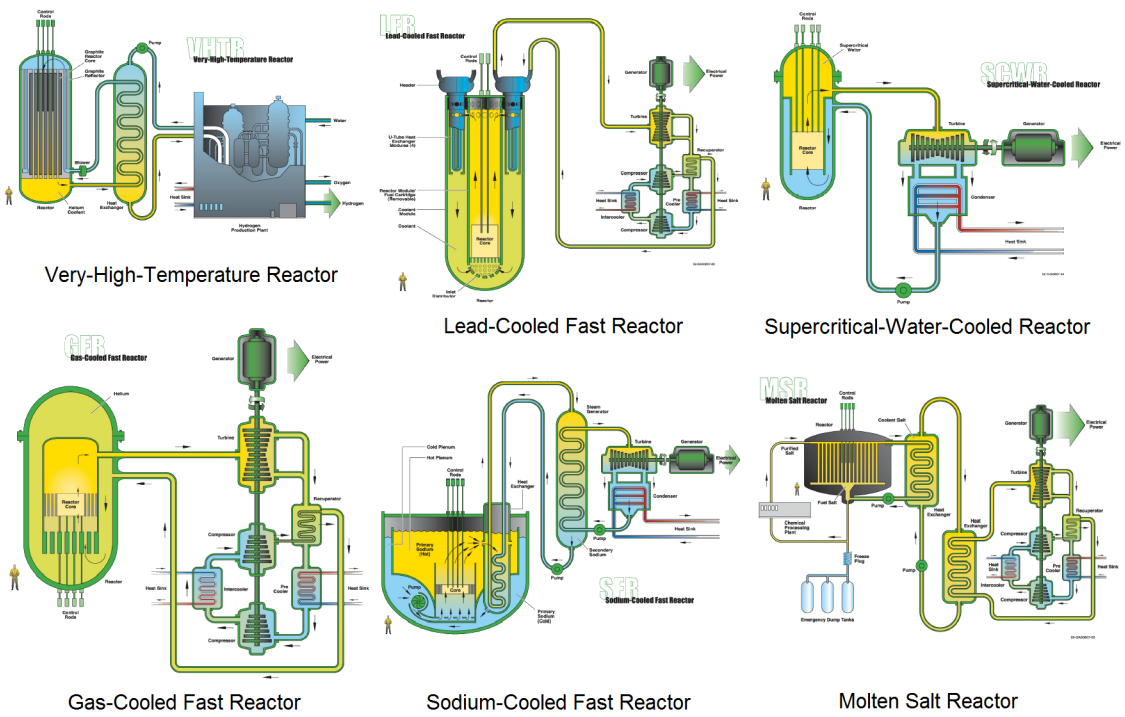

FIGURE 1.1: Six Generation IV nuclear reactor concepts

This Master Thesis focuses on two of the GIF systems, namely the Sodium Fast Reactor (SFR) and the Molten Salt Reactor (MSR), coherently with the research carried out in the Advanced Nuclear Systems (ANS) group at Paul Scherrer Institute (PSI). These reactors are promising in terms of fuel cycle sustainability, since they have the possibility to operate in a closed fuel cycle. Additionally, the fast neutron energy spectrum allows to achieve a high breeding ratio, thus fuel utilization could be further increased [2].

1.1.1 SFR

The Sodium Fast Reactor is the most developed between the Generation IV reactors [3]. It employs liquid sodium as a coolant, which is neutronically favourable since it is a weak neutron absorber and moderator. The high conductivity of sodium guarantees effective cooling and high thermal inertia. The use of liquid sodium allows low pressure operation, since its boiling temperature is 883°C. However, SFR normally has a positive sodium void worth, which can be compensated for with an appropriate design. Furthermore, special precautions are needed to prevent sodium leaks from the primary circuit, because of the high chemical reactivity of sodium with water and air. The SFR can operate in both an open or closed fuel cycle. Operation in a closed cycle mode is achieved when reprocessed fuel, such as MOX, is utilized.

1.1.2 MSR

The Molten Salt Reactor is an old concept, introduced in the 1940s when the Aircraft Reactor Experiment was initiated at Oak Ridge National Laboratory [4]. However, due to its complex and revolutionary features, MSR is not highly developed. In particular, there is a lack of research and expertise concerning chlorides fuelled MSR. Fluoride salts, on the other side, have been investigated more. MSR with liquid fuel is an innovative concept: it allows low pressure operation and online and offline fuel reprocessing. At the same time, fuel assemblies fabrication would be unnecessary. MSR guarantees a large fuel cycle flexibility, since it could operate as a breeder in both Uranium and Thorium fuel cycle [5]. On the other hand, molten salts are highly corrosive, therefore materials which combine good corrosion-resistance and mechanical strength, such as the nickel alloy Hastelloy, must be developed.

1.2 Batch-wise reactor operation

Refuelling between operation cycles is necessary to replace depleted fuel, poisoned by fission products, with fresh fuel. Refuelling can take place either continuously or batch-wise. Most of the Generation IV reactors (SFR, LFR, VHTR and SWCR) operate with solid fuel assemblies, thus refuelling can take place only batch-wise. HTR fuel is in the form of graphite pebbles

which are replaced from the core with high frequency, in a roughly continuous mode [6]. In the case of MSR with liquid fuel, refuelling can take place in both ways.
A reactor which operates with batch-wise refuelling, after many years of unaltered operation, experiences a transition from an initial fuel composition to an equilibrium one [7]. According to the fuel feed, which could be fresh or reprocessed, the equilibrium cycle is respectively open or closed. In this work, SFR and MSR are simulated with batch-wise refuelling in an open fuel cycle with fixed fresh fuel composition, until they reach equilibrium.

1.3 Equilibrium state and simulation

The equilibrium state can be achieved if a periodic reloading scheme is applied. At equilibrium core parameters such as reactivity, fuel burnup, fuel composition and safety parameters remain constant from one cycle to another. Studying the equilibrium state of a reactor can give useful information about its long-term operation, and allows the comparison of different systems in their steady state. For example in [8] sixteen reactor designs, eight fast and eight thermal, were compared with the equilibrium method [9]. At PSI, three numerical tools were developed to evaluate the performances of disparate systems after their convergence to equilibrium. These procedures are namely EQL3D (2008), EQL0D (2018) and BBP (2018).

1.3.1 EQL3D - ERANOS

EQL3D is a numerical tool created at PSI, whose name stands for "Equilibrium fuel cycle procedure for fast reactors" [7]. It is coded into ERANOS environment, and it is able of solving the equilibrium condition of both closed and open fuel cycles [10]. It was specifically designed to account for complex multi-batch fuel reloading schemes, including for example fuel reshuffling and reprocessing. Compared to previous tools, mainly relying on point models or simplified homogeneous 2D geometries [11], EQL3D has the advanced capability to model 2D r-z and 3D hexagonal-z geometries. The mathematical formulation of the fuel evolution, based on the matrix form of the Bateman equation, proved that the equilibrium fuel vector only depends on the feed composition and on the transition matrix; however, several iterations are needed to reach the equilibrium state.

1.3.2 EQL0D - Serpent

The second tool, EQL0D, is a zero-dimensional depletion code applicable to fluid fuel cores, treated as homogeneous. The code was created, in particular, in view of MSR simulations. It is coded in Matlab and it internally calls the Monte Carlo code Serpent for cross-sections calculations. Fuel depletion is computed solving the Bateman equation, where refuelling and non-soluble

fission and decay products removal appear as respectively positive and negative terms. The addition of nuclides, according to the user's preferences, can be used to control the total actinides mass, reactor criticality or redox potential for corrosion purposes. The code can support two types of calculations: the search for equilibrium, which ends when convergence is reached, or the time dependent fuel evolution. In both cases, the algorithm consists of two loops: an outer loop, in which Serpent computes the microscopic cross-sections and the reaction rates, and an inner loop coded in Matlab, where the depletion equation is solved [5].

1.3.3 BBP - Serpent

The tool extended and utilized in this work is a versatile routine which, coupled with the Monte Carlo code Serpent 2, can be applied to simulate neutronic aspects of different systems. The routine is called Batch Burnup Procedure (BBP) and is coded in Python language. It is complementary to Serpent since it introduces the possibility to simulate batch-wise refuelling and fuel reshuffling between consecutive operation cycles. Originally, the code was created at PSI in Ruby language, and it was named Semi-continuous Refuelling Burnup (ScRB). The first application concerned the pebble-bed reactor HTR-PM [12]. Afterwards, it has been translated in Python and adapted for the application to solid fuel reactors, as well as renamed Batch Burnup Procedure [13]. For this work, the routine was extended to include the application to homogeneous liquid fuel reactors and safety coefficients mapping.

1.4 Aim of the Thesis

The aim of this Thesis was, in first place, to use and extend the BBP code, a versatile tool which can be utilized to study the equilibrium state of solid and liquid fuel systems.
The applications of the BBP routine concerns the two fast reactors mentioned above. The first system is a European technology, the European Sodium Fast Reactor (ESFR), developed by a consortium of research centres and companies. This Thesis is a contribution to ESFR-SMART, a Horizon2020 project, whose main goal is the assessment of the enhanced safety of the concept through experiments and modelling. Batch-wise operation of the full-core ESFR has been previously simulated with Serpent [14]. In this Thesis, a reduced model of the ESFR inner core has been simulated through the BBP routine. The use of a reduced model could allow to adopt higher statistics, enhancing the precision of the results while maintaining a reduced computational resources utilization. Additionally, a finer axial nodalization of the fuel assemblies could be implemented. To assess the precision of the ESFR reduced model utilized, its results were compared with those of full core models developed at PSI.
The second system studied is a Breed and Burn (B&B) Molten Chloride Fast Reactor (MCFR). This reactor has been analysed in previous works, where a

continuous refuelling mode was adopted [5] [15] [16]. In this Thesis, batch-wise refuelling is implemented. B&B is a sustainable operation mode which could be applied to any fast system with an open once through cycle. The feed is fertile fuel, and the reactor itself breeds the fissile material burnt during operation. To realize such operation mode, the neutron economy must be excellent and neutron leakage outside of the reactor must be limited. A core of considerable size could compensate the losses due to neutron leakage; however, it would be unpractical and a too large fuel inventory is undesirable. Therefore, a geometry optimization has been carried out in order to reduce the size of a B&B MCFR core.

Chapter 2

Simulation Tools Applied

In this work the two reactors simulated are brought to equilibrium, where their performance is analysed. For this purpose, a Python-based routine named Batch Burnup Procedure and developed at PSI was utilized. Such routine was coupled with the Monte Carlo code Serpent2, used to perform burnup and transport simulations.

2.1 Serpent

Serpent is a Monte Carlo reactor physics code developed by Jaakko Leppanen for VTT Technical Research Centre of Finland and released in October 2008 [17]. It is suitable for high precision transport and burnup calculations thanks to the continuous energy cross-sections structure. In Serpent, the material depletion matrix is solved by the Chebyshev Rational Approximation Method (CRAM) [18], and several Predictor-Corrector schemes may be applied [19]. However, good statistics come at the cost of a very high number of neutrons simulated, hence elevated CPU time. This is particularly true in the case of large systems with complex geometries. Very good statistics are also required for the study of local properties of large systems: as a consequence, Serpent is unsuitable for this type of calculations in favour of deterministic codes.
In this work, ENDF/B-VII.0 nuclear data libraries were consistently used. The Predictor-Corrector scheme adopted when high precision results were required is Linear-Extrapolation/ Linear-Interpolation (LE/LI) with three time substeps. As an alternative Linear-Extrapolation (LE), which is less memory consuming, was applied. In any case, both LE/LI and LE were proven to perform better than the traditional Constant-Extrapolation (CE) scheme [20][21].

2.2 BBP - Batch Burnup Procedure

To converge to an equilibrium state, a reactor must operate for long term under repetitive conditions. This can be achieved by applying a periodic fuel reloading pattern. To simulate the transition from initial to equilibrium state, an external routine had to be coupled to Serpent. Such procedure was named BBP. With respect to the original version, which allowed burnup calculations

in case of solid fuel reactors, the BBP was extended to include the application to liquid homogeneous fuel reactors and safety coefficients calculation.

2.2.1 Burnup calculation

The goal of the BBP script is to automatize batch-wise refuelling. The algorithm of the routine is schematized in Figure 2.1. At the beginning of each cycle, the routine manipulates the input files for the Serpent simulation. In particular, the main input file is completed by overwriting some of the input parameters like number of neutrons, active and inactive cycles number and burnup time steps. The material input file, which contains the fuel material cards, is also prepared: the fuel composition is copied from the output of the previous cycle simulation. Then, in the solid fuel case, the most burnt fuel is identified and substituted with fresh fuel. In the homogeneous liquid fuel case, a volumetric share of the fuel is removed and the same volume of fresh feed is added. In the next step, the routine calls Serpent to run the burnup calculation. The whole process is repeated for as many cycles as requested by the user. As a final step, the outputs from every cycle are processed and arranged in more compact output files, suitable for transferring data to Excel.

2.2.2 Safety parameters calculation

The capabilities of the BBP functions to manipulate Serpent inputs were further utilized for the calculation of reactivity feedbacks. In this work, Doppler constant and sodium void effect were calculated for ESFR. For MSR Doppler effect, fuel density effect and combined temperature and density effect were calculated. Safety parameters were computed by direct calculations, i.e. comparing the nominal state with a perturbed state:

$$\Delta\rho = \rho_{perturbed} - \rho_{nominal} \tag{2.1}$$

where $\Delta\rho$ is the reactivity effect and ρ is the core reactivity in the perturbed or unperturbed case. In the case of the Doppler constant for fast neutron energy spectra, the reactivity difference has a logarithmic dependence on the ratio between perturbed and unperturbed temperatures:

$$KD = \frac{\rho_{perturbed} - \rho_{nominal}}{ln(\frac{T_{perturbed}}{T_{nominal}})} \tag{2.2}$$

where KD is the Doppler constant and T is the fuel temperature in Kelvin. The uncertainties of the safety feedbacks were calculated as in equations 2.3 and 2.4, derived applying the law of propagation of errors:

$$\sigma_{effect} = \sqrt{\frac{err^2_{nominal}}{k^4_{nominal}} + \frac{err^2_{perturbed}}{k^4_{perturbed}}} \tag{2.3}$$

$$\sigma_{Doppler} = \frac{\sqrt{\frac{err^2_{nominal}}{k^4_{nominal}} + \frac{err^2_{perturbed}}{k^4_{perturbed}}}}{|ln(\frac{T_{perturbed}}{T_{nominal}})|} \tag{2.4}$$

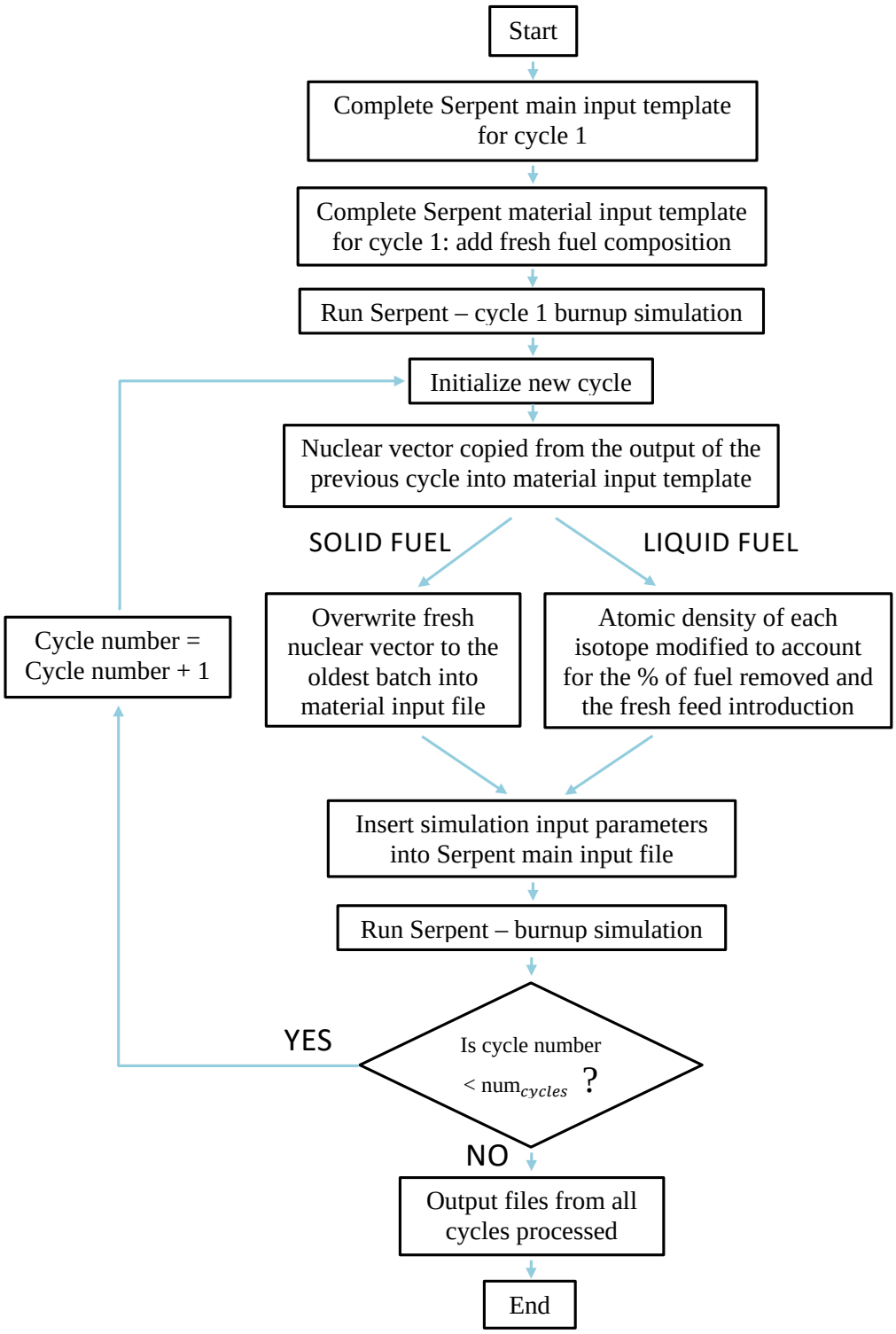

FIGURE 2.1: BBP burnup calculation algorithm

For the MSR study, the safety feedbacks of the whole core were calculated at equilibrium, both at the beginning and end of cycle. In the case of ESFR, the safety feedbacks were computed with two different modalities: for the whole core throughout the transition from initial to equilibrium cycle and at EOEC for different core regions individually. While the former gives an expression of the evolution of the safety feedbacks in time, the latter shows the contribution of each local region to the overall feedback. In order to perform the local mapping of the core, the production of the input files was once more automatized. The algorithm can be seen in Figure 2.2: the core was conceptually divided in many subregions, e.g. in horizontal layers or in batches. A transport simulation was run for each region until the whole core was perturbed.

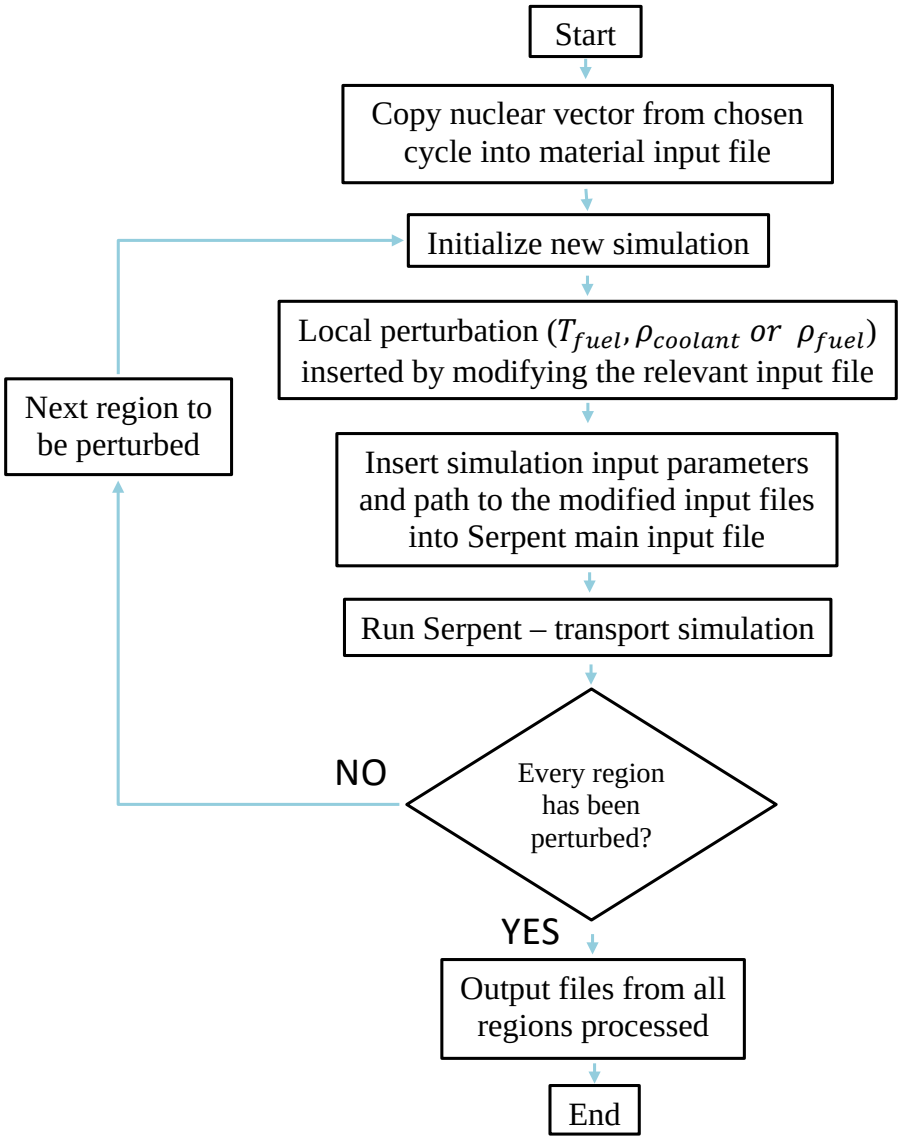

FIGURE 2.2: Safety feedbacks mapping algorithm

Chapter 3

Application to European Sodium Fast Reactor

The first application of the BBP routine is a code to code benchmark of a reduced Serpent2 model of the inner core of the European Sodium Fast Reactor.

3.1 European Sodium Fast Reactor

Sodium Fast Reactor is the most developed among the six advanced systems proposed by the GIF. The prototype of a large fast breeder sodium reactor, Superphenix (SPX), was built in France in the 70s and operated until the 90s. A European project, the European Fast Reactor, was formulated in the 90s to benefit from the experience gained with SPX and to bring the technology a step further, but ended prematurely. Recently, however, a renewed interested into sodium fast technology has converged into the CP ESFR, the Collaborative Program on European Sodium Fast Reactor. The goal of the CP ESFR, ended in 2013, was to move towards the industrial development of the reactor [22]. Today, a consortium of research insitutes, among which PSI, universities as well as companies has gathered to contribute to ESFR-SMART (Safety Measures Assessment and Research Tools), a Horizon2020 project. The project aspires at enhancing the safety of the ESFR and validating new reliable computational tools [23]. This thesis tackles the code-to-code benchmark of a Serpent model of the ESFR inner core in the framework of PSI contribution to the project ESFR-SMART.
The ESFR is a pool type reactor designed for a thermal output of 3600MW$_{th}$ and a net electrical output of 1500MW$_{e}$. The plant is composed of three primary pumps, six internal heat exchangers and six secondary loops [24]. The core design is shown in Figure 3.1 and presented in [25]. The core is structured in circular rings. It is composed, from the inside to the outside, of 216 Inner Fuel (IF) subassemblies and 288 Outer Fuel (OF) ones, surrounded by a reflector and by spent IF and OF subassemblies. In the active core zone there are 36 shutdown devices and 31 corium discharge tubes. The reloading pattern is based on a six-batches scheme, designed to minimize reactivity oscillations between neighbouring assemblies. Each assembly is numbered from one to six, and each cycle one batch is replaced with fresh fuel. At the end of the first cycle batch number 2 is removed, at the end of the second cycle batch number 3 is removed, etc. This reloading scheme is called mixed

and allows avoiding any reshuffling of the subassemblies therefore minimizing the refuelling period duration. Each cycle is 365 days long [14].

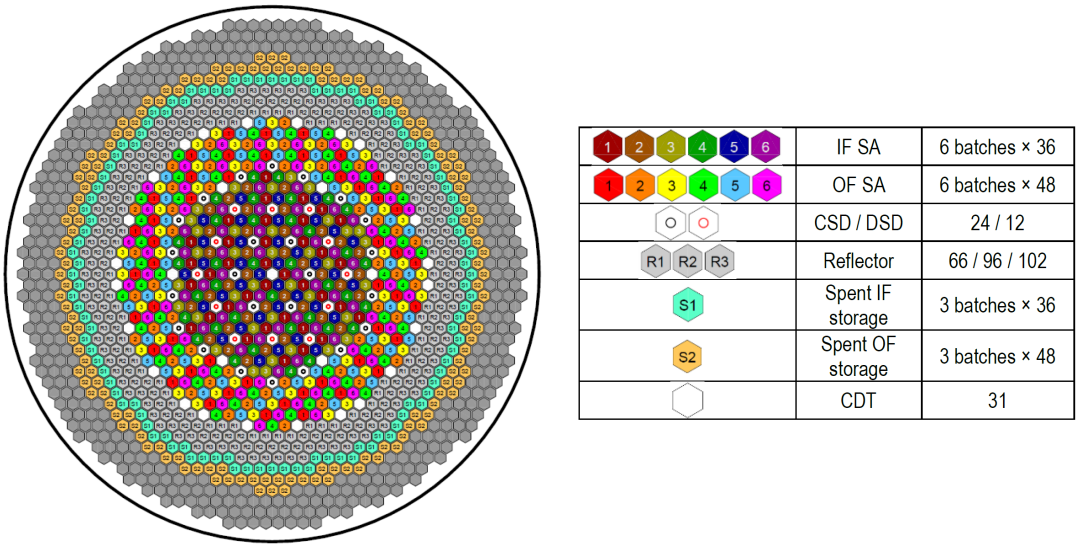

FIGURE 3.1: European Sodium Fast Reactor core design

The assemblies are hexagonal, and enclosed into a EM10 steel wrapper. Each assembly is composed of 271 pins, and is axially divided into a lower fertile region and an upper fissile one. The fissile to fertile ratio is 75:25 in IF and 95:5 in OF. The fissile pellets have a central hole, designed to reduce the central temperature. The assembly pitch is 21.435 cm, whereas the pin pitch is 1.167 cm. Fresh fuel is MOX in the fissile pellets and fertile Uranium dioxide in the fertile blanket. The active core height is one meter, while the whole core is roughly 4 meters long. An upper sodium plenum followed by a neutron absorbing material is introduced on top of the active core to mitigate the positive worth of sodium boiling.

3.2 ESFR inner fuel reduced model

The reduced model utilized in this work has been created at PSI to simulate the ESFR IF within a decreased computational time [13]. The model is generated in the Monte Carlo code Serpent 2 environment. Generally, Monte Carlo simulations are adopted when high precision results are required; however, they come at the cost of high CPU times, especially when large systems like a full-core are modelled. As a consequence, the axial meshing of the fuel assemblies for a Serpent ESFR full-core model is limited by the large computation cost. On the other hand, a Serpent2 reduced model could profit of the high precision of Monte Carlo simulations with a lower computational cost. A fine axial nodalization could be adopted to calculate precise power, burnup and safety feedbacks profiles.
The model is based on the selection of six representative assemblies of the ESFR inner core, as shown in Figure 3.2. It is radially infinite, since periodic

boundary conditions are applied in x and y directions. This model is eligible for reproducing the ESFR inner core behaviour despite of the periodicity condition because previous studies proved that the flux, the sodium void effect and the Doppler constant maintain a flat radial profile in the IF zone [26]. Axially, the design is an exact reproduction of the ESFR structure, and it is composed as presented in Figure 3.3.

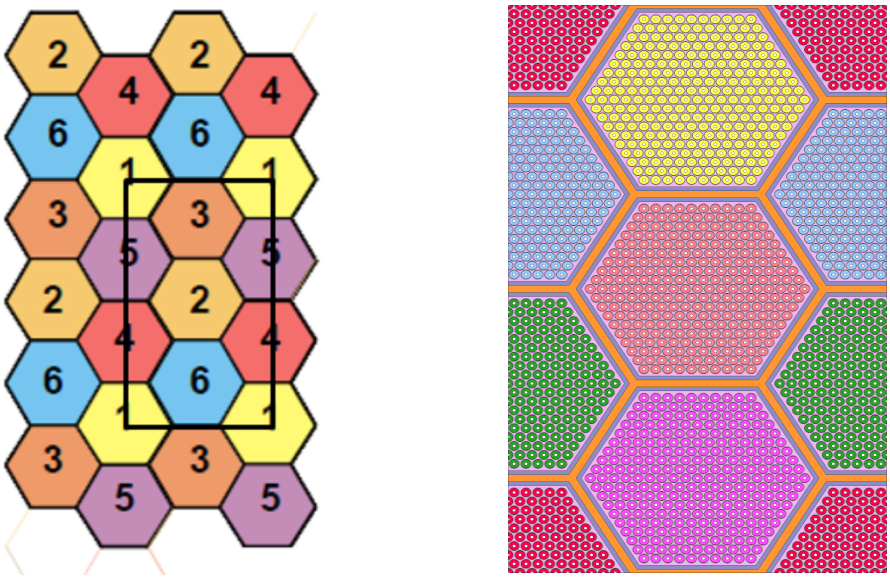

FIGURE 3.2: ESFR inner fuel reduced model radial design

The temperatures adopted are 1500K for the fuel and 900K for the sodium coolant and structural materials. Unresolved resonances probability tables were consistently used, as well as a Predictor-Corrector scheme. The fissile region of the core was axially discretized into 15 burnup regions, while a study about the proper axial nodalization in the fertile core region was performed (see Appendix A). Eventually, 5 axial cells were found to be appropriate for modelling the fertile blanket zone.

3.3 Batch-wise operation simulation

The reduced Serpent model was utilized to simulate the convergence of the ESFR inner core to equilibrium. Open fuel cycle operation 12 cycles long with fixed fuel composition was simulated. Each cycle is 350 days long and divided in two burnup steps. For this calculation, the neutron histories were set to 50000 neutrons, 500 active cycles and 30 inactive ones. The Predictor-Corrector scheme implemented is LE/LI with 3 substeps, and the cross section libraries used are ENDF/B-VII.0. In the next sections, the results of the burnup calculation are presented and compared with the results from more detailed full-core Serpent and ERANOS models. This calculation is based on a previous work [13]; the model used, however, has been updated and simulated with higher statistics.

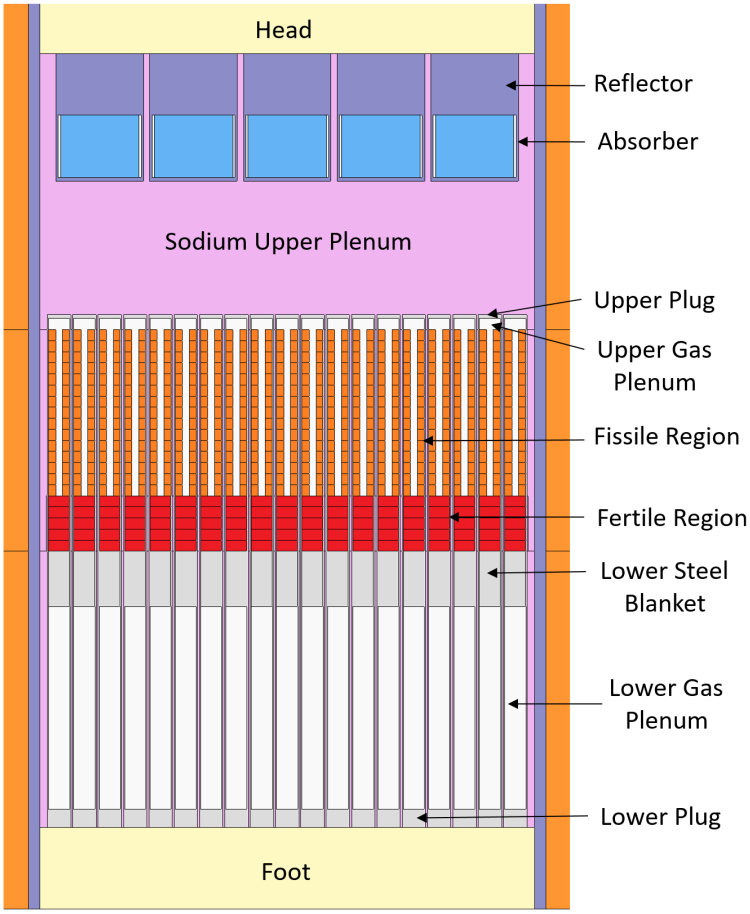

FIGURE 3.3: ESFR inner fuel subassembly axial design

3.3.1 Transition towards equilibrium cycle

The reactivity evolution throughout 12 operation cycles is presented in Figure 3.4. Each cycle, the total reactivity of the six-assembly model decreases linearly by roughly 850 pcm. After six cycles, when each batch has been replaced once, the core reaches equilibrium and the reactivity oscillations do not vary significantly from cycle to cycle. The positive reactivity inserted through refuelling increases from the initial cycle to the equilibrium cycle, because the burnup of the removed batch increases. Figure 3.5 shows the batch-wise power evolution with irradiation time. The total power adopted in the simulation is calculated as seen in Equation 3.1.

$$P = \frac{3600MW_{th}}{(216+288)assemblies} \cdot 6assemblies \simeq 42.9MW_{th} \tag{3.1}$$

During the first cycle the total thermal power is equally distributed between the six assemblies, resulting in $P \simeq 7.14MW_{th}$ per assembly. Once refuelling starts taking place, the power spatial distribution oscillates with a periodicity of six cycles. Since the model is composed of six assemblies and refuelling takes place with a six-cycle periodicity, the power distribution varies both batch-wise and cycle-wise. In particular, the spatial power and burnup distribution between batches vary from cycle to cycle, because the

arrangement of the assemblies causes a slightly uneven neutron flux. In Figure 3.5, this is reflected by the power maxima and minima at equilibrium, which are different from cycle to cycle. Generally, the peak power occurs in fresh fuel at EOC, while the largest power depression occurs in the most burnt assembly at EOC.

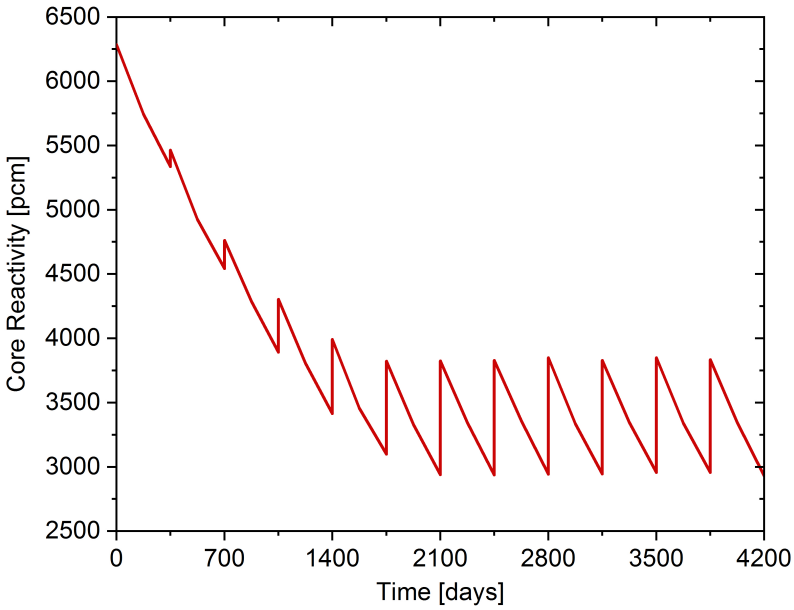

FIGURE 3.4: Core reactivity evolution within 12 cycles

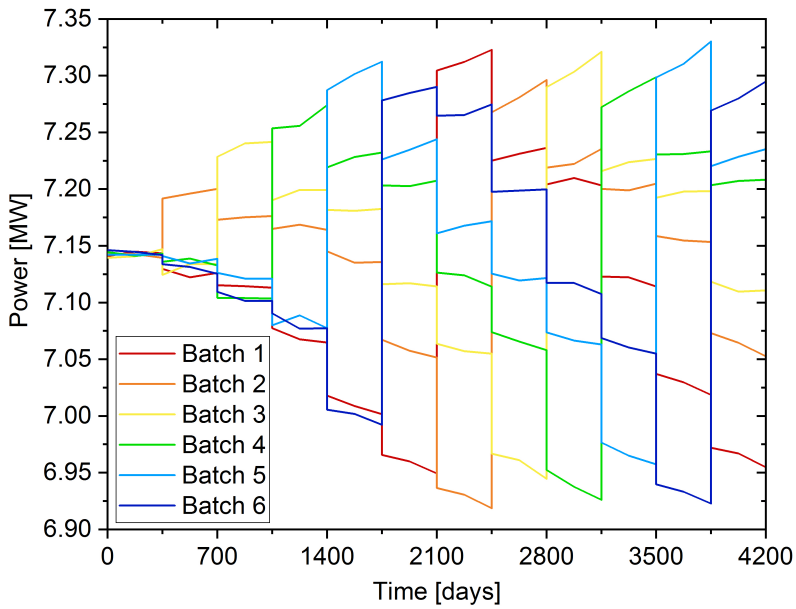

FIGURE 3.5: Batch-wise power evolution within 12 cycles

The axial distributions of power and burnup of Batch 1 at different irradiation times can be seen in Figure 3.6. Once again, the periodicity generated by the refuelling scheme adopted can be observed. Since Batch 1 is replaced at the end of the sixth cycle, the power and burnup profiles of cycles 7-12

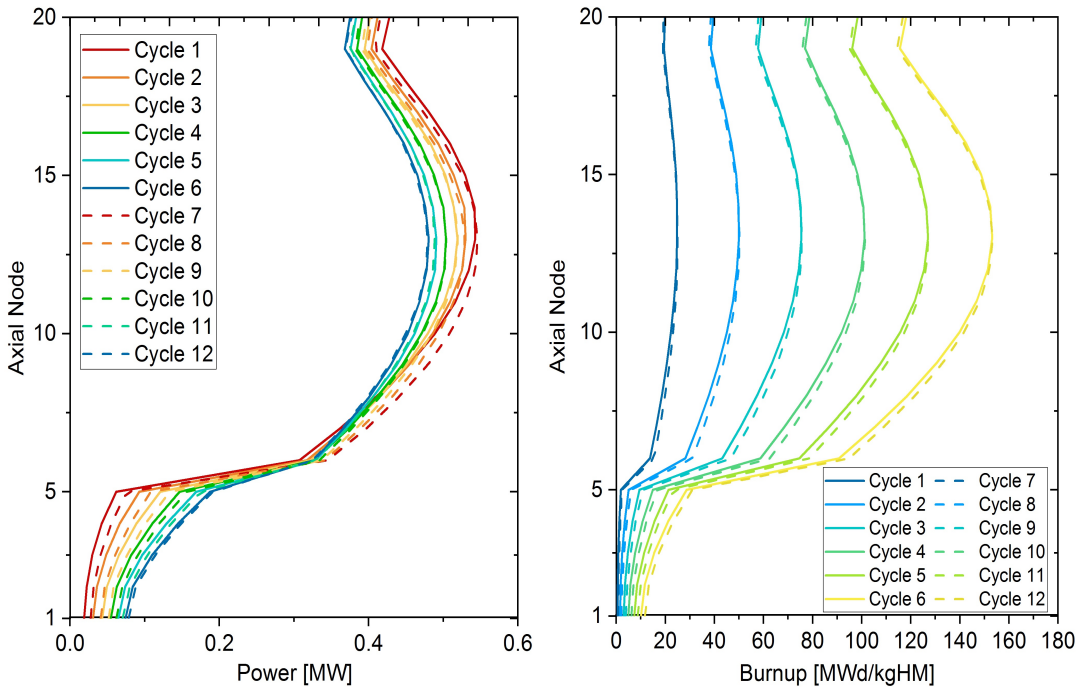

FIGURE 3.6: Axial profiles of power (left) and burnup (right) of Batch 1 at the end of all the simulated cycles, with 20 nodes discretization of the active core

overlap with the profiles of cycles 1-6. Both power and burnup peak in the middle of the fissile region, which extends from node 6 to node 20.

An anomaly with respect to the sinusoidal shape of power and burnup expected in the fissile region can be seen in the last node of the core. Although power and burnup are expected to decrease because of the high neutron leakage at the periphery of the core, they increase. This behaviour may be due to neutrons thermalization and reflection taking place in the sodium upper plenum above the core. However, this effect has not been observed in any other model results, and an extensive explanation has not been found yet. For more insights, see Appendix B.The power axial profile flattens out with irradiation, because of fuel depletion in the fissile region and of fissile fuel breeding in the fertile one. Batch 1 peak power at EOC is achieved at cycles 1 and 7, and it is 0.54 MW. The burnup increment from cycle to cycle is roughly constant in the fissile region. In the fertile region it increases faster with irradiation because of the build-up of fissile isotopes. The peak burnup in Batch 1 occurs at cycles 6 and 12 and it is 153 MWd/kgHM. The build-up of burnup from cycle to cycle for each batch is shown in Figure 3.7. Initially, when the flux in the periodic model is perfectly flat, the burnup profiles of each batch are superimposed. After each cycle, the assemblies which are not replaced accumulate almost exactly the same burnup.

The evolution of the concentration of the most relevant actinides, i.e. ^{235}U, ^{238}U, ^{239}Pu, ^{240}Pu, can be seen in Figure 3.8. The two Uranium isotopes, shown in the top two graphs, are widely consumed from cycle to cycle. ^{235}U is present in very small concentrations, and it is depleted at a lower rate each cycle until it is almost entirely consumed.

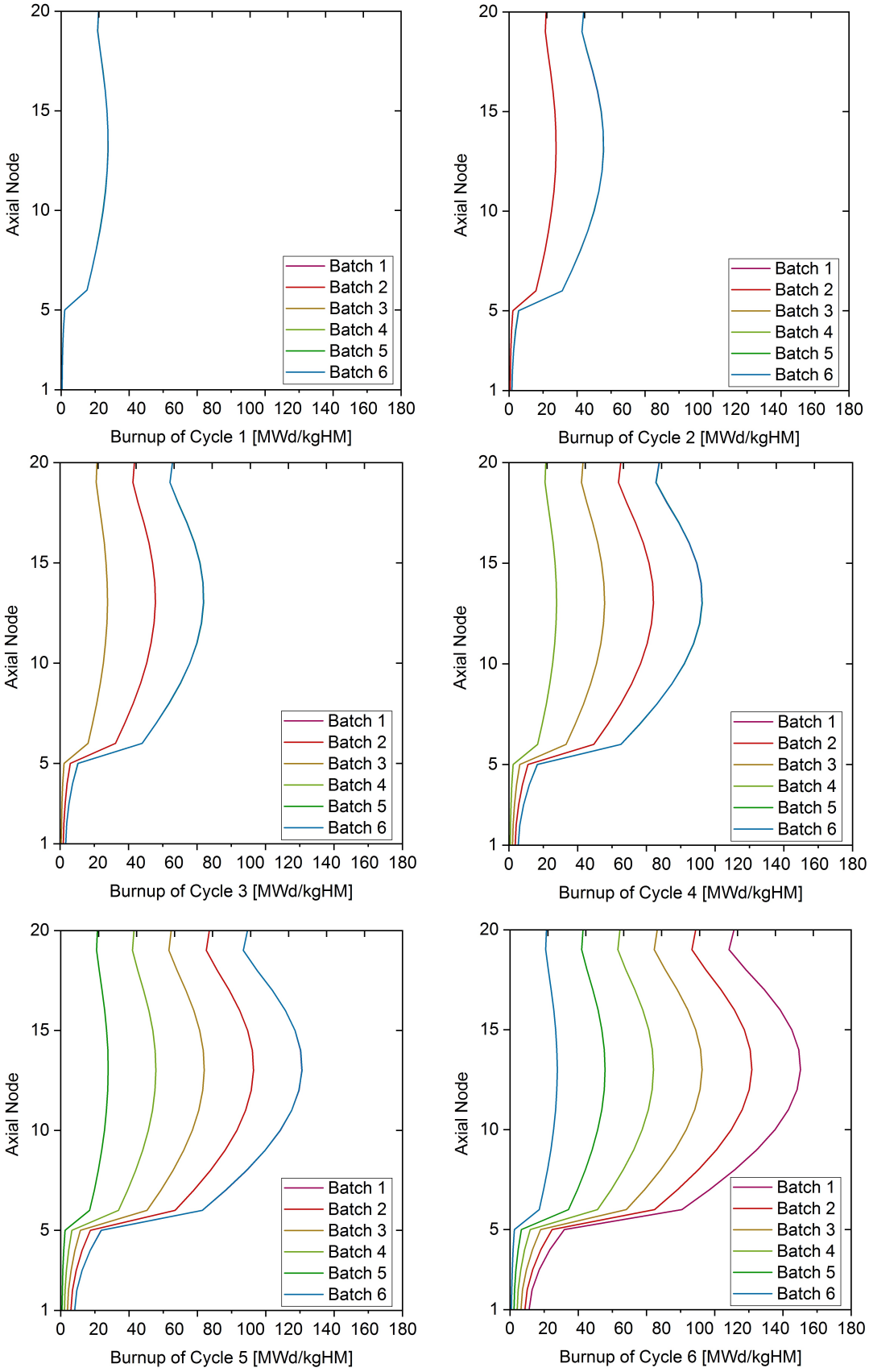

FIGURE 3.7: Burnup axial profile of each batch at the end of cycles 1 to 6

^{238}U is the main breeding source, and it is depleted almost exclusively by neutron capture. Three competing processes determine ^{239}Pu concentration evolution: generation from ^{238}U, fission and transmutation into ^{240}Pu. ^{239}Pu is originally absent in the fertile region, and it is generated from ^{238}U breeding. The net production rate slows down with irradiation because of its increasing consumption. In the fissile region net production is initially positive, but after cycle 4 neutron capture and fission prevail. ^{240}Pu is fertile, so it is depleted mainly by transmutation into ^{241}Pu. Its consumption is faster than its generation in the fissile region, contrarily to the fertile region.

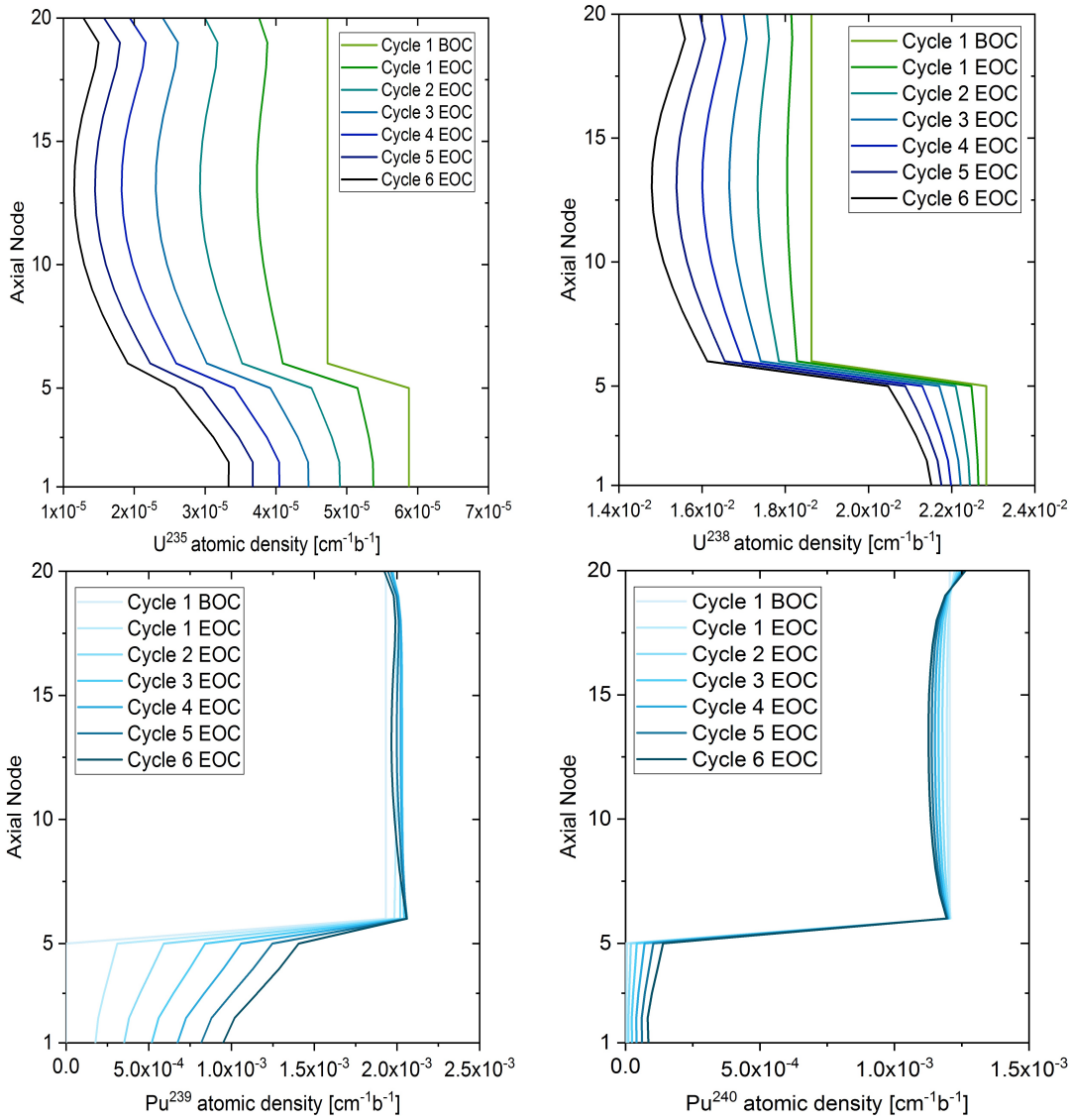

FIGURE 3.8: Axial profile of the atomic densities of ^{235}U, ^{238}U, ^{239}Pu, ^{240}Pu in Batch 1 from cycle 1 to cycle 6

3.3.2 Comparison with full-core model results

In order to assess the capability of the reduced Serpent model to simulate the inner fuel features, some of the results presented in the previous section

are compared with those from two ESFR finite models. Those are a Serpent2 model and an ERANOS2 model coupled with the EQL3D procedure. Those models simulate $\frac{1}{3}$ of the ESFR full-core with repetitive boundary conditions at the interfaces. The nuclear data libraries used are JEFF-3.1, contrarily to the reduced Serpent model in which ENDF/B-VII.0 nuclear data were applied. All the data used for comparison are taken from [14], an official ESFR deliverable reports. Figure 3.9 compares the transition of the core reactivity from beginning of life to equilibrium for the reduced Serpent model and the ERANOS model. Additionally, Table 3.1 compares the reactivities from the three models at BOL, BOEC and EOEC. The reactivity difference between the infinite model and the finite ones is approximately 2500 pcm. This large difference is due firstly to the absence of neutron losses from radial leakage in the radially infinite model. In second place, some neutron absorbing components like control rods and equipment guide tubes are not included in the reduced model. In the reduced Serpent model, the first six cycles were simulated with both JEFF-3.1 and ENDF/B-VII.0 nuclear data libraries. The difference between the two results is almost 1000 pcm at BOL, and it gradually decreases up to roughly 150 pcm at the end of the sixth cycle. However, since the use of JEFF-3.1 libraries increases the core reactivity in the reduced model, the reactivity difference between the two models cannot be attributed to the use of different libraries.
The reactivity gap between the infinite Serpent model and the two finite models is roughly constant. Thus, the reduced core and the full-core evolve coherently. Furthermore, it must be noticed that the equilibrium reactivity at BOC and EOC varies from cycle to cycle. This effect is more pronounced in the finite models: the elements such as control rod and guide tubes, which are not included in the infinite model, break the periodicity of the full core. Additionally, the two finite models only simulate $\frac{1}{3}$ of the core with boundary conditions connecting the two interfaces; since the assemblies at the boundaries do not match precisely, further spatial effects are introduced. As a consequence, each fuel batch has a slightly different reactivity worth. Additionally in the case of ERANOS, cross-sections are recalculated every six cycles, so a full convergence to equilibrium in ERANOS may take more cycles than the ones simulated.

TABLE 3.1: Comparison between core reactivity for three different models; "INF" and "FIN" refer respectively to the Serpent infinite and finite models

	Serp INF	**ERANOS**	**Serp FIN**	**Serp INF - ERANOS**	**Serp INF - Serp FIN**
BOL	6285	3769	3942	2516	2343
BOEC	3836	1258	1400	2578	2436
EOEC	2945	481	549	2464	2394
EOEC-BOEC	-891	-777	-851	-114	-40

The axial profiles of burnup and power of each batch at EOEC were compared with those produced by the finite Serpent model. The axial profiles

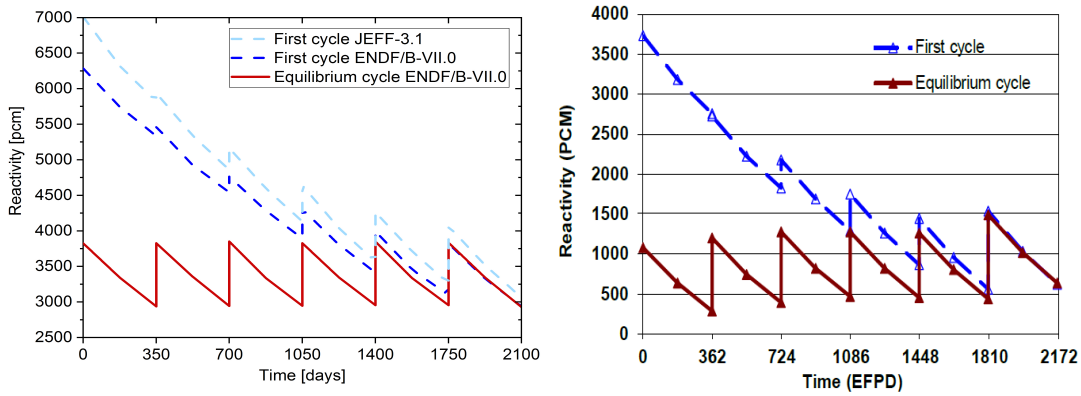

FIGURE 3.9: Reactivity evolution throughout 12 cycles for the reduced Serpent model (left) and ERANOS model (right) [14]

reported from both models are a snapshot in time taken at the end of an equilibrium cycle. However, due to the six-cycle periodicity of the refuelling strategy and to the elements previously mentioned which perturb the radial neutron flux, power and burnup spatial distribution changes from cycle to cycle. Therefore, results from a different equilibrium cycle would be slightly different. Since the spatial effects which cause such radial and axial neutron flux variations from cycle to cycle are model-dependent, the comparison should be taking place between data averaged over six cycles. However, those data were not available for the finite Serpent model, so the comparison shown is biased.

The burnup profiles from the two models are presented in Figure 3.10, while the numeric comparison between the highest burnups in the fissile and fertile regions is shown in Table 3.2. The agreement in the fissile region improves with increasing assembly burnup. When most of the fissile material throughout the assembly is exhausted, the burnup axial profiles match better. In the fertile region, the relative error varies without following a clear trend, and it is in average higher than in the fissile zone. The strong discrepancy partially derives from the different nodalizations of the core. While the infinite model employs 20 axial nodes, the finite one uses a coarser mesh with 8 axial nodes. On the other hand, the error in the burnup profiles is related to the error in the power profiles.

The power axial profiles are presented in Figure 3.11, while a numeric comparison is shown in Table 3.3. The power profiles produced by the finite Serpent model account for all the assemblies of the IF, which are 36 per batch. In the table, the batch-wise power values from the finite core are divided by 36, i.e. the average power of each batch was considered. To produce the power profiles, 20 axial detectors were added to the finite model. Once again, the agreement between the two models deteriorates for fresher fuel in the fissile region, and is consistently very poor in the fertile region. The reasons can be several. In first place, the total power of the reduced model was calculated as the full-core power divided by the total number of assemblies and multiplied by six. This calculation relies on the assumption that the total thermal power is equally distributed between IF and OF assemblies,

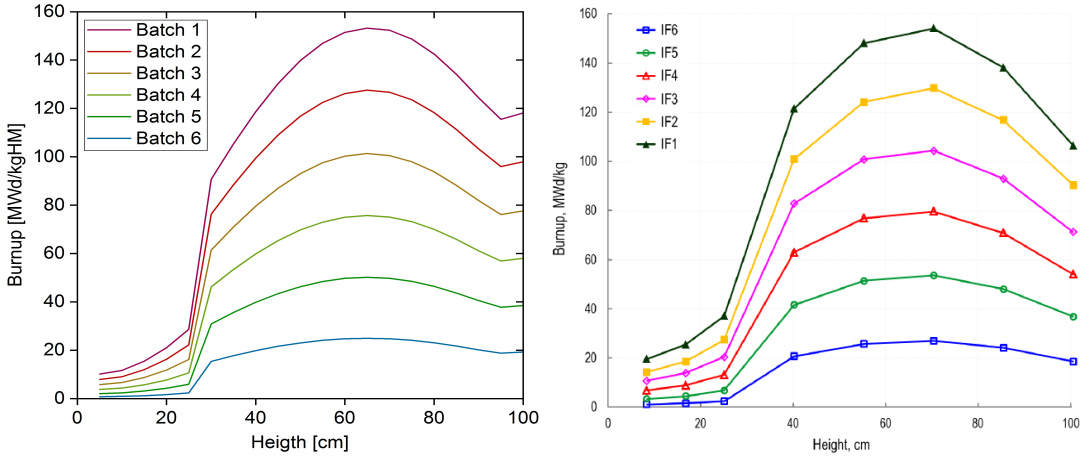

FIGURE 3.10: Axial profiles (infinite Serpent left, finite Serpent right [14]) of EOEC burnup for each of the IF batches

TABLE 3.2: Comparison between peak burnups in the fissile and fertile regions for Serpent infinite and finite models

	Peak BU FI zone EOEC			**Highest BU FE zone EOEC**		
	FIN $[\frac{MWd}{kgHM}]$	**INF** $[\frac{MWd}{kgHM}]$	**Err**	**FIN** $[\frac{MWd}{kgHM}]$	**INF** $[\frac{MWd}{kgHM}]$	**Err**
Batch 1	154.4	153.4	0.7%	36.8	30.9	16.0%
Batch 2	129.6	127.6	1.6%	27.2	23.4	14.0%
Batch 3	104.0	101.3	2.6%	20.8	16.7	19.6%
Batch 4	79.2	75.6	4.6%	13.6	10.9	20.2%
Batch 5	54.4	50.2	7.8%	6.4	6.0	6.1%
Batch 6	27.2	24.9	8.5%	2.4	2.3	3.3%

which is not the case. Therefore, the power normalization employed in the infinite and finite cases is different. Additionally, the reduced model is based on the assumption that the neutron flux is flat in the IF zone. However, [14] shows that the radial power profile is slightly descending towards the outside. Therefore the power differs from assembly to assembly of the same batch; the reduced model probably represents better the most central assemblies, less subject to leakage and radial spatial perturbations of the flux.
Another source of error is given by the different cross-section libraries utilized in the infinite and finite models, respectively ENDF/B-VII.0 and JEFF-3.1.

3.4 Doppler Constant and Sodium Void Effect

Detailed knowledge of temperature and density feedback coefficients and their local distribution is crucial for the safety of any nuclear reactor. This statement is especially relevant for SFR, where the sodium density effect is usually positive and an Unprotected Loss Of Flow (ULOF) transient may result in a reactivity excursion. The coolant density effect is positive in all iso-breeding fast reactors except of the molten salt reactor [8], where coolant

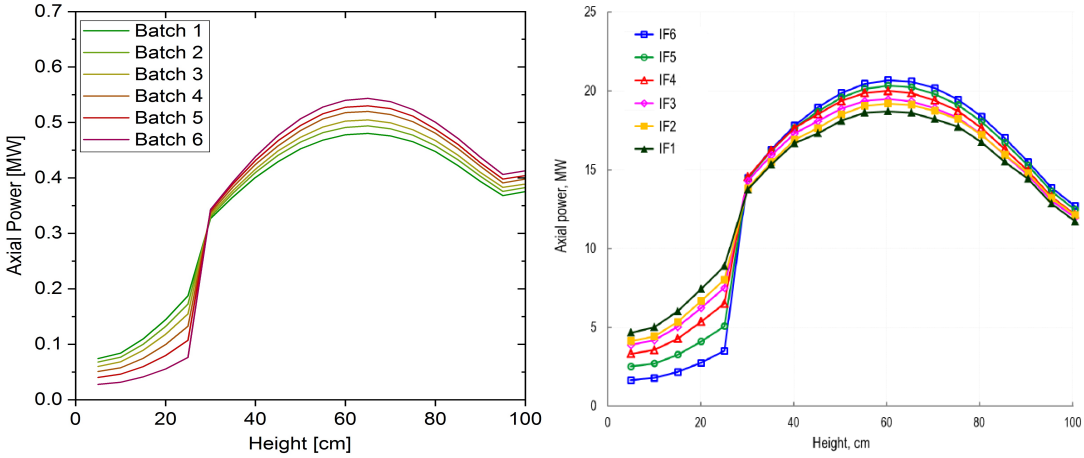

FIGURE 3.11: Axial profiles (infinite Serpent left, finite Serpent right [14]) of EOEC power for each of the IF batches

TABLE 3.3: Comparison between peak powers in the fissile and fertile regions for Serpent infinite and finite models

	Peak Power FI zone EOEC			Highest Power FE zone EOEC		
	FIN [MW]	**INF [MW]**	**Err**	**FIN [MW]**	**INF [MW]**	**Err**
Batch 1	0.57	0.54	5.1%	0.24	0.19	21.8%
Batch 2	0.56	0.53	6.3%	0.22	0.18	21.2%
Batch 3	0.56	0.52	6.6%	0.21	0.16	24.9%
Batch 4	0.54	0.50	7.0%	0.18	0.13	27.1%
Batch 5	0.53	0.49	7.7%	0.14	0.11	21.2%
Batch 6	0.52	0.48	7.8%	0.10	0.08	21.1%

and fuel are mixed. Sodium coolant density effect is stronger than for gas coolants, but weaker than for lead or lead-bismuth coolants. Nonetheless, compared to those heavy liquid metals, the gap between operating temperature and sodium boiling point is much smaller (≈290 K). The positive reactivity introduced by sodium boiling is the major safety risk in case of an ULOF transient. From neutronic perspectives, the reduced sodium density decreases the neutrons scattering in the core and the resulting spectrum hardening causes reactivity increase. At the same time, reduced scattering increases the neutron leakage at the core periphery. The strength of sodium void effect depends on the core design. It is lower in cores with higher leakage. In recent designs [27][28][29] the positive void effect is reduced by minimizing the sodium share in the core lattice and by maximizing the importance of neutron leakage. This is typically achieved by introducing an upper sodium plenum followed by a neutron absorber, as in the ESFR case. The plenum effect is amplified by increasing the neutron importance in the upper core part with an axial blanket at the bottom half of the core. As a result, the local void map is crucial for proper simulation and understanding of the ULOF transient behavior. It was already shown that the local void effect ranges from strongly positive (core center) to strongly negative (sodium plenum) values and that the overall effect is not a linear combination of these

components [26]. Furthermore, the Doppler effect is interacting with the void effect and the spectral shift caused by one effect influences the other. In this work, Doppler constant and coolant void effect were evaluated for different zones at the EOC state. Additionally, their integral values were calculated during the evolution from BOL to EOEC.

3.4.1 Safety parameters evolution towards EOEC

Void effect and Doppler constant were calculated for the ESFR reduced model over 12 operation cycles. In the case of Doppler, the temperature of both fissile and fertile fuel was perturbed. In the case of void, the coolant in the fissile fuel region, in the upper plug and in the upper plenum was voided. In the core, only the sodium inside of each assembly was voided whereas the sodium outside of the steel wrapper was not perturbed. Four situations were compared:

- Nominal case
- Fuel temperature decreased from 1500 K to 600 K
- Sodium density reduced by a factor of 10^9
- Fuel temperature decreased from 1500 K to 600 K and sodium density reduced by a factor of 10^9.

Through these combinations, four safety feedbacks were calculated: Doppler constant for flooded and voided core, and void effect with nominal and 600 K fuel temperature. For each of the mentioned cases, BOC, MOC and EOC transport simulations for each of the 12 cycles were performed. To improve statistics, each simulation was repeated three times and the results were averaged. Eventually, a maximum error of 10.3 pcm and 9.8 pcm was produced respectively for Doppler constant and for void effect. The results are shown in Figure 3.12.

Although the statistics used for fuel temperature and coolant density calculations are identical, and the errors produced are similar, the temperature constant curves show high stochastic noise whereas the void effect ones do not. While the sodium density was reduced to almost zero, the intensity of the temperature perturbation was limited by the cross-sections available in Serpent. Due to the stochastic nature of Monte Carlo simulations, a weak perturbation produces more scattered results.
The safety feedbacks converge to equilibrium after approximately six cycles. Both void effect and Doppler constant degrade with burnup, due to the increase of minor actinides concentration which hardens the neutron spectrum [30]. The difference between BOL and BOEC Doppler constant for flooded and voided core is respectively 140 pcm and 100 pcm. In the case of void effect, the difference is higher and it is 430 pcm for nominal fuel temperature and 470 pcm for cold fuel. At the same time, at equilibrium the evolution from BOC to EOC is worth approximately 30 pcm for the two Doppler constants and 160 pcm for the two void effects. Due to the induced hardening

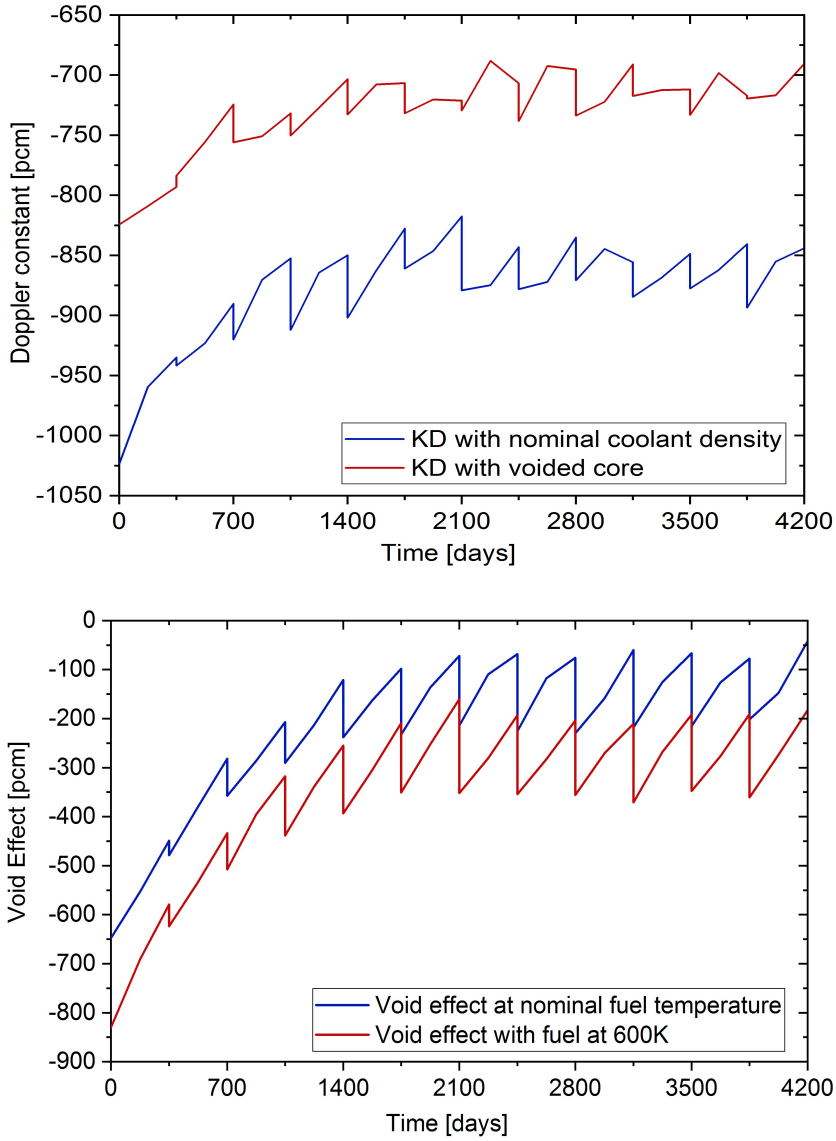

FIGURE 3.12: Safety feedbacks time evolution: Doppler constant for flooded and voided core (top) and void effect for nominal and Doppler fuel temperature (bottom)

of the neutron spectrum, the Doppler constant for the voided core guarantees a worse safety margin compared to the Doppler constant for the flooded core. On the other side, the void effect for a cold core is more negative than the effect for the nominal core, due to the spectrum softening resulting from reduced resonance absorptions.
The results obtained can be compared with those produced by the finite ERANOS model introduced in the previous section. A full comparison is presented in Figure 3.13. In some cases, especially the ones concerning Doppler constants, in ERANOS results the end of the first cycle does not coincide with the beginning of the equilibrium cycle. This is a consequence of the periodic recalculation of cross-sections.

The absolute feedback values of the Serpent model differ from ERANOS ones by approximately -300 pcm for the void effects, and roughly 50-100 pcm

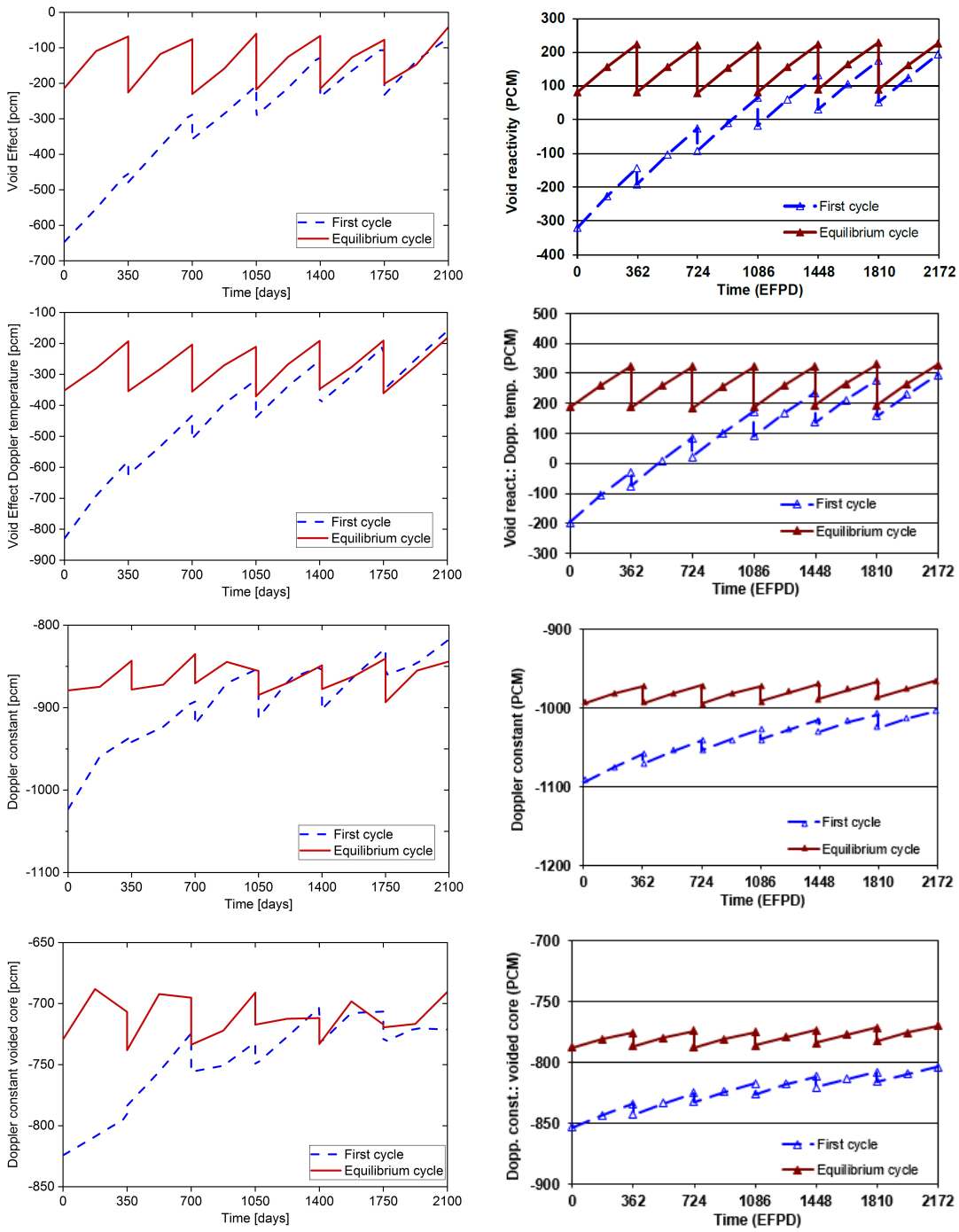

FIGURE 3.13: Comparison between void effect for nominal and Doppler fuel temperature (600K and 2500K) and Doppler constant for flooded and voided core from Serpent infinite model (left) and finite ERANOS model (right) [14]

for the Doppler constants. The case of void effect at Doppler temperature is an exception, since the perturbed fuel temperature is 600 K in the infinite model and 2500 K in ERANOS. Decreasing the fuel temperature, the void effect becomes more negative, while increasing the fuel temperature it becomes more positive. Thus, the difference between the two cases is amplified

and it is roughly -550 pcm. It must be considered, however, that ERANOS feedbacks are calculated for the full core. Consequently, the contribution of the outer fuel and of radial neutron leakage bias the comparison between the feedbacks absolute values. Nonetheless, the evolution of the void effect and Doppler constant computed by the two models are in very good agreement.

3.4.2 Safety parameters mapping at EOEC

The capability of the reduced Serpent model to calculate local feedbacks was tested. Doppler constant and void effect were calculated at the equilibrium state, at EOC. For comparison ERANOS inner core feedbacks maps, produced at PSI as a contribution to the ESFR-SMART project, were used. Feedback maps with different levels of spatial refinement were computed. The capabilities of the BBP script to manipulate Serpent inputs were extended for such calculation, while the EQL3D ERANOS procedure has this feature integrated. The EQL3D methodology for simulating reactivity changes in the order of pcm by direct calculation is described in [26]. The same restart file is used for nominal and perturbed cases and the calculation is stopped after a fixed number, e.g. 25, of iterations. These two calculations as such are not fully converged. The difference between them has, however, already converged and seems meaningful. Full mathematical prove of this method was not carried on.
As observed in the previous section, the fact that Serpent model is radially infinite strongly influences the safety coefficients. Surprisingly, both the void effect and Doppler constant computed by Serpent for the active inner core are higher by a factor of roughly 1.5 compared to ERANOS values. Therefore, this number was used for Serpent results renormalization in the safety coefficient maps. Some consideration about the safety parameters normalization can be found in Appendix C.

Doppler constant

Doppler constant is roughly additive and there are not strong spatial correlation between different regions [26]. Therefore the sum of the local effects can represent faithfully the overall behaviour of the core. Different discretizations were considered. At first, all the six fuel batches in the inner core have been perturbed simultaneously. The core was divided into 1, 2, 4, 10, and 20 axial nodes, as presented in Figure 3.14. The Doppler constant of each region is shown, as well as the constant per 5 cm node. The colour scheme in the feedback maps was locked to the physical range. Outliers were highlighted in red or dark blue. For a coarse discretization, Serpent results are comparable to ERANOS results, which are perfectly additive. However, in the 20 nodes case for the Doppler constant the reactivity change is comparable with the stochastic error produced by Serpent, thus a strong stochastic noise is generated.

A similar axial nodalization was used for batch-wise mapping, where each group of assemblies is perturbed separately. Figure 3.15 shows results in

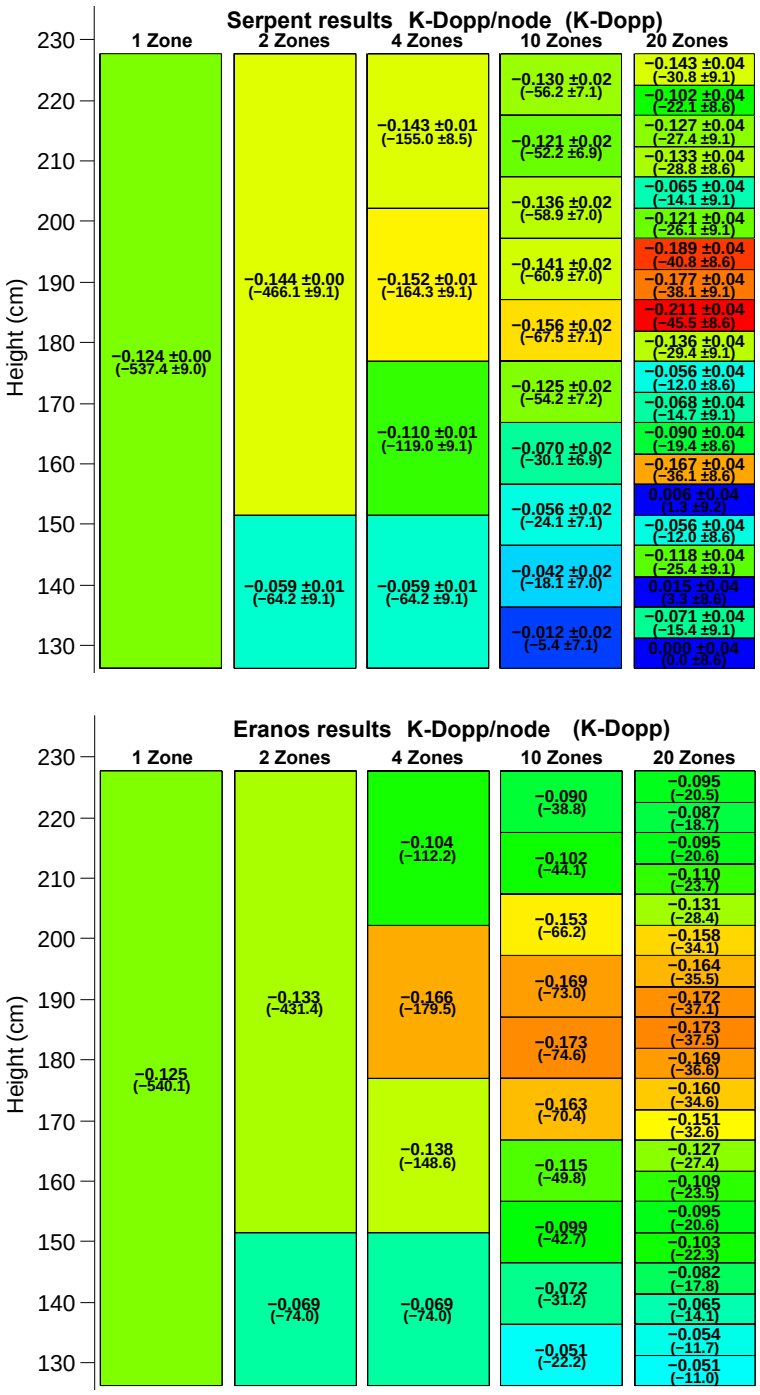

FIGURE 3.14: Doppler constant calculated by Serpent (top) and ERANOS (bottom) for different axial nodalizations

case of 4 axial nodes. The mapping produced by Serpent model for Doppler constant faces strong stochastic behaviour, because the selected accuracy is lower than the effect itself. Some feedback colour maps with higher refinement can be seen in Appendix D. When 10 and 20 axial nodes are adopted, Serpent results lose any physical meaning. On the other side, ERANOS maintains high accuracy even when the discretization requires a sensibility of a fraction of pcm.

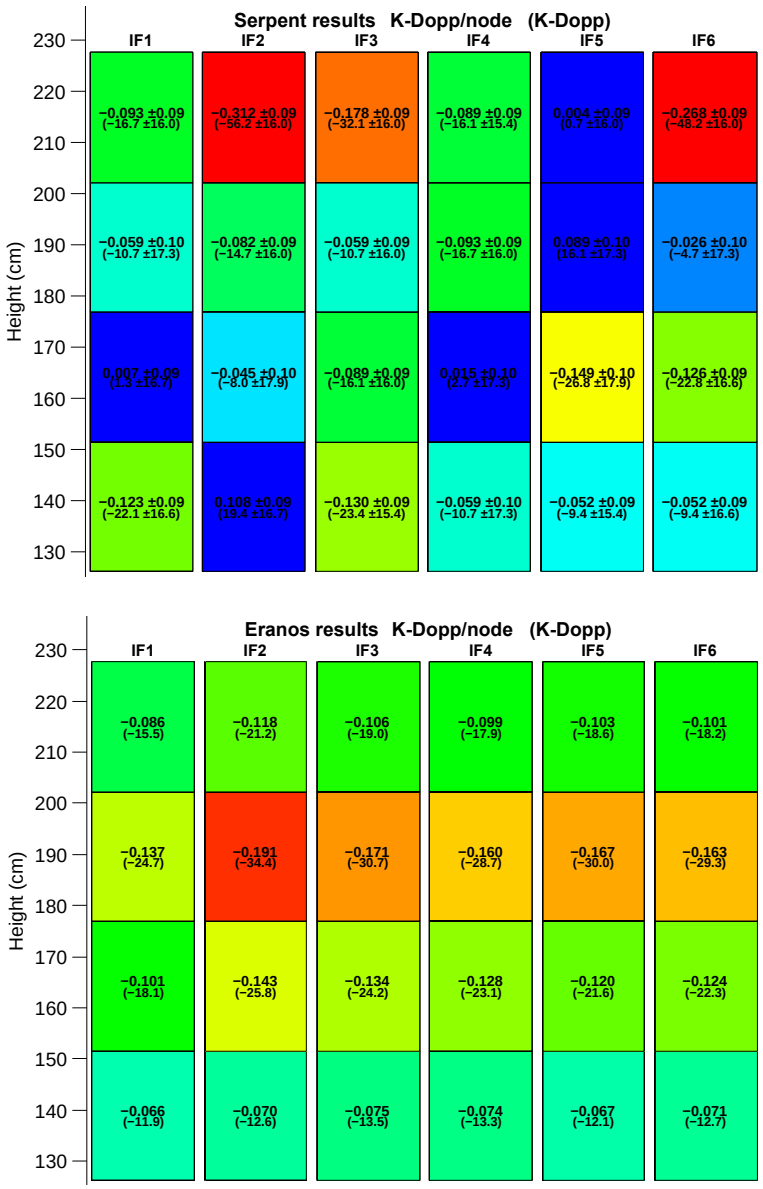

FIGURE 3.15: Doppler constant calculated by Serpent (top) and ERANOS (bottom) for 4 axial nodes and 6 batches

For a better comparison between the results from the two codes, axial profiles as in Figure 3.16 were produced. In ERANOS, there is good agreement between the profiles composed of 10 and 20 nodes. On the other side, the 20 nodes Serpent profile shows strong stochastic oscillations, due to the high uncertainty compared to the reactivity feedback per node. The 10 nodes profile does not show high statistical scattering, and it evolves similarly to ERANOS model in the lower half of the core. However, Serpent is not able to represent the axial Doppler behaviour of the inner core unless extremely high statistics are implemented.

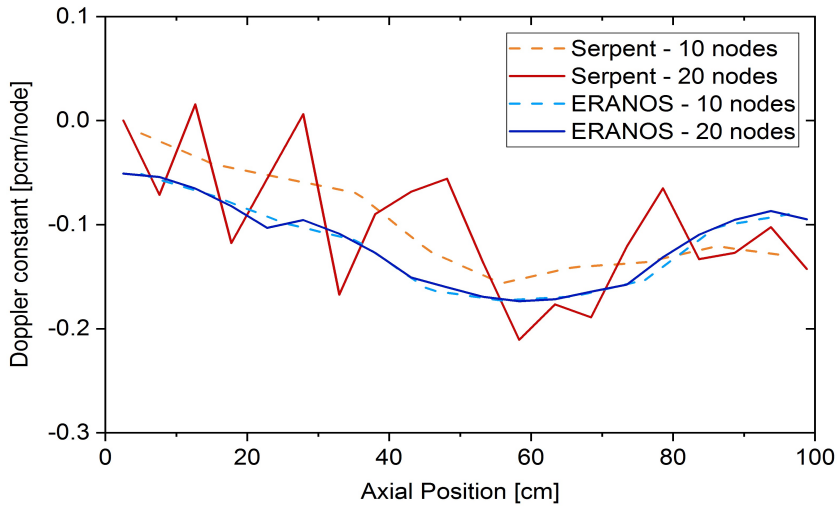

FIGURE 3.16: Doppler constant axial profiles calculated by Serpent and ERANOS

Sodium void effect

The sodium void reactivity worth was calculated by reducing the density of the sodium inside of the assemblies wrapper by a factor of 10^9. As in the case of the Doppler constant, the local void effect was calculated at EOEC for the whole core and for smaller regions. Additionally, the void reactivity worth of sodium in the upper plenum and in the upper plug was computed. Contrarily to the fuel temperature effect, the coolant density shows strong interconnections between adjacent regions. This can be observed in Table 3.4. The void effect of the upper plenum was calculated for flooded and voided top fuel region; at the same time, the void effect of the top fuel region was calculated for flooded and voided upper plenum. The results show a strong correlation between the two regions. The top fuel void effect decreases by roughly 50% when the plenum is voided, and the plenum void worth decreases by 7% when the top 20 cm of fuel are voided. In both cases, the difference is approximately 100 pcm. The important interdependency between the two zones depends on the strong impact of leakage on the void effect. Additionally, at the boundary between core and upper plenum the sodium void effect is not additive. Voiding the two regions separately, the effect is roughly 100 pcm less negative than when they are voided together. This can be seen in Table 3.5. On the contrary, Table 3.6 shows that the void effect in the core region is additive: the difference between the cumulative effects of each single region and the effect of the whole fissile region is smaller than its uncertainty. Consequently, local maps of the coolant void effect can faithfully represent the core region; on the other hand, they are not fully reliable close to the interface between the active core and the upper plenum.

The void effect maps produced by Serpent and ERANOS for 1, 3, 8, 17 and 27 nodes can be seen in Figure 3.17. The absolute reactivity difference generated by sodium voiding and the void effect normalized per mass of voided sodium are reported in the results. As in the case of Doppler constant, Serpent results have been further normalized by a factor of 1.5, which is the

TABLE 3.4: Void effect in sodium upper plenum and top of the core region for flooded and voided conditions

		Upper Plenum		
	Reactivity	Flooded	Voided	Plenum void
100cm-80cm core region	Flooded	2790	1366	**-1424**
	Voided	2992	1470	**-1522**
	Core void	**202**	**104**	[pcm]

TABLE 3.5: Void effect additivity at the boundary between sodium upper plenum and fissile core region

	ρ [pcm]	Void Effect [pcm]	σ [pcm]
Nominal	2790		
Upper Plenum voided	1366	-1424	14
Last 20 cm fissile voided	2992	202	13
SUM		**-1222**	**19**
Upper Plenum + last 20 cm fissile voided	1470	**-1320**	**13**
DIFFERENCE		**98**	**23**

TABLE 3.6: Void effect additivity in the fissile core region

	ρ [pcm]	Void Effect [pcm]	σ [pcm]
Nominal	2790	-	**-**
100cm-80cm core voided	2992	202	13
80cm-60cm core voided	3381	591	13
60cm-45cm core voided	3209	419	13
45cm-25cm core voided	3033	243	13
SUM		**1454**	**26**
ALL Fissile core region voided	4216	**1426**	**13**
DIFFERENCE		**28**	**29**

ratio between the maximum effects calculated by Serpent and ERANOS in the 17 zones case. Since the coolant void effect in the ESFR inner fuel is stronger than the fuel temperature effect, the statistical error plays a weaker role in Serpent results. Therefore, a fine nodalization made by 20 fuel zones and 7 Upper Plenum zones gives reasonably physical results. Inside the core, the additivity of the void effect is respected. This is hardly the case in the upper plug and upper plenum, for both Eranos and Serpent. In Figure 3.18, the void effect of each batch is presented singularly, for 8 axial nodes.

ERANOS produced accurate and physical results. In the case of Serpent, however, the intensity of the void effect is comparable to the statistical error produced in the calculation. This is particularly true in the peripheries of the core and in the upper plug. Other void worth maps with a more refined

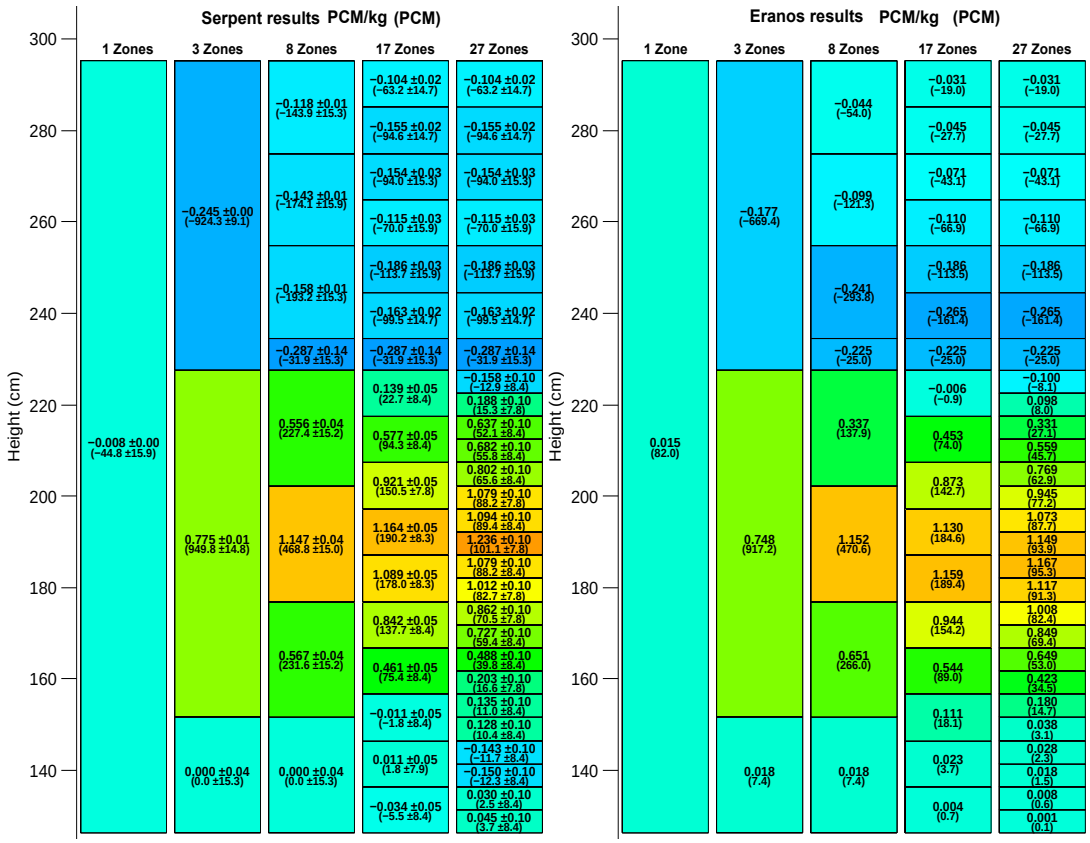

FIGURE 3.17: Void Effect calculated by Serpent (left) and ERANOS (right) for different axial nodalizations

meshing are shown in Appendix D. From those results it can be observed that, while ERANOS maintains high accuracy, Serpent results strongly oscillate.

For a better comparison between the reactivity effects calculated by two codes, axial profiles were produced and presented in Figure 3.19. The agreement between ERANOS results for 14 and 27 nodes is extremely good. The profile generated by Serpent with 14 nodes is accurate as well, even though the maximum is shifted of 5 cm with respect to ERANOS. In the Serpent profile composed by 27 nodes, some statistical oscillations are visible. Overall, however, all results produced for the void effect show a consistent physical behaviour.

3.4.3 Number of neutron histories and stochastic error

As mentioned in the previous section, good statistics are crucial for feedback maps calculations. In Monte Carlo codes, statistics depend on the number of neutrons, active and inactive cycles simulated. In general, the global number of neutrons implemented per simulation is indicative of both the accuracy achievable and the necessary computational time. Figure 3.20 shows that increasing the number of neutrons employed in the perturbed case simulation, i.e. reducing the statistical error, the scattering in the Doppler constant axial profile composed of 10 nodes decreases strongly. In the case of sodium void

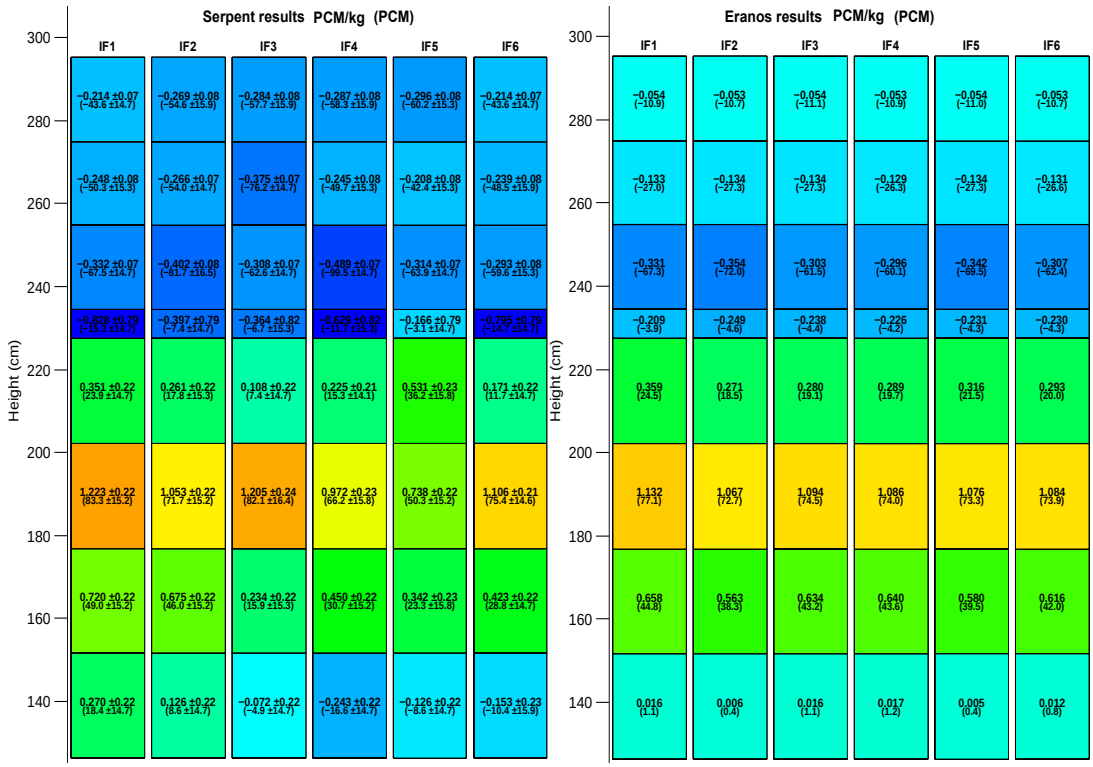

FIGURE 3.18: Void Effect calculated by Serpent (left) and ERANOS (right) for 8 axial nodes and 6 batches

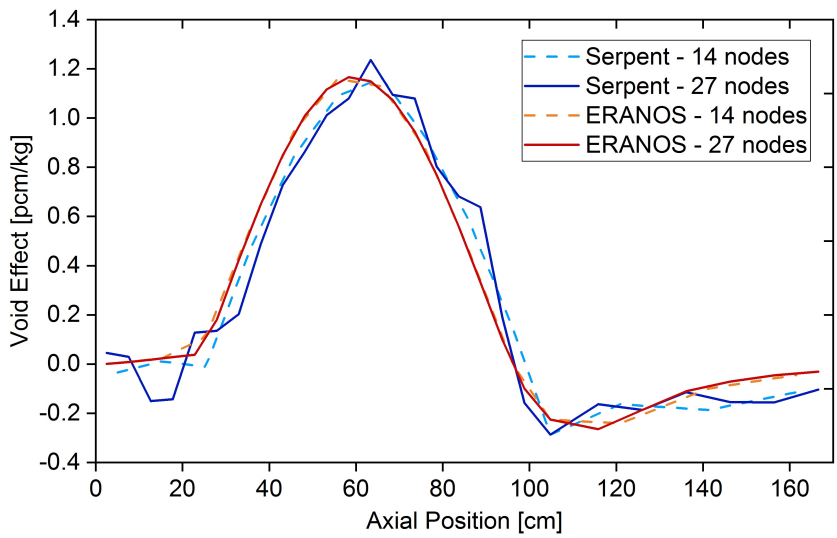

FIGURE 3.19: Axial void effect profiles calculated by Serpent and ERANOS

effect, simulated statistics have a lower impact than in the case of Doppler constant. This can be seen in Figure 3.21. When decreasing the number of neutrons implemented, the difference in the axial profiles produced is not extremely significant.

Additionally, the discretization adopted must be adequate to the statistics chosen. The axial discretization of the core into 1, 2, 4, 10 and 20 zones to map the Doppler constant of all batches was further adopted. In each of

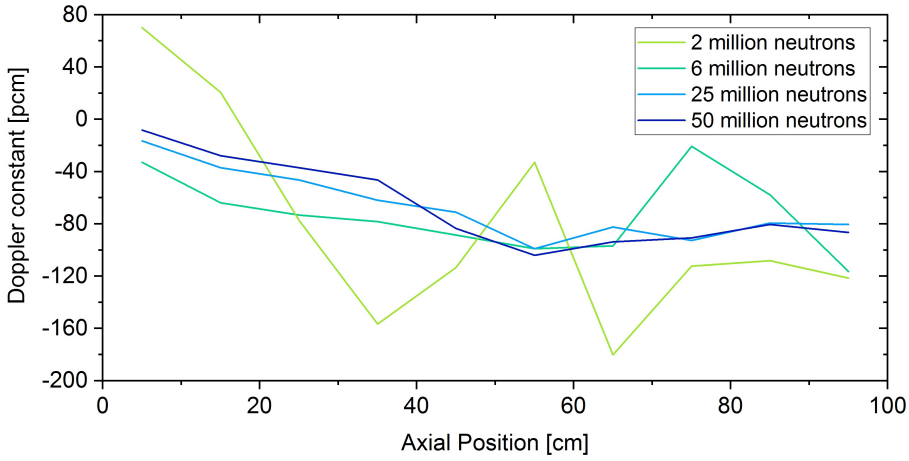

FIGURE 3.20: Axial Doppler constant profiles simulating the perturbed case with different neutron histories; the nominal state is simulated with 75 million neutrons

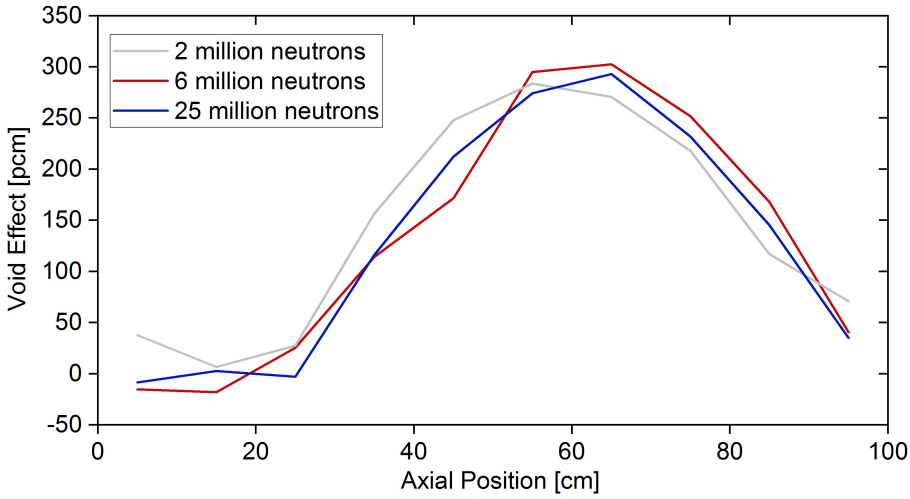

FIGURE 3.21: Axial void effect profiles simulating the perturbed case with different neutron histories; the nominal state is simulated with 75 million neutrons

these cases, the cumulative Doppler constant of the core was calculated. Figure 3.22a shows that refining the nodalization, the Doppler constant diverges strongly from the whole core value, especially when low statistics are implemented. Despite the absolute error is independent on the nodalization, as seen in Figure 3.22b, the relative error is not. It reaches up to 120% when the lowest statistics are used. However, for 20 axial nodes it is extremely high even for the highest statistics implemented, as seen in Figure 3.22c.

The relation between statistics implemented and error produced was derived for Doppler constant and void effect from the cases previously simulated, assuming that the neutron source is uniformly distributed inside the core. The global number of neutrons simulated was used as a measure of accuracy. Generally, the relative error steeply increases when the neutrons

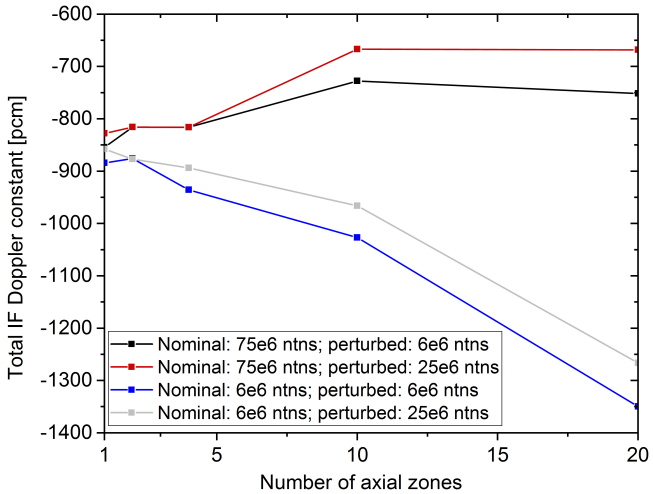

(A) Doppler constant

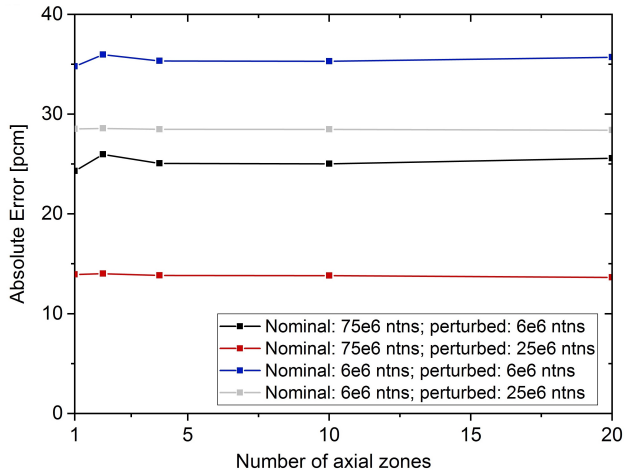

(B) Absolute Error

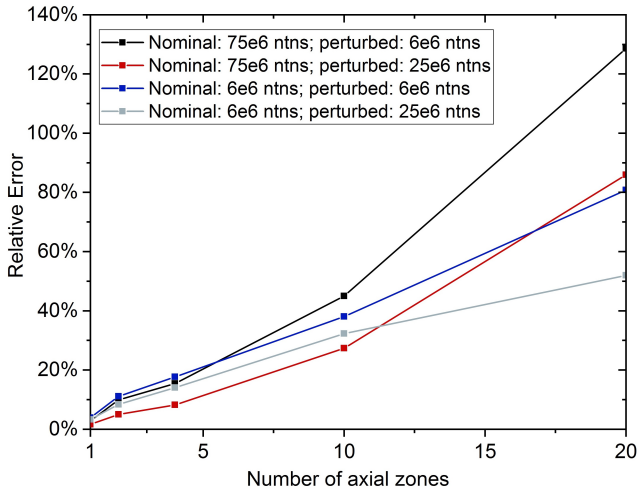

(C) Relative Error

FIGURE 3.22: Doppler constant, absolute and relative error produced by Serpent for different axial nodalizations

simulated per node decrease. In the Doppler constant case, 25 million neutrons per node are necessary to produce a relative error lower than 2%. If the

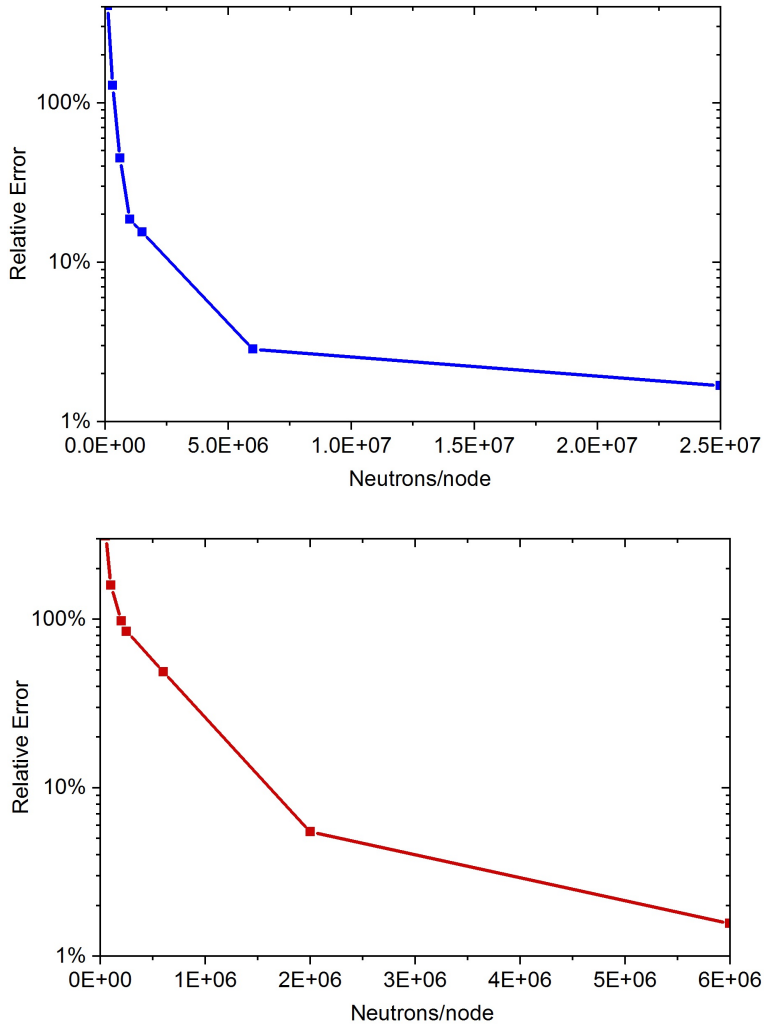

FIGURE 3.23: Average relative error as a function of the number of neutrons simulated per each perturbed node for Doppler constant (top) and void effect (bottom)

core is subdivided into 6 assemblies and 20 axial zones, for instance, 3 billion neutrons would be needed per each of the 120 perturbations simulated. For the void coefficient, 6 million neutrons per node are enough to produce a relative error lower than 2%. In case of 6 assemblies with 27 axial nodes, 972 million neutrons per each of the 162 simulations are needed. Clearly, the computational resources required would be extremely large.

Chapter 4

Application to Breed & Burn Molten Salt Reactor

In this Chapter, the second application of the BBP script is described. It is a parametric study aimed at reducing the dimensions of a Breed and Burn Molten Chloride Fast Reactor.

4.1 Molten Chloride Fast Reactor

The idea of a reactor with molten salt fuel and coolant dates back to the 1940s, when a military program for the development of nuclear powered aircrafts was launched at Oak Ridge National Laboratory. In the 1960s, when the program shifted from military to civilian purposes, the Molten-Salt Reactor Experiment took place. The first and only MSR ever built was a 8 MWth test reactor which operated for five years and provided valuable information, in particular about the corrosion driven issues of Hastelloy N [31]. Still nowadays, the experimental data collected at Oak Ridge are the basis of MSR research. In the following years, molten salt technology have received intermittent attention. Today, however, MSR has been selected as one of the most revolutionary Generation IV reactor. Features like the low vapour pressure of molten salts, the absence of integrity issues related to solid fuel and the possibility of online fuel reprocessing make MSR an attractive choice. As a consequence, MSR is now the focus of many international collaborations and projects, like Samosafer in Europe. Many different reactor concepts have been proposed; a classification is suggested in Figure 4.1.

The numerous concepts explore the possibility to operate in a fast or thermal neutron energy spectrum, with chloride or fluoride fuel salts, in an open or closed fuel cycle. The system studied in this work is a Molten Chloride Fast Reactor (MCFR) operated in Breed and Burn fuel cycle.

4.1.1 Breed & Burn fuel cycle

Generation II reactors, such as LWR, normally operate as converters: some fissile material is produced from the fertile, but the breeding ratio is smaller than one. Fast reactors, however, can profit from a better neutron economy and can be operated as breeders, i.e. they can breed more fissile material than

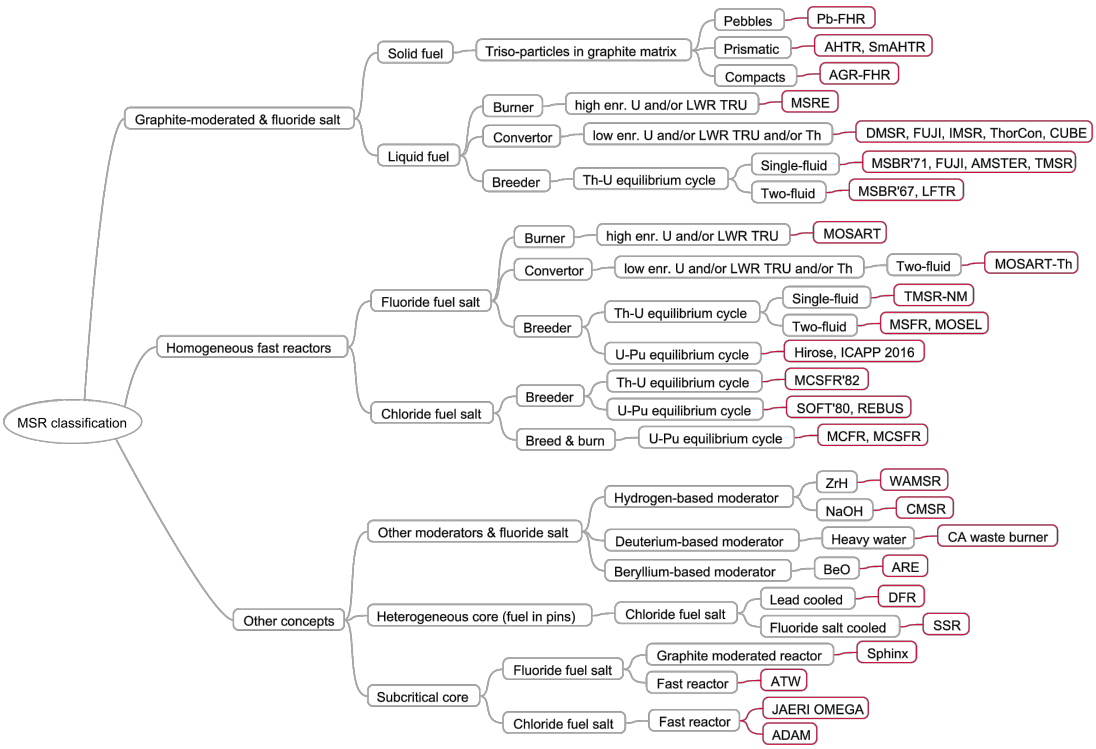

FIGURE 4.1: A Molten Salt Reactors classification

it is burnt. Breeders would drastically enhance fuel utilization and cycle sustainability if operated in a closed cycle. With an excellent neutron economy, extreme breeding can be achieved: if the fresh fuel feed is only fertile, the reactor can be operated in B&B mode, where all the fissile material to be burnt is bred inside the core. As a consequence, fuel enrichment at the front-end of the fuel cycle would be no longer necessary. Spent fuel from B&B operation could be disposed as waste or used as initial fuel for another reactor. In any case, fuel utilization can be extremely high even in an open once through cycle.

B&B operation mode can be applied in case of solid fuel, liquid fuel, and multi-liquid systems. An illustrative evolution of burnup in the different cases is represented in Figure 4.2. In case of solid fuel, each batch has a different burnup and at the end of each cycle the oldest fuel is replaced. In case of liquid fuel, however, fuel batches with different burnup are homogeneously mixed and not distinguishable. The spent fuel average burnup is based on the residence time of the different batches inside the core. In a multi-liquid reactor, e.g. in case of a fertile salt blanket around the fuel, fuel burnup is built up by moving the salt from a lower irradiation region to a higher irradiation one.

The current work focuses on a conceptual externally cooled pool type reactor with liquid homogeneous fuel operated with batch-wise refuelling. The same design has already been extensively studied under the assumption of continuous refuelling. The feasibility of B&B mode was proven by [16] and [33]; in [32], the performances of chloride and fluoride salts in Uranium and Thorium fuel cycles were compared through the PSI in-house EQL0D code.

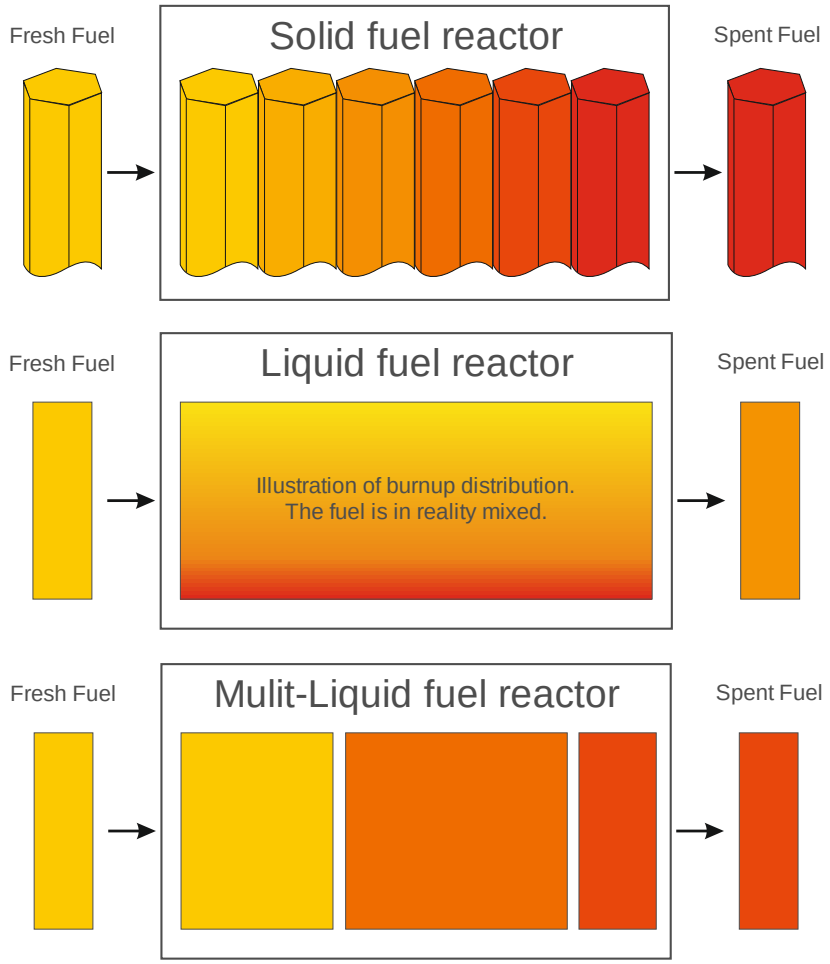

FIGURE 4.2: Breed and Burn burnup evolution in solid, liquid and multi-liquid fuel [32]

A comparison between a moderated and unmoderated two-fluid layout is proposed in [15]. Additionally, [34] has analysed the possibility of B&B in a Moltex dual-salt configuration, where the fuel is contained into cladded channels. In this Thesis, some of the previous studies were reproduced with the difference of batch-wise refuelling. Under the perspective of practical application, refuelling at the end of each cycle is more functional rather than continuous refuelling.

4.2 MCFR batch-wise operation model

This study concerns, in first place, the neutronic feasibility of a fast, externally cooled, homogeneous Breed and Burn reactor with batch-wise refuelling. For this purpose, the core is simulated as an infinite medium. Once the feasibility was assessed, an optimization of the dimensions of a finite geometry was performed. The influence of some parameters, such as the fuel salt composition, the modality of non-soluble fission products removal and the frequency of refuelling were studied. To reduce the size of the core, originally bulky

to compensate for the high neutron losses induced by leakage, other components were included in the design. An example is a fertile salt blanket positioned around the core, where fissile material can be bred, thus making use of the neutrons leaking from the active core. Also a thin moderating graphite layer was included, with the intent of reducing neutrons migration length.
The tool utilized was the previously introduced BBP script coupled with Serpent2. The task of BBP is to automatize refuelling between cycles for liquid homogeneous fuel. When a single-fluid reactor is simulated, the refuelling operation performed for each isotope i with atomic density n_i contained in the fuel takes place as reported in Equation 4.1.

$$n_i = n_i \cdot (1 - V\%_{removed}) + n_{i_{feed}} \cdot V\%_{removed} \tag{4.1}$$

where $V\%_{removed}$ is the volumetric share of fuel removed each cycle from the core. When one or more blankets were included in the simulation, a fixed volume V_{out} of salt is moved from one region to another. In the following equations, the blankets are distinguished by the subscript j, where $blanket_1$ is the most internal one and $blanket_m$ the most external.

$$n_{i_{fuel}} = (1 - \frac{V_{out}}{V_{fuel}}) \cdot n_{i_{fuel}} + \frac{V_{out}}{V_{fuel}} \cdot n_{i_{blanket_1}} \tag{4.2}$$

$$n_{i_{blanket_j}} = (1 - \frac{V_{out}}{V_{blanket_j}}) \cdot n_{i_{blanket_j}} + \frac{V_{out}}{V_{blanket_j}} \cdot n_{i_{blanket_{j+1}}} \quad j = 1, 2, 3, ..., m \tag{4.3}$$

$$n_{i_{blanket_m}} = (1 - \frac{V_{out}}{V_{blanket_m}}) \cdot n_{i_{blanket_m}} + \frac{V_{out}}{V_{blanket_m}} \cdot n_{i_{feed}} \tag{4.4}$$

Occasionally, batch-wise removal of the non-soluble fission products was performed by the BBP as well: during the preparation of the material input for a new cycle, the atomic density n_i of the selected products was replaced by zero.
Any repetitive batch-operation mode converges to equilibrium. Here, some of the equilibrium parameters were compared to evaluate the performance of the reactor, like k_∞ and $k_{effective}$ as a function of the equilibrium burnup. Since the fuel salt is considered to be continuously mixing, fuel batches with different burnup cannot be distinguished inside the core, thus the in-core fuel burnup is homogeneous. Burnup is an indication of the average residence time of all fuel batches inside the core. It increases with the cycle length and decreases with the refuelling rate: for high refuelling rates, the average time spent by the fuel inside the reactor is lower than in the case of low refuelling rates, hence burnup is lower. This can be observed in Figure 4.3.

From Figure 4.3 it can be noticed that the dependence between BU % FIMA (Fissions per Initial Metal Atom) and refuelling rate is $BU_{\%FIMA} \propto \frac{1}{V\%_{removed}}$. By definition, BU % FIMA is expressed as:

$$BU_{\%FIMA} \equiv \frac{N_{fissions}}{N_{InitialActinides}} \tag{4.5}$$

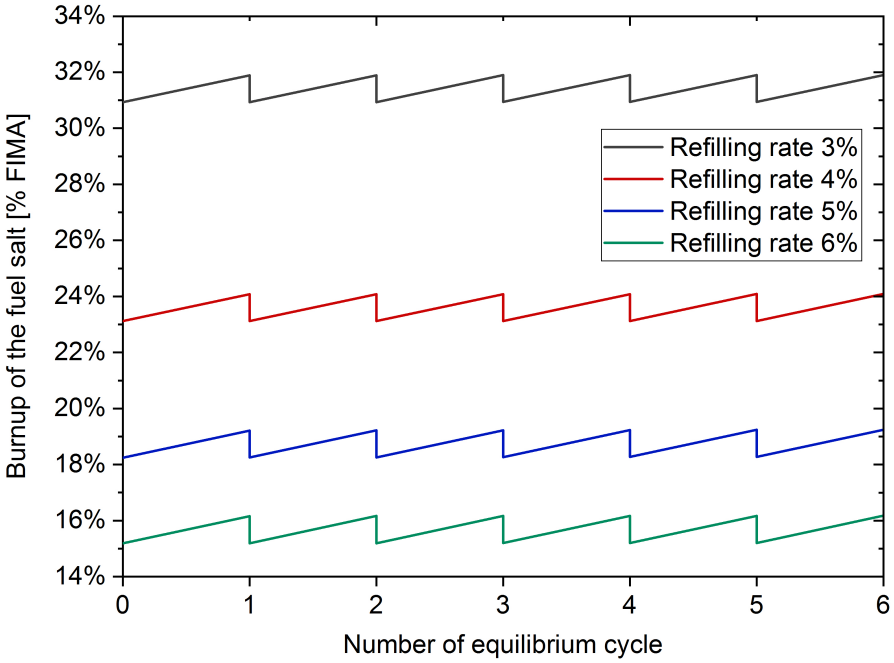

FIGURE 4.3: Relation between fuel salt equilibrium burnup and refuelling rate in % of salt volume removed each cycle

In case of batch-operation, the equilibrium burnup is the burnup of the equilibrium cycle divided by the refuelling rate [33] (Equation 4.6).

$$BU_{\%FIMA_Equilibrium} = \frac{BU_{cycle}}{V\%_{removed}} = \frac{N_{fissions/cycle}}{N_{Initial\,Actinides} \cdot V\%_{removed}} \tag{4.6}$$

Equation 4.6 can be rewritten as Equation 4.7, which is a balance between the number of actinides inserted and removed from the core (or from a blanket) at the end of an equilibrium cycle. In this work, the formulation in Equation 4.7 was applied for burnup calculation.

$$BU_{\%FIMA_Equilibrium} = \frac{N_{Actinides_{IN}} - N_{Actinides_{OUT}}}{N_{Actinides_{IN}}} \tag{4.7}$$

4.3 Cell-level simulation

In this section, the feasibility of B&B operation is assessed in the zero dimensional case, i.e. an infinite homogeneous medium. Due to the absence of leakage, the neutron economy in the infinite case is the best possible. At equilibrium, a B&B reactor converges to its isobreeding material composition. Therefore, feasibility is confirmed when there is positive reactivity at equilibrium, i.e. $k_\infty \geq 1$, because it means that the net neutron production is positive and the reactor can sustain itself as an isobreeder [5].
In this study, the infinite neutron multiplication factor is expressed as a function of the average burnup of the discharged fuel. Infinite core performances

with different fuel salts were compared. The modality of non-soluble fission and decay products was studied, as well as the time span between consecutive refuelling outages.

4.3.1 Fuel salt types

Previous studies have demonstrated that chloride salts perform neutronically better then fluorides in B&B mode [32]. In particular, chlorine isotopically enriched with ^{37}Cl is favourable, since ^{37}Cl neutron capture cross-section is within one and two orders of magnitudes lower than the one of ^{35}Cl [35]. For this reason and for simplicity, in this study chloride fuel salts are fully composed by ^{37}Cl. The salts simulated have the compositions and densities reported in table 4.1: a pure Uranium salt, a Thorium salt and a mixed one were used to compare different fuel cycles. Among them, the Thorium salt is the most convenient in terms of melting temperature.

TABLE 4.1: Salt compositions studied

Salt composition	Atomic Fractions	Density [$\frac{g}{cm^3}$]	Melting Point [°C]
NaCl - UCl_3	60% - 40%	3.64	590
NaCl - $ThCl_4$ - UCl_3	55% - 25% - 25%	3.16	500
NaCl - $ThCl_4$	55% - 45%	3.15	375

All the mixtures were initially 10% enriched. However, it was previously demonstrated that the equilibrium state does not depend on the initial fuel composition, but only on the fuel feed [7]. From the second cycle on, the fresh feed was composed only by fertile materials, i.e. ^{238}U and/or ^{232}Th.
From Figure 4.4, it can be observed that k_∞ is very low for low average salt burnups. In fact at equilibrium, fuel burnup has to be large enough to allow sufficient breeding of fissile material to sustain the chain reaction. At the same time, the neutron multiplication factor decreases steeply for high burnups, because the core is poisoned with fission products and the fuel has already been partially depleted. The maximum occurs in a mid-burnup range, between 30% and 40% FIMA. However, fuel utilization is higher at high burnup: therefore, the best operation mode is when fuel achieves the highest burnup at which $k_\infty > 0$.
From Figure 4.4, it can also be noticed that with pure Thorium salt, criticality is not reached for any range of burnup. Between pure Uranium and mixed Uranium and Thorium cycle, the former is the best performing and it could be operated between 13% and 49% FIMA. The mixed Uranium and Thorium cycle could be operated in the burnup range between 15% and 49%.
It must be noticed that these simulations included continuous exponential non-soluble products removal with time constant $\tau = \frac{1}{30s}$. More details about non-soluble fission products strategies are provided in the next section.

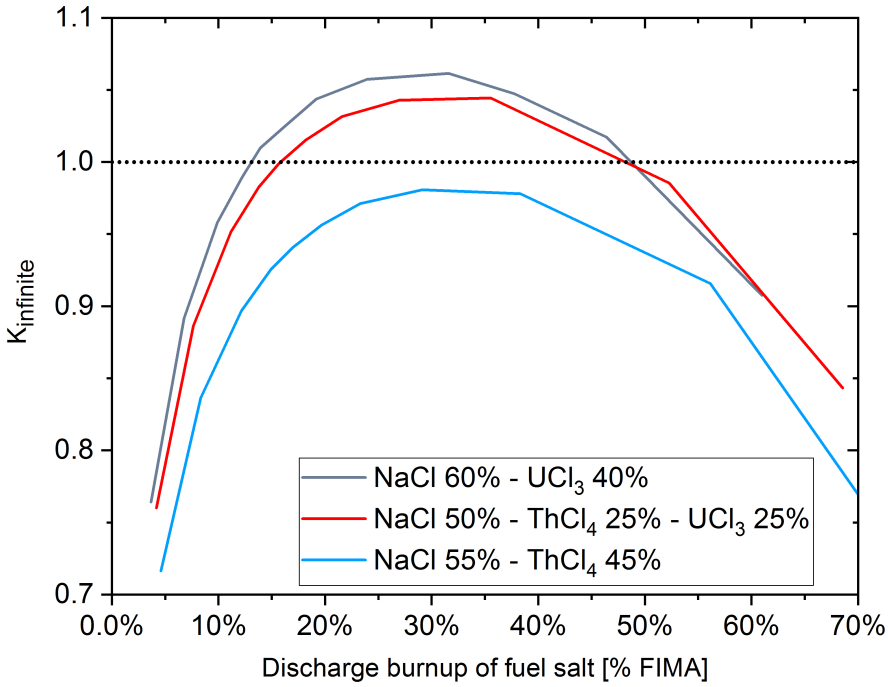

FIGURE 4.4: k_∞ as a function of average burnup of the discharged fuel for different salt compositions

4.3.2 Non-soluble fission products removal strategy

When actinides are fissioned, they generate fission products (FP) which mainly dissolve in the salt mixture. However, some fission and decay products are non-soluble and can be physically separated from the salt. Those elements are, for example, some of the noble gases and volatile products such as He, Ne, Ar, Kr and Xe. Also some metals and semi-metals are included, like Nb, Mo, Tc, Ru, Te, Sb. Other non-soluble elements can be found in [36]. Physical separation of non-soluble elements could be achieved through Helium bubbling. Helium bubbles are sprayed inside the core and trap the undissolved products. Then, helium bubbles with the captured products are discharged to the off-gas system. If helium bubbling is not employed, all the fission products remain in the core for the whole duration of the cycle. At the end of each cycle, they could either be removed during the fuel outage or simply stay in the core. Reprocessing of soluble fission products, on the contrary, has not been included in this work.
From a simulation point of view, the three cases listed above can be distinguished as described:

- Continuous products removal, characterized by a time removal constant τ, was applied through an extension of Serpent2 implemented appositely for reprocessing in liquid fuel systems. A fictitious exponential decay term for the selected isotopes was added to the depletion equation. In nominal conditions, the effective removal time constant most frequently found in literature is $\tau = \frac{1}{30s}$ [36] [37].

- Cycle-wise products removal, taking place at the end of each cycle, can be simulated through the BBP script.
- No removal: all the fission and decay products remain homogeneously distributed in the core.

The three situations just depicted are compared in Figure 4.5, where Uranium chloride is used as fuel. Refuelling is taking place batch-wise in all the situations included in this study.

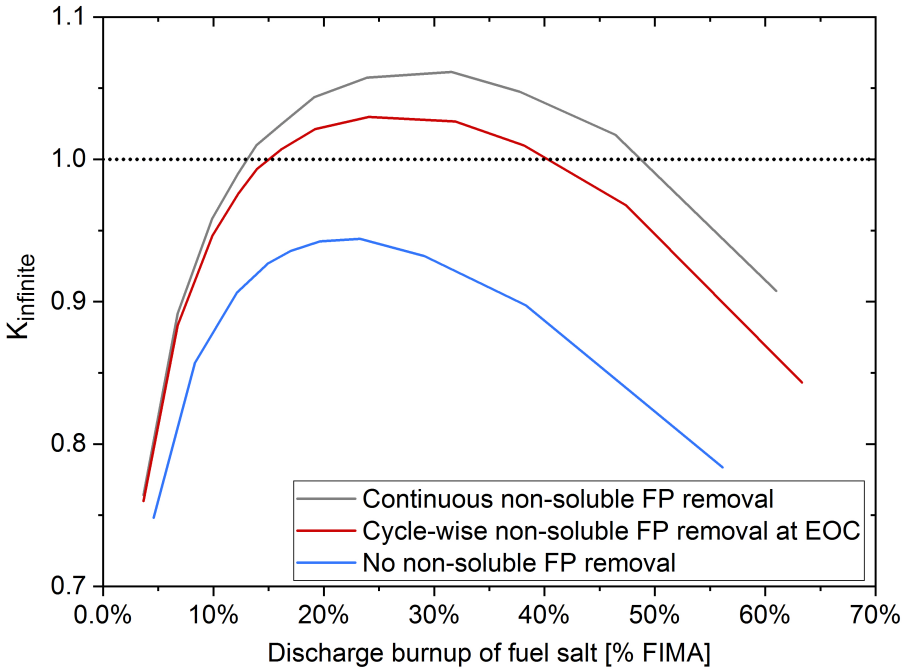

FIGURE 4.5: k_∞ as a function of average burnup of the discharged fuel for different modalities of non-soluble products removal

B&B operation without any fission products removal would not be possible in any range of burnup. However, operation feasibility is confirmed if batch-wise or continuous removal are implemented. Continuous removal is the best option: many of the non-soluble fission products are strong parasitic absorbers. Removing them from the core throughout the cycle produces a noticeable positive reactivity insertion. Additionally, some of the non-soluble products are unstable, and they could decay or be transmuted into a soluble element which cannot be separated from the salt unless an expensive reprocessing process is taking place. If fast continuous removal is taking place, most decays happen outside of the core. Consequently, the difference between each removal case and the others is more evident for high burnups, since the soluble products generated by decay or transmutation of the unremoved non-soluble fission products remain in the active core for a longer time.

4.3.3 Non-soluble fission products removal frequency

A sensitivity study on the frequency of non-soluble fission products removal has been carried out. In the batch-wise removal case, the cycle length was varied, whereas in the continuous removal case the removal time constant τ was varied. The average amount of non-soluble fission products contained in the core was used as a parameter to compare the two removal modalities. The cases included in the study are summarized in Table 4.2. All the data presented refer to the equilibrium state and to a burnup of approximately 24% FIMA.

TABLE 4.2: Non-soluble fission products removal cases studied

Removal modality	**Characteristic Time**
Cycle-wise	1/2 year 1 year 2 years
Continuous	$\frac{1}{30s}$ $\frac{1}{300s}$ $\frac{1}{30000s}$ $\frac{1}{3000000s}$

Figure 4.6 shows the time evolution of the non-soluble fission products content inside the core in the different cases. In the case of cycle-wise removal, the fission product concentration grows linearly throughout the cycle, as demonstrated by simulating different refuelling intervals. As a consequence also the fission products average mass, i.e. the mean value of the masses at BOC and EOC, grows linearly with the cycle length. In the continuous removal case, the time constants simulated differ by several orders of magnitude, as well as the fission product masses in the core at equilibrium. Strong variations were necessary in order to notice a difference in the neutronics performances of the four cases. When the nominal time removal constant, $\tau = \frac{1}{30}$, is adopted, the average non-soluble FP mass inside the core is 1.1E-07% of the total fuel mass. It is a negligible quantity, considering that when non-soluble fission products are not removed from the fuel their mass fraction is 5.8%. Therefore, continuous removal with $\tau = \frac{1}{30}$ is the most effective of the removal strategies considered. Table 4.3 summarizes the average non-soluble fission products content of each case: continuous products removal is consistently more efficient than cycle-wise removal, even after decreasing significantly the time removal constant.

Using the average non-soluble FP mass inside the core as a correlation parameter, the cases with cycle-wise and continuous removal can be compared. The cases with continuous removal can be associated to a fictitious cycle length, which would leave the FP mass in the core unaltered if the removal was cycle-wise. The results are shown in Table 4.4.

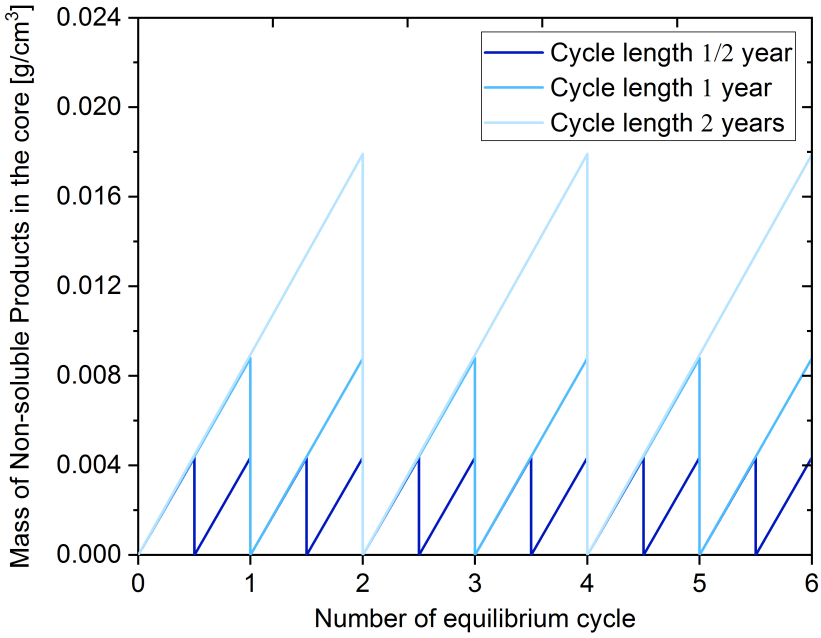

(A) Cycle-wise removal

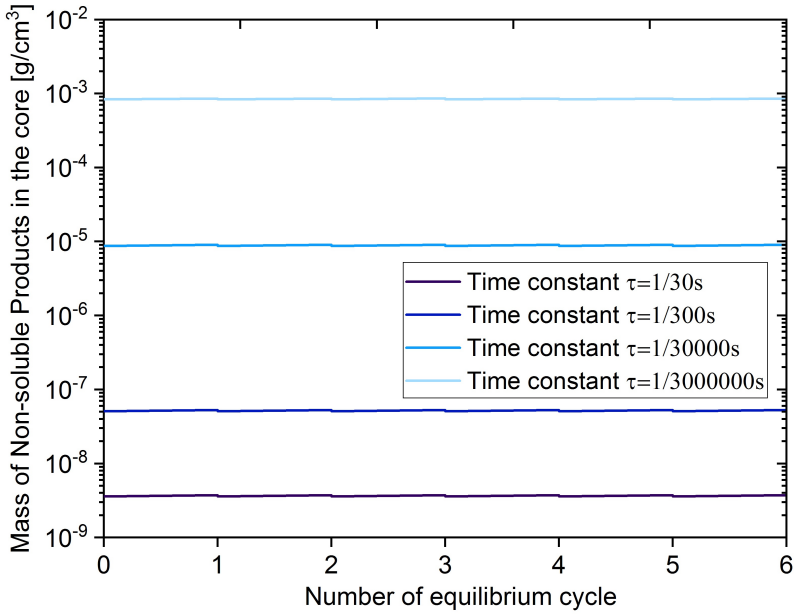

(B) Continuous removal

FIGURE 4.6: Mass of non-soluble fission products in the core at equilibrium with different non-soluble products removal strategies and equilibrium burnup 24% FIMA

As already mentioned, continuous removal with $\tau = \frac{1}{30}$ is the best case achievable, i.e. fast and almost complete non-soluble fission product removal from the core. To achieve such performances with cycle-wise removal, each cycle should be 26 second long. This is, of course, unpractical and unrealistic. On the contrary, the case without any fission products removal shown in Figure 4.5 would correspond to a cycle 50 years long with cycle-wise removal.

TABLE 4.3: Comparison between average mass of non-soluble fission products in the core at equilibrium, maximum $k_{infinite}$ and maximum burnup with positive reactivity for several removal modalities; in all cases, refuelling is taking place batch-wise

Non-sol FP removal mode		**In-core FP mass [$\frac{g}{cm^3}$]**	**Max k_{inf}**	**Max BU [FIMA]**
No removal		2.12E-01	0.94411	19%
Cycle-wise	2 years	8.96E-03	1.02631	40%
	1 year	4.40E-03	1.02979	40%
	1/2 year	2.18E-03	1.03222	40%
Continuous	τ=1/3000000s	8.45E-04	1.03628	41%
	τ=1/30000s	8.90E-06	1.05310	46%
	τ=1/300s	5.18E-08	1.05653	48%
	τ=1/30s	3.68E-09	1.06142	49%

TABLE 4.4: Cycle length corresponding to continuous removal constant τ

τ [s^{-1}]	**Corresponding cycle length with cycle-wise non-soluble FP removal**
1/30	26 seconds
1/300	6.2 minutes
1/30000	17.7 hours
1/3000000	70.1 days
0	$\approx$ 50 years

The neutronic comparison between all cases, expressed as k_∞ as a function of burnup, can be seen in Figure 4.7. Neither continuous nor cycle-wise removal are sensitive to small variations of respectively τ and of the cycle length. The cycle length span studied has a maximum deviation of a factor 4, and the maximum k_∞ of all cases are very similar: it varies from 1.02631 to 1.03222. The maximum burnup which allows operation is approximately 40% in all cycle-wise removal cases. The range of time constants considered in the continuous removal case was as large as 10^5. The k_∞ for these cases varies from 1.03628 to 1.06142, while the maximum burnup with a positive equilibrium reactivity varies from 40% to 49%.
In all the future work, a cycle length of one year and continuous FP removal with the nominal time constant $\tau = \frac{1}{30}$ has been applied.

4.4 Core-level simulation

Once the neutronic feasibility of the B&B MCFR design considered was assessed, a geometry optimization was carried out. In fast MSR fuelled by chloride salts neutron leakage has a large impact. The neutron migration

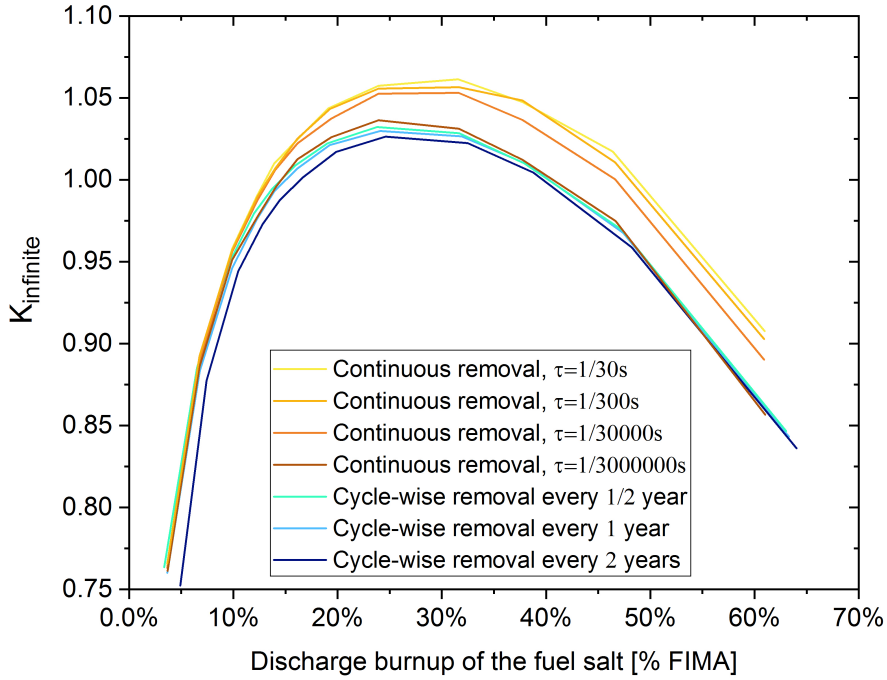

FIGURE 4.7: Comparison between the neutron multiplication factor as a function of burnup of the discharged fuel for different non-soluble fission products removal modalities

length in chlorides is high because of the modest scattering cross section and of the high atomic number of ^{37}Cl, compared to the usual moderator materials such as water and graphite. Since B&B operation requires an excellent neutron economy, a very large core may be necessary to compensate for the losses. However, a too large core is unpractical and excessively expensive, thus a geometry optimization is necessary.

4.4.1 Minimal critical core dimensions

In this section, the minimal critical core dimension in a reduced burnup range was investigated. The geometry selected is a cylinder with proportions $\frac{D}{H} = 0.92$, proven to be optimal by diffusion theory. The fuel salt is surrounded by a 2.5 cm thick wall of Hastelloy. The selected configurations are a bare reactor, and a reactor surrounded by a one meter thick reflector. Two reflector materials were considered, lead and Hastelloy. The $k_{effective}$ as a function of the core diameter was analysed for the three cases, varying the equilibrium burnup within the interval where the infinite core from the previous section had positive equilibrium reactivity. The results can be seen in Figure 4.8. The neutron multiplication factor grows with the core diameter. The optimal burnup, among the cases considered, is 32% FIMA for all configurations. The results of this study are summarized in Table 4.5. The introduction of a reflector allows to reduce considerably the core size. Between Hastelloy and naural lead, the latter guarantees the best performance.

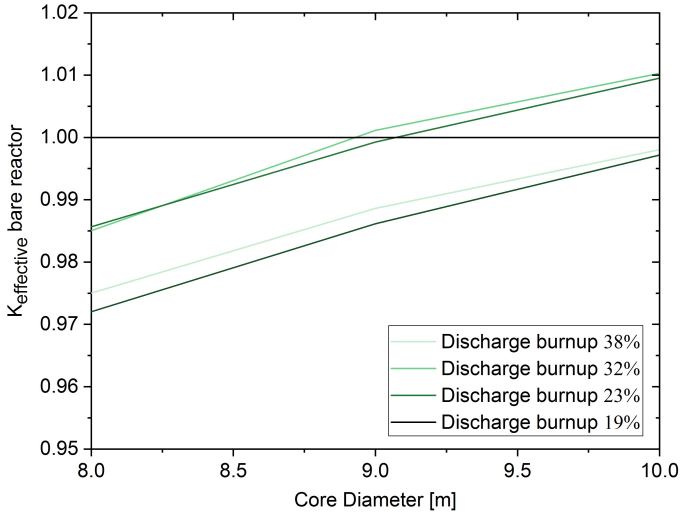

(A) Bare reactor

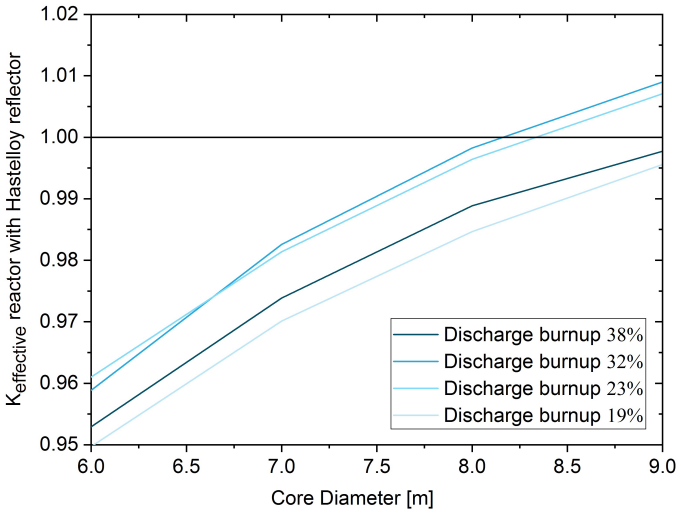

(B) With Hastelloy reflector

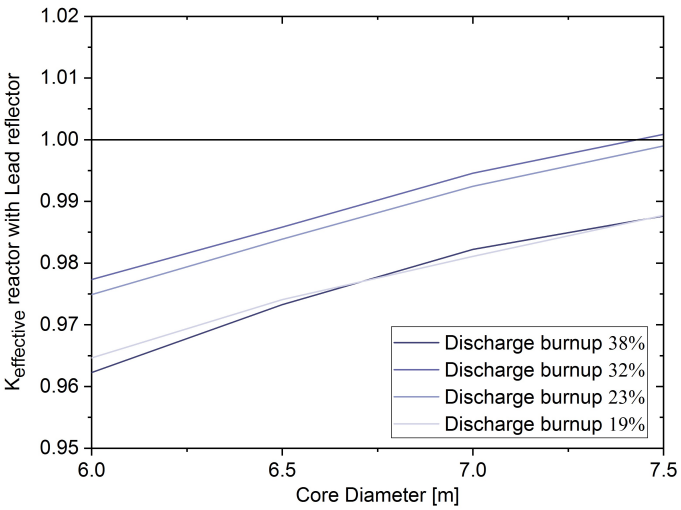

(C) With lead reflector

FIGURE 4.8: $K_{effective}$ dependence on core diameter for different fuel discharge burnups

TABLE 4.5: Minimum critical core dimensions at optimal equilibrium burnup

	Optimal BU [FIMA]	Diameter [m]	Volume [m^3]
Bare reactor	32%	9	527
Hastelloy reflector	32%	8.2	398
Lead reflector	32%	7.5	305

Nevertheless, even the smallest core volume achieved, 305m^3, is too large for practical applications. A two-fluid layout was adopted to reduce the core dimensions.

4.4.2 Two-fluid layout

A fertile salt blanket can be added between the core and the reflector, to make use of the neutrons leaking outside of the core. Fissile material is bred inside the blanket during irradiation; at the end of each cycle, the core is refilled with the salt from the blanket and the blanket is refilled with fresh fertile feed. The blanket can effectively limit neutron leakage when its equilibrium reactivity is negative, in which case the radial neutron flux decays exponentially towards the periphery. Additionally, the blanket burnup must be low to prevent the blanket from acting like a burner, depleting the fissile material bred and accumulating poisonous fission products. Three parameters were investigated: the core volume, the blanket volume and the total salt burnup. The core volumes simulated are 100 m^3, 200 m^3 and 300 m^3; the blanket volumes 50 m^3, 100 m^3, 150m^3 and 250 m^3. Figure 4.9 is an in-scale representation of the geometries considered.

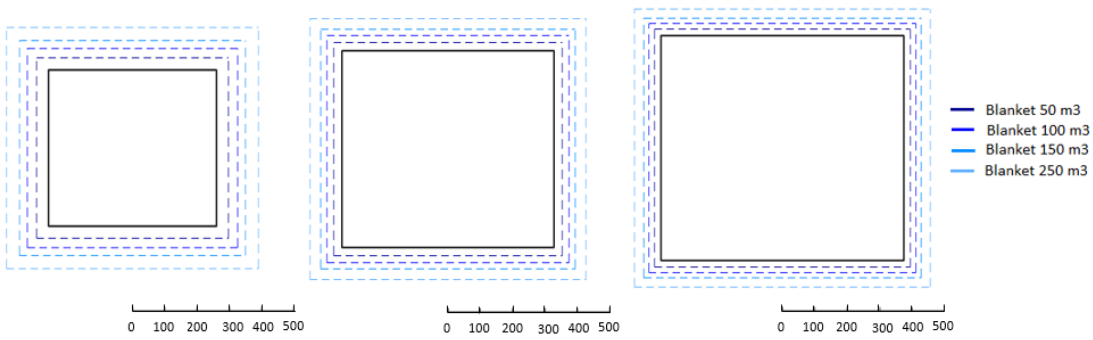

FIGURE 4.9: In scale geometries with four blanket possibilities: 50 m^3, 100 m^3, 150 m^3 and 250 m^3. From left to right the active core volume is 100 m^3, 200 m^3 and 300 m^3; the scale is in cm

The system was optimized in terms of $k_{effective}$, core dimensions and total salt inventory, which is strictly related to the fuel burnup achieved. Although using the burnup which corresponds to the maximum $k_{effective}$ can allow reducing the core size, a higher burnup would decrease the total salt inventory over time, thus improving fuel utilization. The burnups simulated were 22%, 33% and 44%. The dependence of $k_{effective}$ on the total burnup and on the blanket volume is shown in Figure 4.10 for different core volumes.

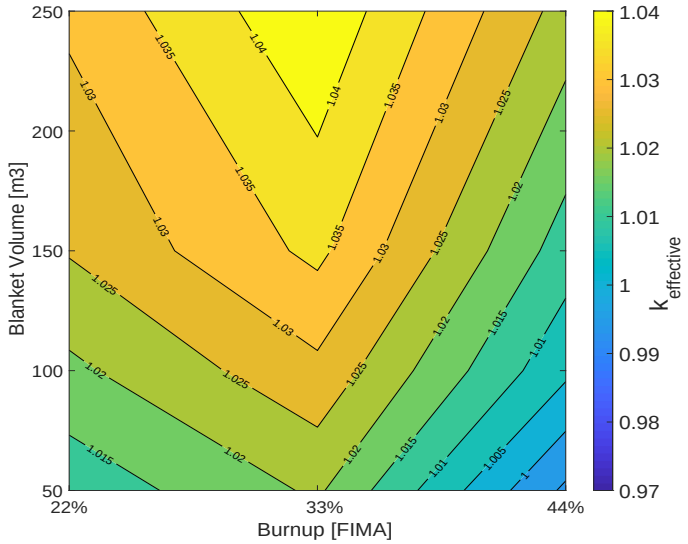

(A) 300 m^3

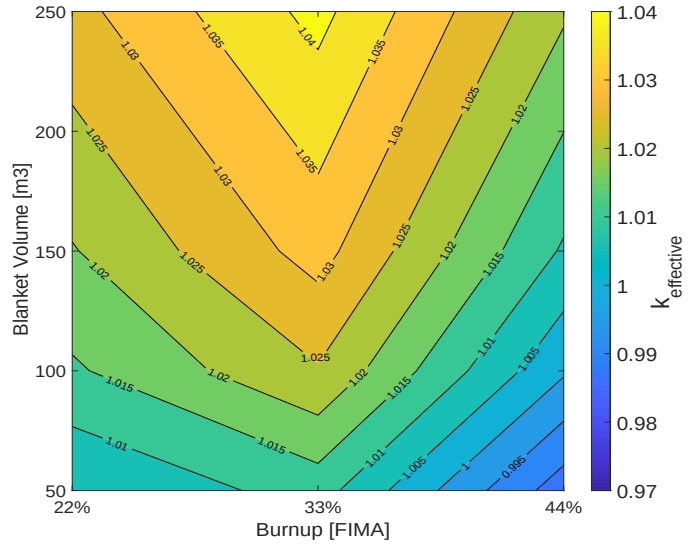

(B) 200 m^3

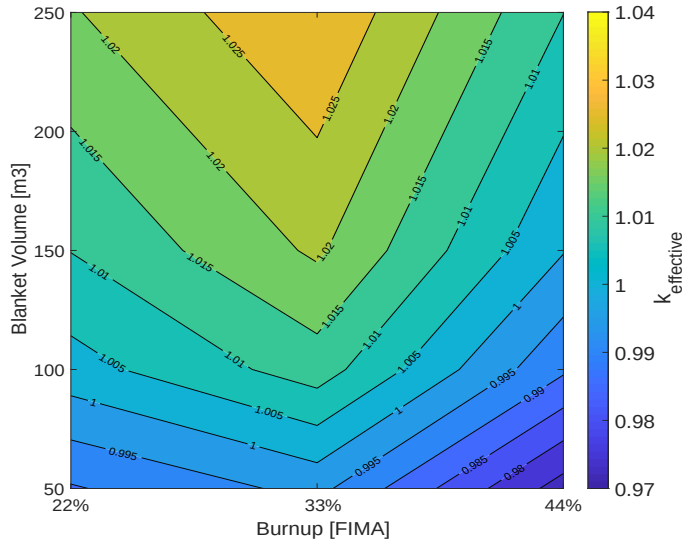

(C) 100 m^3

FIGURE 4.10: $K_{effective}$ dependence on blanket volume and total burnup for different active core volumes

The effective neutron multiplication factor of the system decreases with decreasing blanket and active core volumes, because of the increasing neutron leakage. The smallest configuration simulated with positive reactivity at equilibrium is composed by 100 m^3 of active core and 100 m^3 of blanket. Among the three burnups simulated, the best equilibrium composition is the one burnt up to 33% FIMA. However, the burnup ensuring the best performance is included between 22% and 33%. Figure 4.11 is a representation of the results where the impact of the total dimensions of the system on $k_{effective}$ is explicit.

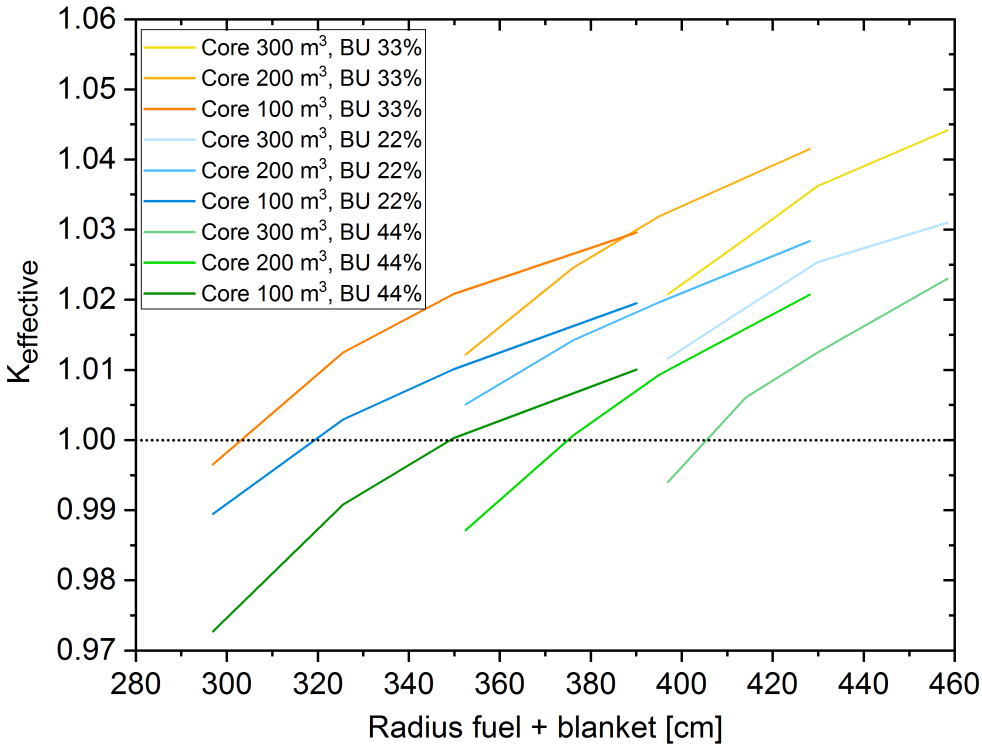

FIGURE 4.11: $K_{effective}$ dependence on the outer blanket radius for different burnups and active core volumes

From Figure 4.11 and Figure 4.12 it can be noticed that between two combinations with the same radius, the one with smaller active core and bigger blanket is the most performing. A bigger blanket enhances the core neutronic performance because the blanket burnup increases with the blanket volume: the residence time of the salt in the blanket is proportional to the number of cycles it takes to substitute the whole volume. The blanket burnup of all the geometries studied ranges from 0.2% to 18%. Within this interval the $k_{infinite}$ of the blanket, as well as the atomic density ratio $\frac{^{239}Pu}{^{238}U+^{240}Pu}$, shown in Figure 4.13, grow with burnup. Therefore, a higher burnup is associated with a higher concentration of fissile material, which is fed into the active zone increasing its equilibrium reactivity. On the other hand, considering the results presented in Chapter 4.3, the infinite neutron multiplication factor of the blanket salt is expected to reach a maximum and then decrease with growing

burnup. A too high burnup would in fact be connected with fission material depletion and high fission products density: the blanket would act as a burner rather than like a breeder. Consequently, also the $k_{effective}$ curves for constant active core volume of Figure 4.11 are expected to peak and descend by increasing further the blanket volume.

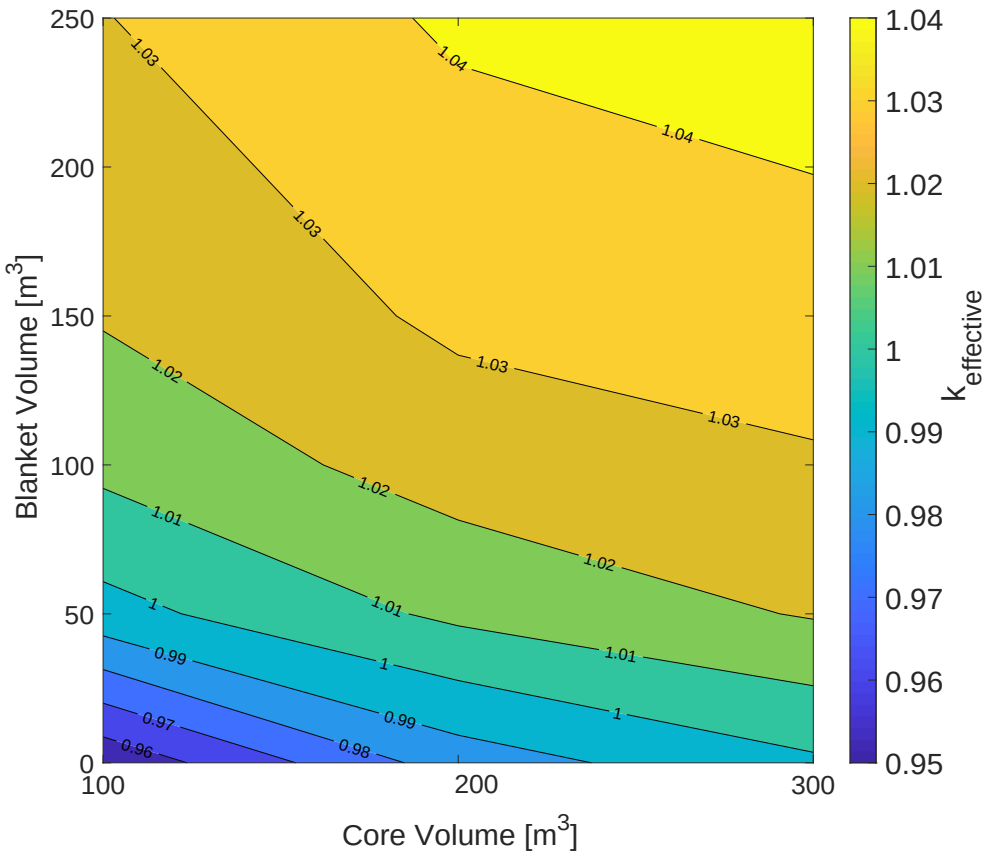

FIGURE 4.12: $K_{effective}$ dependence on active core and blanket volume for total fuel burnup 33%

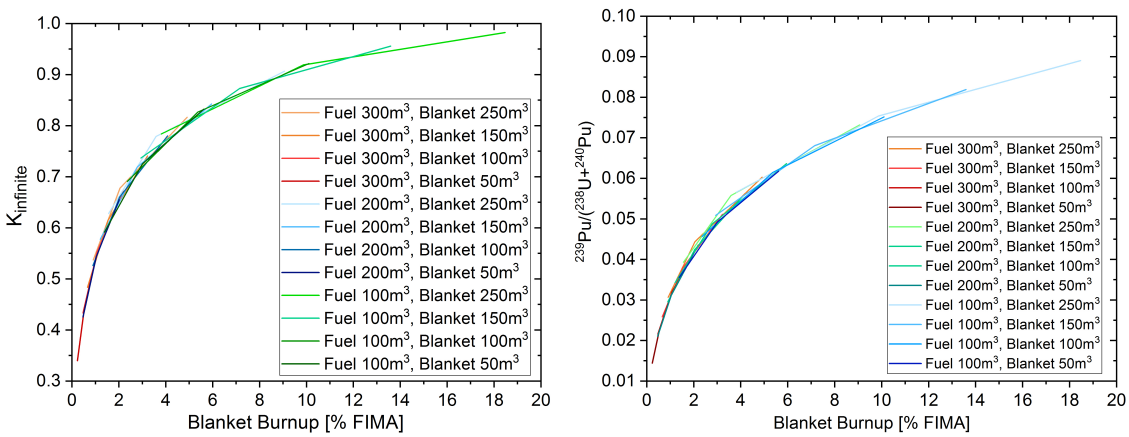

FIGURE 4.13: Blanket $k_{infinite}$ (left) and fissile to fertile mass ratio (right) dependence on blanket burnup

Figure 4.12 also shows that the reactivity of smaller active cores is more sensitive to variations in the blanket volume. Small cores suffer from a high neutron leakage that is mitigated within the blanket thickness. The blanket thickness, however, is more variable for small cores than for large ones when the same blanket volumes are adopted.
A further dimension reduction, with respect to the minimal critical reactor volume identified previously, i.e. 200 m^3, was attempted. An active core of 75 m^3 was modelled with blankets of 100 m^3, 75 m^3 and 50 m^3 and total burnups of 27%, 29%, 31% and 33%. The case with total volume 175 m^3 still shows positive reactivity at equilibrium, as shown in Figure 4.14.

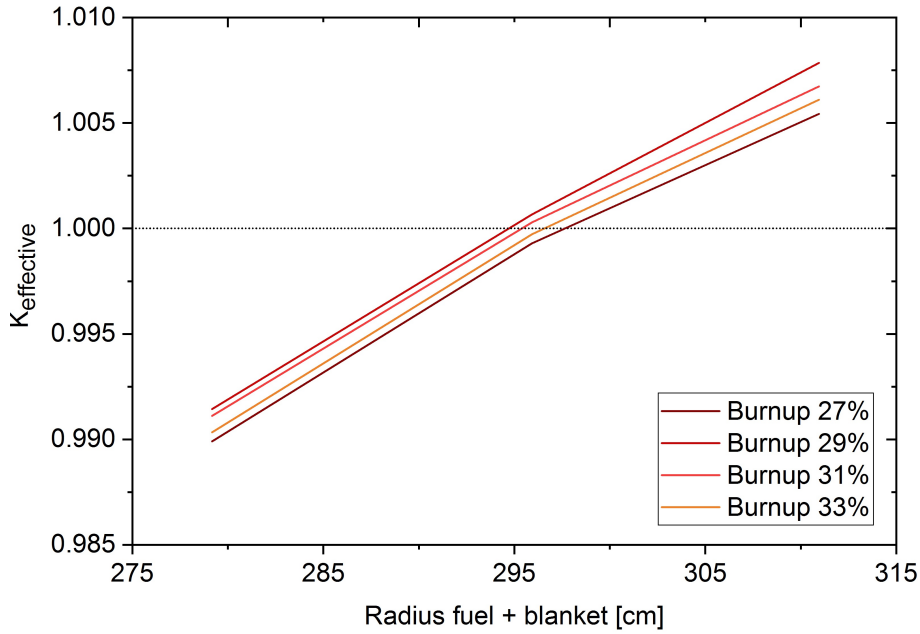

FIGURE 4.14: $K_{effective}$ dependence on the outer blanket radius for different total burnups and an active core volume of 75 m^3

The optimal equilibrium composition is obtained burning the salt up to 29% FIMA. On the other hand, considering that the total salt inventory is minimized at high burnup, the optimal burnup must a compromise between good performances and high fuel utilization. In the case of the reactor composed of 75 m^3 of active core and 100 m^3 of blanket, for example, the reactivity difference between the cases with burnup 29% and 33% is 170 pcm and the difference in salt inventory accumulated in 100 years of operation is roughly 35 m^3. Generally, the optimal burnup must be calculated following a cost and safety analysis based on these parameters.
Overall, the addition of the blanket has a large impact on the neutronic performance of the B&B MCFR: due to the better neutron economy achieved, the total salt volume could be reduced by more than 40% compared to the single-fluid configuration.

4.4.3 Multi-fluid layout

The radial neutron flux distribution could be optimized in a multi-fluid layout. Introducing small external salt blankets with low burnup and low $k_{infinite}$, the neutron flux at the periphery of the reactor would be reduced, thus neutron leakage would be mitigated. This study was conducted for two setups: a reactor with total volume 150 m^3, made of 75 m^3 of active core and 75 m^3 divided into one, two (50+25 m^3) or three (35+20+20 m^3) blankets and a reactor with total volume 200 m^3, composed by 100 m^3 of active core and 100 m^3 of salt divided into one, two (50+50 m^3) or three (50+25+25 m^3) blankets. Refuelling is taking place from an outer region to the neighbouring inner region. Figure 4.15 is a representation of the three multi-fluid designs described.

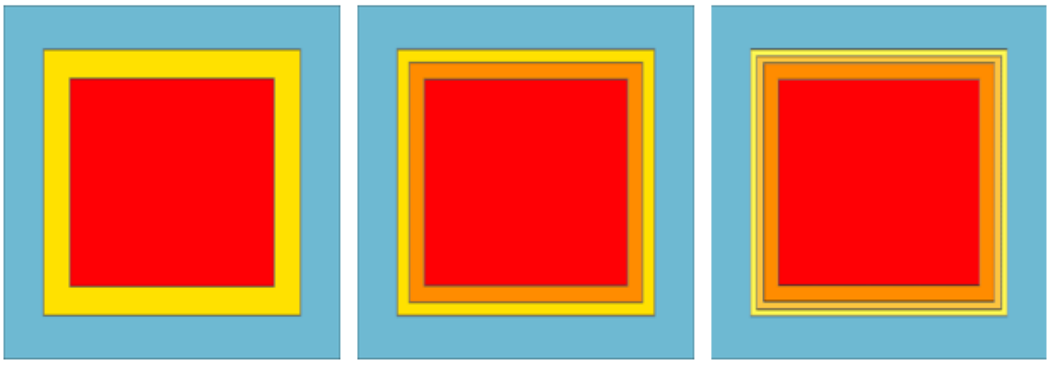

FIGURE 4.15: Representation of reactor with one, two and three salt blankets. The active core is in red while the lead reflector is in light blue

Table 4.6 summarizes the results obtained. Increasing the number of blankets, the fuel utilization in the core region increases whereas the salt burnup in the blankets decreases. The same effect is reflected on the $k_{infinite}$ of the salt in the active core and in the blankets, and on the radial neutron flux, shown in Figure 4.16. Increasing the number of blankets, the radial flux buckles more prominently in the centre and decays faster in the periphery. The reduction of the neutron flux in the blanket peripheries is beneficial in the transition from one to two blankets, in which case the core reactivity increases by approximately 90 pcm and 110 pcm in the two cases studied. In the three blankets case the total leakage is slightly reduced as well. However, each layer of salt must be contained in a 2.5 cm thick vessel made of Hastelloy. Increasing the number of blankets, the amount of Hastelloy per salt unit volume increases, and so do the parasitic captures of the system. When three blankets are simulated the additional captures from the supplementary Hastelloy prevail on the improved leakage, and the whole core reactivity decreases by roughly 270 pcm and 210 pcm in the two cases.

4.4.4 Impact of moderation

The effect of a moderating material has been studied in the two-blanket layout with total volume 200 m^3, composed by 100 m^3 of active fuel and by

TABLE 4.6: Comparison between neutronic performances of different multi-fluid layouts

	Total Volume 150 m^3			**Total Volume 200 m^3**		
	1 Blank	2 Blank	3 Blank	1 Blank	2 Blank	3 Blank
$K_{effective}$	0.9997	1.0006	0.9979	1.0125	1.0136	1.0115
Reactivity	-28	62	-206	1236	1346	1136
BU fuel	27.6	28.6	29.2	28.2	29.3	29.6
BU blanket 1	6.2	4.5	3.4	5.4	3.2	3.1
BU blanket 2	-	0.5	0.6	-	0.8	0.4
BU blanket 3	-	-	0.2	-	-	0.1
K_{inf} fuel	1.1190	1.1246	1.1264	1.1187	1.1251	1.1231
K_{inf} blanket 1	0.8977	0.9267	0.9251	0.8768	0.8993	0.8926
K_{inf} blanket 2	-	0.4984	0.6135	-	0.5617	0.5519
K_{inf} blanket 3	-	-	0.3948	-	-	0.3565
Hastelloy capt.	1.39E19	1.71E19	1.96E19	1.54E19	1.86E19	2.14E19
Leakage	5.12E18	3.33E18	2.31E18	5.20E18	3.14E18	2.26E18

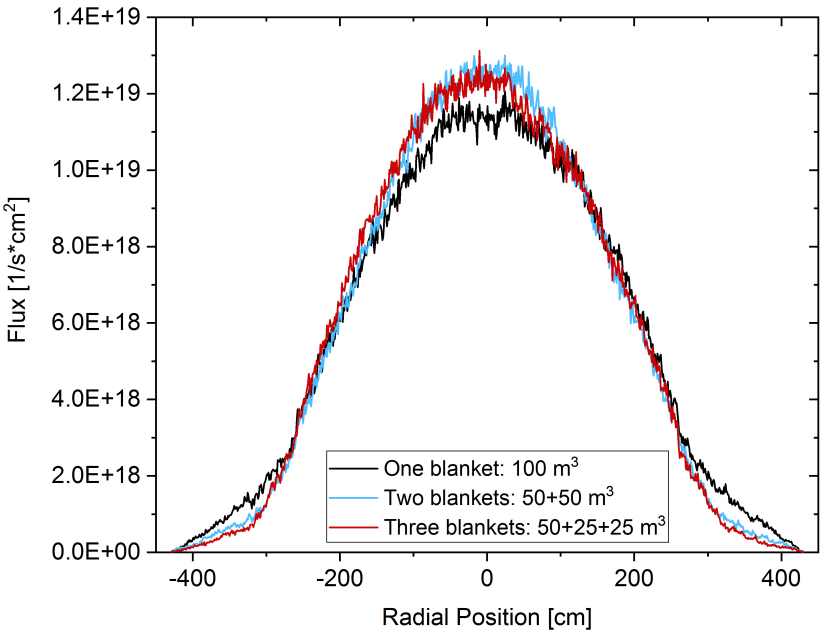

FIGURE 4.16: Radial flux distribution of different multi-fluid layouts, in the case with total volume 200 m^3

two blankets of 50 m^3 each. Moderation could improve the overall neutronic performance by increasing neutron scattering in the chloride salts, thus reducing neutron migration length and leakage. At the same time, a softer spectrum increases parasitic captures in structural materials and in the salt, modifying the equilibrium composition and the fissile to fertile atomic ratio, i.e. $^{239}Pu/^{240}Pu$ [38]. To limit this effect, the moderator was introduced in the blanket with the lowest burnup, the most external one, as shown in Figure 4.17. The total dimension of the reactor was unchanged, which implies that the second blanket salt volume was reduced. Two different moderating

materials were considered: graphite and Hastelloy.

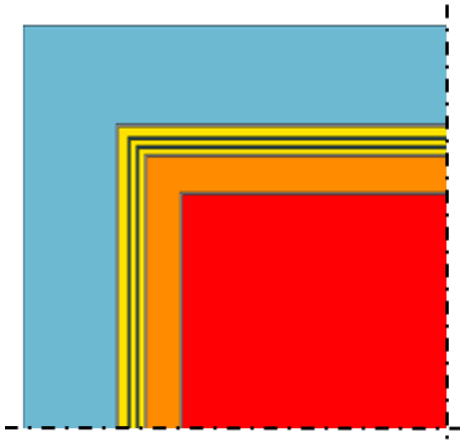

FIGURE 4.17: Representation of a two-blanket layout with two moderating shells in the most external blanket

A comparison between the neutronics of the unmoderated case and the graphite and Hastelloy moderated cases is shown in Table 4.7. In Figure 4.18, the radial flux distributions for all the cases investigated are presented. In the two-blanket design simulated, moderation largely deteriorate the equilibrium reactivity. In the moderated cases the flux is flatter in the periphery of the core, and leakage is lower. However, reduced leakage is not sufficient to compensate for the extra losses due to the increased captures by ^{239}Pu and structural materials in a softer spectrum. Fuel utilization in the second blanket improves poorly in the graphite moderated case and it decreases with Hastelloy moderation. The $k_{infinite}$ in the fuel and in the blankets diminishes in both cases. The difference between Hastelloy and graphite is driven by the large parasitic Hastelloy captures. On the contrary, graphite introduces negligible additional captures.

TABLE 4.7: Comparison between neutronic performances of differently moderated two-blanket designs

	No Moderation	Graphite	Hastelloy
$K_{effective}$	1.0136	1.0101	1.0041
Reactivity	1346	995	404
BU fuel	29.3	29.3	29.8
BU blanket 1	3.2	3.1	2.9
BU blanket 2	0.8	0.9	0.3
K_{inf} fuel	1.1251	1.1223	1.1165
K_{inf} blanket 1	0.8993	0.8853	0.8501
K_{inf} blanket 2	0.5617	0.5510	0.4608
Hastelloy captures	1.86E19	2.06E19	2.55E19
Graphite captures	-	1.04E16	-
Leakage	3.14E18	1.87E18	1.78E18

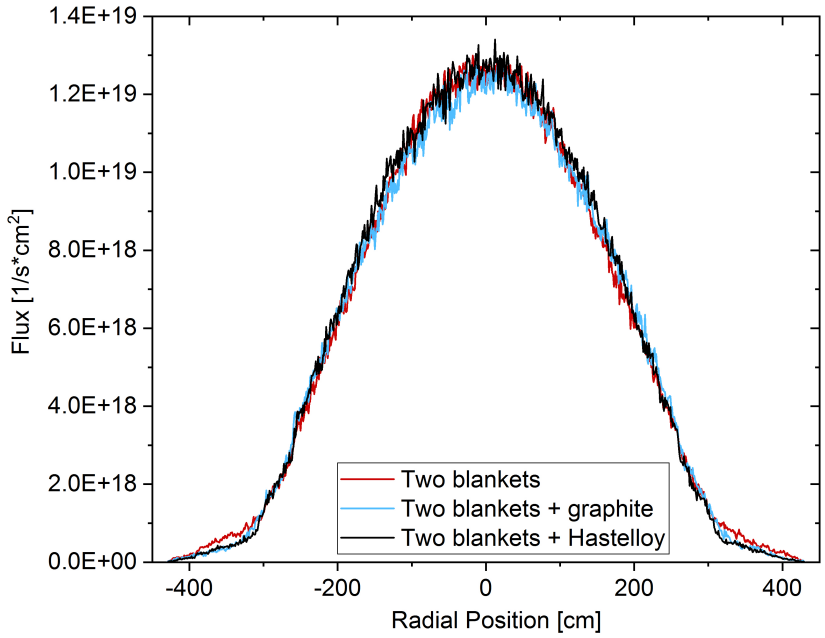

FIGURE 4.18: Radial flux distribution of differently moderated two-blanket designs

4.4.5 Impact of refuelling strategy

In this section, the refuelling scheme adopted was modified for optimization purposes. In all the previous simulations, refuelling was taking place moving the salt from the outside to the inside. The new refuelling scheme, implemented in a two-blanket design, can be seen in the right sketch of Figure 4.19: the salt is transferred from the fresh feed storage to the outer blanket, then to the active core, to the middle blanket and eventually to the spent fuel storage. This design may allow to profit of the low flux periphery of the reactor, the middle blanket region, by burning salt with high content of fissile material.

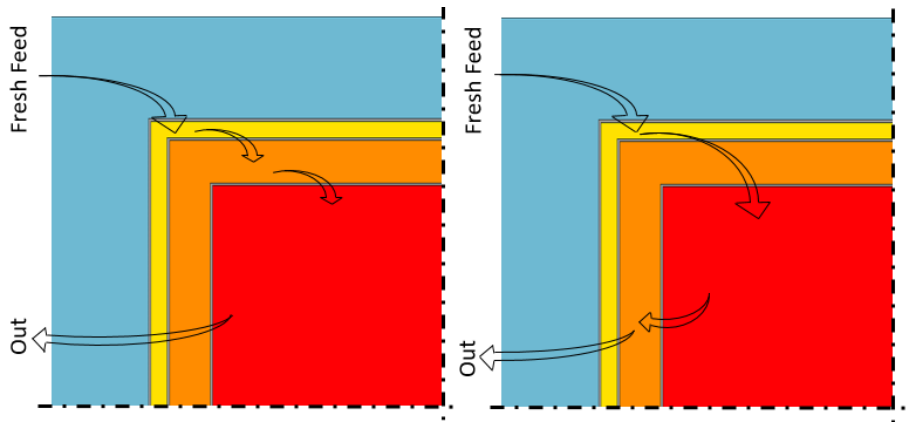

FIGURE 4.19: Old (left) and new (right) refuelling schemes

The reactor simulated was composed of 75 m^3 of active core zone, 50 m^3 of inner blanket and 25 m^3 of outer blanket. The burnup of the discharged

fuel is 33% FIMA. The neutronics comparison of the two refuelling strategies is shown in Table 4.8, while the radial flux of the two cases is presented in Figure 4.20. The new refuelling order is not beneficial to the reactor design simulated, and the equilibrium reactivity becomes strongly negative. With the new scheme, the active core receives only slightly bred fuel. Most of the irradiation takes place in the core region, but a significant part of it happens in the middle blanket. As such, the fuel composition reaches the optimal burnup in the middle blanket, as indicated by the high k_{inf}. A consistent fraction of power is produced in the blanket despite of the neutron flux, which is lower with respect to the centre of the core. On the other side, using salt with high excess reactivity in the periphery increased the neutron flux in that region. Consequently neutron leakage and Hastelloy captures became more significant. However, a new refuelling strategy may be beneficial with a different salt burnup or changing the volume subdivision between core and blankets. In order to assess the optimal refuelling strategy in a multi-fluid layout, further studies would be needed.

TABLE 4.8: Comparison between neutronic performances of two-blanket design with different refuelling schemes

	Old Refuelling	**New refuelling**
$K_{effective}$	1.0006	0.9825
Reactivity	62	-1780
BU fuel	28.6	25.3
BU blanket 1	4.5	7.8
Bu blanket 2	0.5	0.8
K_{inf} fuel	1.1246	1.0854
K_{inf} blanket 1	0.9267	1.1282
K_{inf} blanket 2	0.4984	0.5554
Hastelloy captures	1.71E19	2.00E19
Leakage	3.33E18	4.60E18

4.5 Safety parameters evaluation

Doppler and void safety reactivity effects were calculated for the multi-fluid reactor composed by 100 m^3 of active core region of two blankets of 50 m^3 each. The feedbacks refer to BOC and EOC salt composition at the equilibrium state. Doppler and void effects were calculated separately for the active core region, the inner blanket and the outer blanket. Doppler was computed for nominal and reduced salt density, while void effect was computed for nominal and increased fuel temperature. In the case of liquid fuel, temperature and density effects are tightly connected. Therefore, the combined effect of temperature increase and salt expansion was calculated as well. The Doppler effect was computed increasing the salt temperature by 300 K. According to [39], the salt expansion constant of UCl_3 45% NaCl 55% is 3E-4

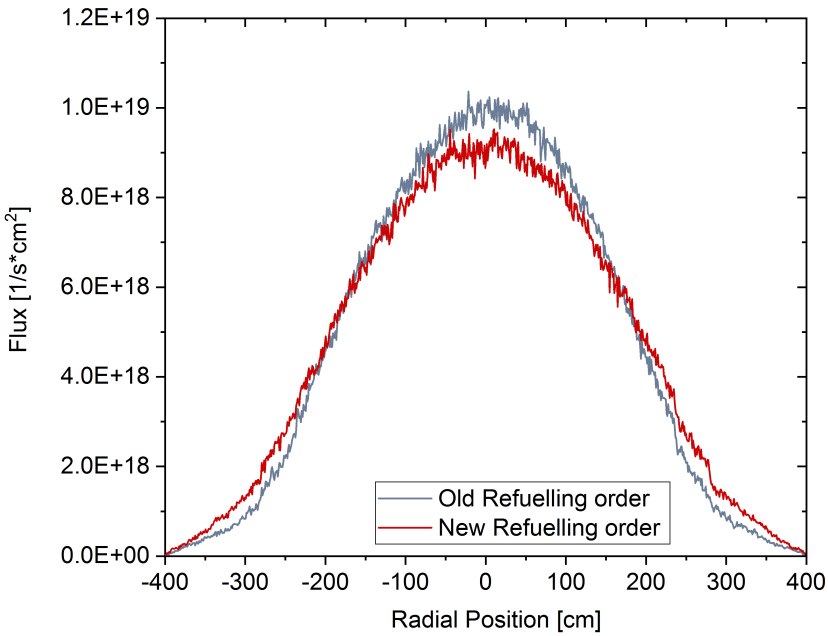

FIGURE 4.20: Radial flux distribution varying the refuelling scheme of a two-blanket design

K^{-1}, which results in a 9% volumetric expansion in case of 300K temperature increase. Obviously, the salt equilibrium composition is different from the fresh salt composition due to the presence of fission products and minor actinides. Therefore, this calculation relies on the assumption that the salt expansion constant does not vary significantly during the transition to equilibrium.

Figure 4.21 and Table 4.9 summarize the Doppler and density effects calculated for each region, as well as the combined effect. Clearly, the intensity of the effects is most significant in the active core region and decreases moving towards outer regions. Therefore, the calculated effects in the outer and sometimes inner blankets have extremely high statistical error. The temperature effect is weakly negative, due to the extremely hard spectrum produced by chloride fuel and shown in Figure 4.22. In a fast reactor, the Doppler effect is the result of two competing processes: the increased resonance captures due to resonance broadening, and induced spectrum hardening into an energy range where U-Pu fission cross-section is higher than the capture cross-section [8]. The harder the neutron spectrum, the less important is the first effect compared to the second one. This is reflected on the decrease of temperature effect in the case of a core with reduced salt density. The void effect is strongly negative because it increases the already high leakage of the system. Increasing the salt temperature, on the other hand, the void effect becomes less negative because the spectrum shift towards higher energies and U-Pu fissions increase compared to captures. The coupled temperature and density effect, which represents a real transient scenario, is the most intense feedback in the active core region. It is additive with respect to the temperature effect for a voided core and the void effect for high temperature fuel. In the two blankets, however, additivity is not respected due to the high

stochastic error produced by Serpent in regions with weak reactivity effects.

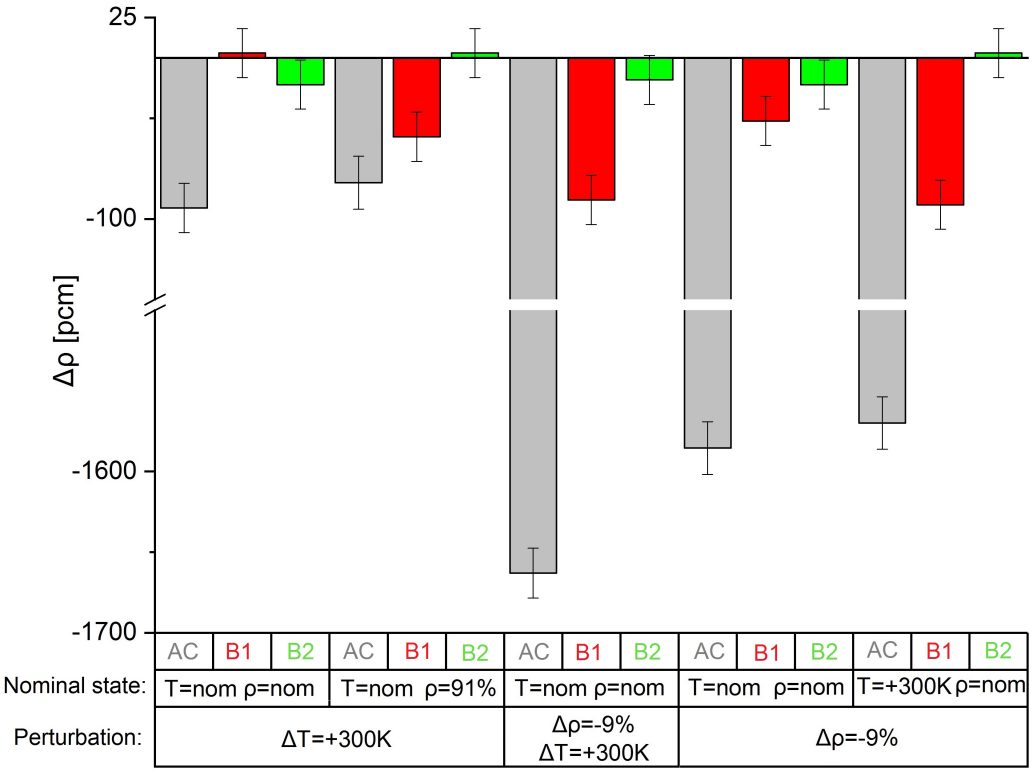

(A) Beginning of Equilibrium Cycle

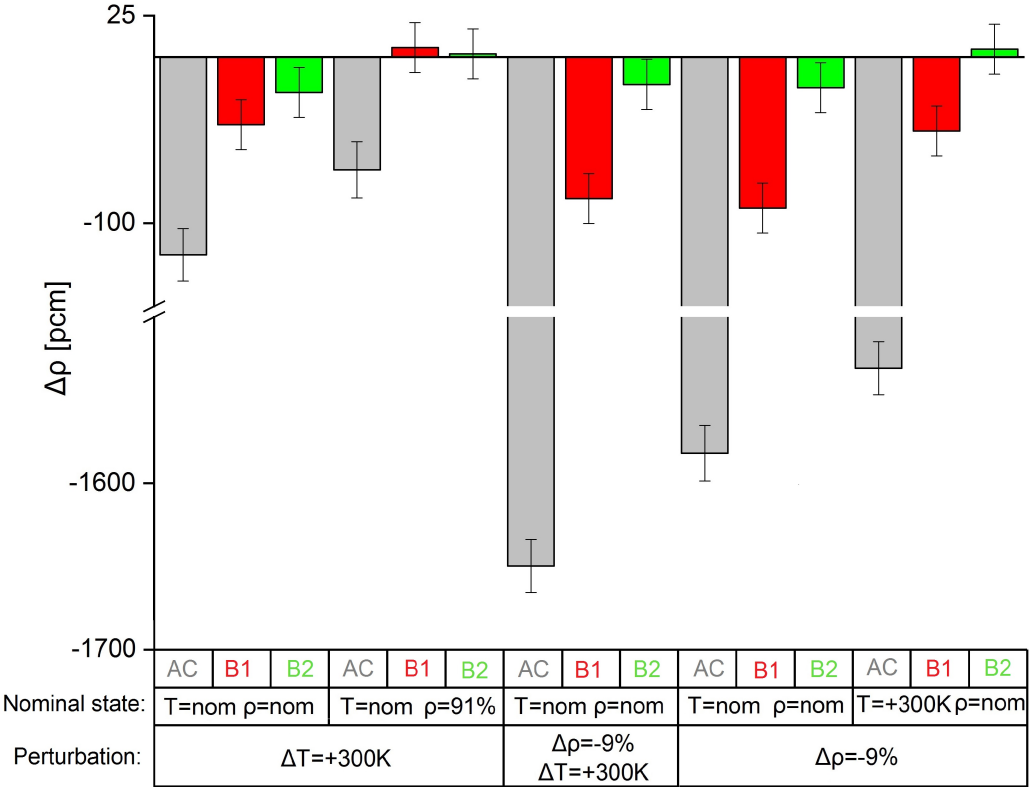

(B) End of Equilibrium Cycle

FIGURE 4.21: Temperature and void effect in active core region (AC), inner blanket (B1) and outer blanket (B2)

The calculated safety feedbacks do not vary substantially from BOC to EOC. The variation is, in almost all cases, within uncertainties. This is related to the neutron energy spectrum, which is roughly identical at BOC and EOC, as shown in Figure 4.22. In reactors operated as converters, the neutron energy spectrum hardens with irradiation due to the build up of minor actinides and fission products. However this does not occur in B&B operation mode, since the salt equilibrium composition is minor actinides rich already at BOC. Additionally in this case fission products, which are strong epithermal absorber and could harden the neutron spectrum, are partially removed from the salt during operation.

TABLE 4.9: Region-wise reactivity effects at BOEC and EOEC

	Active Core		**Blanket 1**		**Blanket 2**	
EFFECT:	**BOC**	**EOC**	**BOC**	**EOC**	**BOC**	**EOC**
Doppler Δ**T= +300 K**	-93	-119	3	-41	-17	-21
Doppler voided fuel (ρ=91%) Δ**T= +300 K**	-78	-68	-49	6	3	2
Density $\Delta\rho$**= -9%**	-1585	-1582	-39	-91	-17	-18
Density hot fuel (T=+300 K) $\Delta\rho$**= -9%**	-1569	-1531	-91	-45	3	5
Combined Δ**T= +300 K and** $\Delta\rho$**= -9%**	-1663	-1650	-88	-85	-14	-16

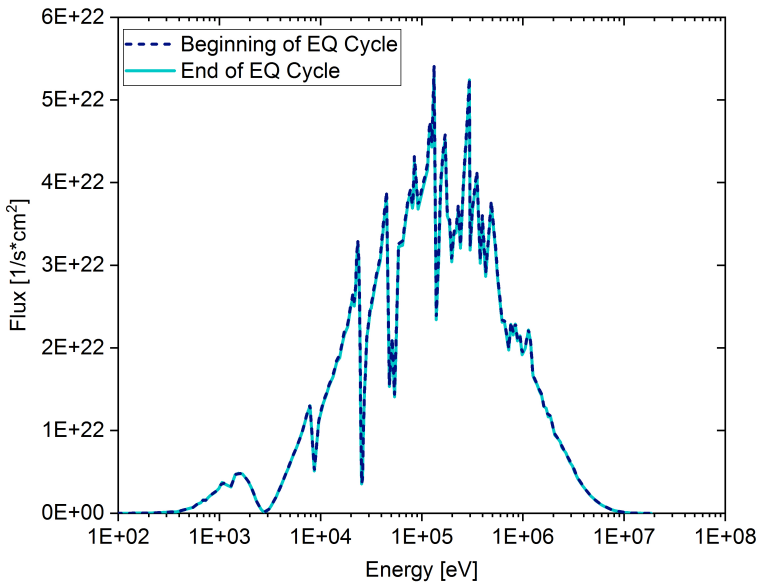

FIGURE 4.22: Neutron energy spectrum at equilibrium

Chapter 5

Summary and Conclusions

This work addresses two advanced nuclear reactors, the European Sodium Fast Reactor and a Breed and Burn Molten Salt Reactor. Both of these systems are Generation IV fast breeders. The ESFR and B&B MCFR can be operated in batches, until they reach an equilibrium state. At equilibrium, parameters such as core reactivity, fuel composition and batch-power are constant from cycle to cycle. Therefore, the equilibrium state is used as a reference to compare and evaluate different reactors performances. Several tools could be utilized to simulate the neutronic behaviour of a reactor at equilibrium. At Paul Scherrer Insitute, codes such as EQL3D, EQL0D and BBP are utilized. For this work, the routine Batch Burnup Procedure (BBP) was applied and expanded. It is a Python routine which automatizes refuelling and safety coefficients mapping. The BBP script calls the Monte Carlo code Serpent2 to perform burnup or transport simulations. It is a versatile routine, which can be applied both to solid and liquid fuel systems. In the case of solid systems, refuelling takes place replacing the most burnt assemblies with fresh ones. In case of liquid homogeneous fuel, refuelling takes place removing a volumetric share of the fuel and replacing it with the same volume of fresh fuel. Safety feedbacks mapping is computed by direct calculations, perturbing locally the selected regions.
The first application of the BBP routine concerns the European Sodium Fast Reactor. It is a large reactor with a power output of 3600 MW_{th}, composed of 216 inner fuel assemblies and 288 outer fuel assemblies, and refuelled according to a six-batch pattern. A radially infinite Serpent model of the ESFR inner core, based on a selection of six assemblies with periodic boundary conditions applied, was created at PSI. Such model was developed to reproduce the ESFR inner core behaviour, and in particular detailed burnup, power and safety coefficients axial profiles, with the high precision of Monte Carlo codes but in a reduced computational time. The results of this model were compared with those from a full core Serpent2 model and a full core ERANOS2.2 model created at PSI. The core reactivity evolution from beginning of life to equilibrium is well reproduced by the reduced Serpent model. The batch-wise burnup and power axial profiles, however, were relatively imprecise. The main reason is that the periodic model does not include the elements, such as control rods and guide tubes, which perturb the radial neutron flux in the full core models. As for the safety feedbacks, the Doppler constant and sodium void effect were calculated. The evolution of the coefficients from first cycle to equilibrium cycle is in good agreement with the results from

ERANOS model. In the case of local coefficients mapping, a precise comparison is hindered by the strong stochastic fluctuations generated by the radially infinite Serpent model. This is particularly true in the case of the Doppler constant. The void effect, which is a stronger effect than Doppler and, as such, is subject to lower statistical noise, shows good agreement with ERANOS results. However, it was demonstrated that several million neutrons per node must be simulated with Serpent to perform safety coefficients mapping. Therefore, if a fine discretization is implemented, each simulation can be extremely resource consuming.
The second application of the BBP routine concerned a Breed and Burn Molten Chloride Fast Reactor. Breed and Burn is a sustainable operation mode in which all the fissile material burnt is bred inside the core. B&B mode allows utilization of fertile fresh fuel, such as natural uranium, enhancing the sustainability of the fuel cycle even in an open once through cycle. The system studied is a pool type, externally cooled, chloride fuelled fast reactor. To be feasible, B&B mode needs an excellent neutron economy; however, chloride salts are fairly transparent to neutrons, thus neutron leakage outside of the reactor is a limitation. In order to overcome the losses due to leakage, a bare single-fluid B&B reactor would need to be extremely large. Therefore, a parametric study aimed at optimizing the reactor dimensions was carried out. At first, the feasibility of the described operation mode was assessed for an infinite core. It resulted that, in the case of a Uranium-Plutonium cycle with continuous non-soluble fission products removal, B&B operation is feasible. The best neutronics performance is achieved when equilibrium burnup of the discharged salt is approximately 30% FIMA. In the case of a cylindrical bare reactor, however, a salt volume of roughly 500 m^3 would be necessary to obtain criticality. The addition of a lead reflector around the active core region allows to shrink the core up to 300 m^3. In a second place, two-fluid operation was introduced through the addition of a breeding blanket around the core. The impact of the active core volume, the blanket volume and the total burnup of the discharged salt at equilibrium was studied. It resulted that the addition of a blanket could largely contribute to shrink the reactor, and that the blanket volume has a larger influence on the performance than the active core volume. With this configuration, a reactor of 175 m^3 was found to be critical. Additionally, different multi-fluid configurations with two and three breeding blankets were introduced. By adding other external blankets, the total leakage from the system is reduced but the parasitic absorption in the structural materials increases. A moderating material and a different refuelling strategy were introduced as well, but did not contribute to enhance the reactor performance. Some safety coefficients such as fuel temperature, density and combined temperature and density effects were calculated regionwise for the two-blanket reactor. All of the feedbacks computed are either negative or very small.

5.1 Outlook

In the IF ESFR simulation, the fine axial nodalization adopted by the infinite Serpent model allowed to distinguish an increase in the fission reaction rate in the last few centimetres of the active core, as described in Appendix B. However, this phenomenon has never been identified by any other fast sodium reactor model. The physics behind this effect should be further investigated to understand whether it is a physical or a fictitious behaviour.
An adapt normalization for the ESFR IF safety feedbacks computed by the infinite Serpent model is hard to define. Additionally, the feedbacks calculated by Serpent were approximately 1.5 times stronger than those from ERANOS, and this disparity has not been well understood yet. How to normalize the safety parameters for an infinite model, and the relation between infinite and finite safety feedbacks require further reasoning.
In the B&B MCFR study, the optimization problem faced is complex and non-linear: the core volume, the number of blankets, the blanket volumes, burnup, the refuelling strategy adopted are only some of the many variables which could influence the reactor performance. Among those variables, the optimal combination is the one that maximizes the excess reactivity at equilibrium and minimizes the size of the reactor. A more sophisticated algorithm that automatizes this parametric study could allow drawing more extensive conclusions.

Acknowledgements

The research conducted was made possible through funding from the Euratom research and training programme 2014-2018 under grant agreement No 754501 (ESFR-SMART project).

For the great support in the realization of this Thesis, I would like to thank my supervisors, Jiri and Konstantin, who dedicated me their time despite of their busy schedule.

My sincere gratitude goes to Professor Prasser for the inspiring lectures, for being an available and fast-responding tutor and for sharing useful advices. A special thank to Professor Pautz and all those involved in the organization of the Nuclear Engineering Master, for the hard work and commitment in guaranteeing such a high level program.

I would like to thank my colleagues for making PSI a more enjoyable place. In particular Rodrigo, for the technical (and moral) support for the Thesis, for being a great IT guy and teaching assistant but especially for sharing stupid Youtube videos with me.

I wish all the best to all the new friends I met in these two years of Swiss life. Thank you for all the beautiful moments we shared, for helping me appreciate Switzerland and making me feel at home despite of the hard times. Even Unterwindisch doesn't feel that bad after all! A special thanks to Andrea, even though he tricked me into watching 12 hours of The Lord of the Rings.

My friends from a lifetime could not be more supportive even in the long distance. Vera, Flavio and Linnea, I've known you for my entire life and you are like family to me. An achievement doesn't feel the same if I'm not celebrating it with you.

Last but not least, my family. My parents and my sisters inspire me and support me, they motivate me to give my best because I would do anything to make them proud.

Appendix A

ESFR fertile blanket discretization

In the IF fertile blanket of the ESFR, breeding takes place during operation. It is important to model such region correctly to predict precisely the amount of actinides generated, which could influence the safety parameters. On the other side, a too fine meshing would increase the CPU time of the simulation. Hence, a proper nodalization of the fertile blanket which accommodates CPU time and accuracy is needed. For this purpose, a radially periodic single pin was modelled. Axially, the fissile zone was divided into 15 cells, while the fertile zone was divided into 1, 5, 10 and 20 cells, as seen in Figure A.1. A burnup simulation was carried out for each nodalization. The pin was burnt for six cycles, each 350 days long. The results were compared, as well as the relative errors calculated using the 20 fertile cells case as a reference.

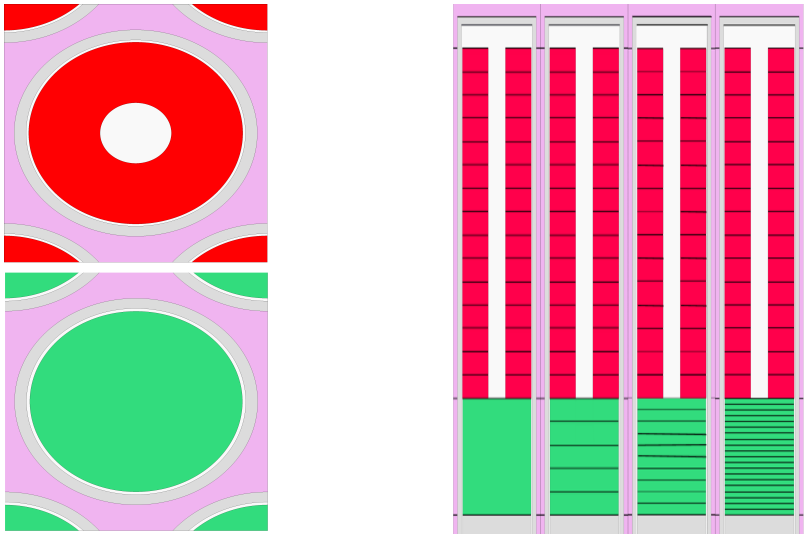

FIGURE A.1: Radially periodic single pin model with different axial nodalizations

The time evolution of burnup and ^{239}Pu atomic density of the fertile region are shown in Figure A.2. The burnup is growing faster than linearly with irradiation time, due to the increasing fissile material content. The burnup trends for the cases with 5, 10 and 20 nodes are very similar, while the case with 1 fertile node departs of almost 4% from the reference case. The relative error of the 5 and 10 nodes cases peaks at the beginning of the simulation. However, the corresponding absolute error is negligibly small. Table A.1 shows the maximum relative error generated in the calculation of some

actinides atomic densities. The error is generally higher for heavier actinides, which are present in a lower concentration in the core. For ^{239}Pu the relative error never exceeds 1.1%. However, it reaches 6% for ^{241}Pu. While the improvement from the 1 node case to the 5 nodes case is noticeable, the difference between 5 and 10 nodes is not. Hence, the fertile region was modelled with 5 axial cells. Each fertile cell results 5 cm high, as the fissile ones.

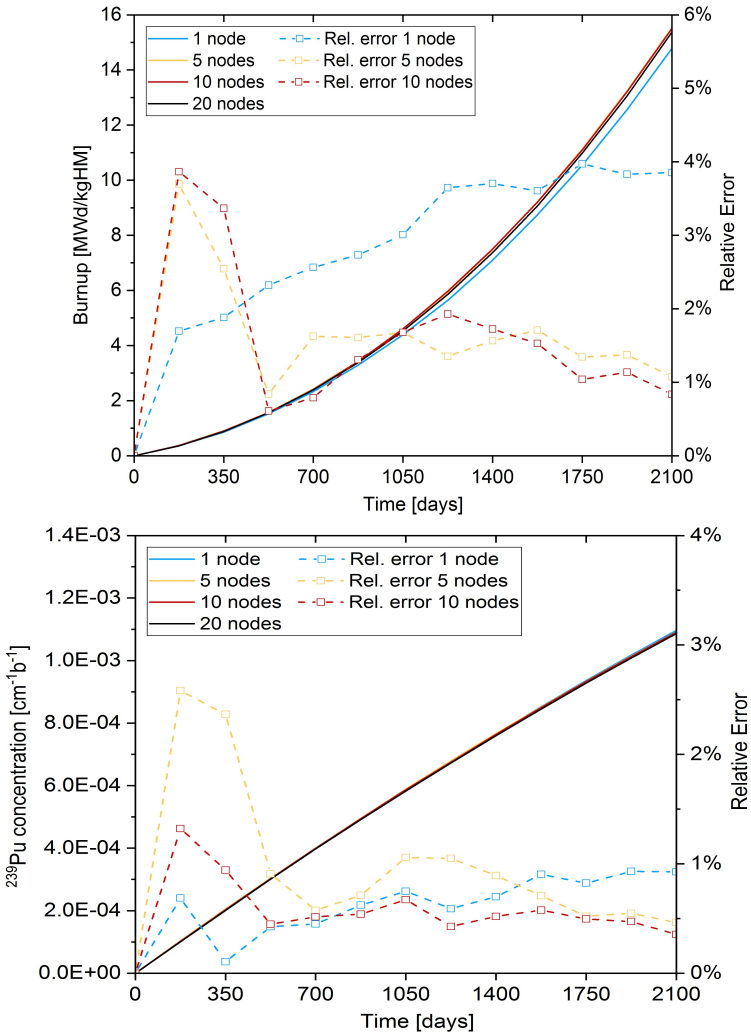

FIGURE A.2: Fertile zone burnup (top) and ^{239}Pu content (bottom) with different nodalizations and relative errors

TABLE A.1: Maximum relative errors in the atomic densities of some actinides in the fertile region of the core; the 20 nodes case is used as a reference

	1 node	**5 nodes**	**10 nodes**
^{239}Pu	0.9%	1.1%	0.7%
^{240}Pu	2.9%	1.8%	1.6%
^{241}Pu	5.8%	3.9%	3.4%
^{241}Am	4.1%	2.5%	2.0%

Appendix B

Behaviour of ESFR core periphery

An anomaly in the burnup and power axial profiles was observed simulating the radially infinite ESFR inner core with the Monte Carlo code Serpent, when a fine axial nodalization was adopted. In the two peripheries of the core, power and burnup increase instead of decreasing as expected. This is particularly evident on top of the core. This effect was further investigated through a radially infinite pin model, analogue to the one presented in Appendix A. At first, a fine axial nodalization of the pin consisting of 40 axial nodes of equal length was adopted. The burnup axial profiles produced are shown in Figure B.1. It can be noticed that burnup steeply increases in the last few centimetres of the core. When coarsening the nodalization to 20 nodes, this behaviour is still visible; however it does not appear when 10 nodes are used, as seen in the detailed view of the burnup profiles on the right of Figure B.1. However, this effect was not observed in any other ESFR model. Generally, full core Monte Carlo models adopt a coarser axial nodalization in order to save computational resources. On the other side, deterministic codes like ERANOS could afford a fine axial nodalization but are imprecise when simulating neutron transport, especially at the boundaries of the model.

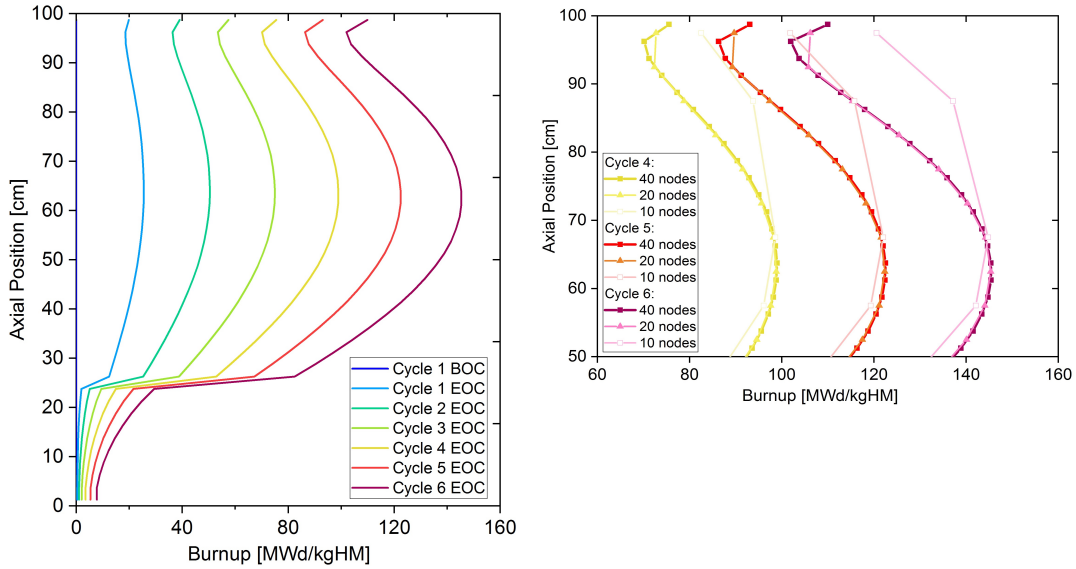

FIGURE B.1: Fine axial burnup profiles of a radially periodic IF pin depleted for six cycles; on the right, a detailed view of some burnup profiles for differently refined nodalizations is shown

The described behaviour does not appear in the axial neutron flux distribution, shown in Figure B.2. At both peripheries of the fuel region, the total flux decreases due to the high leakage.

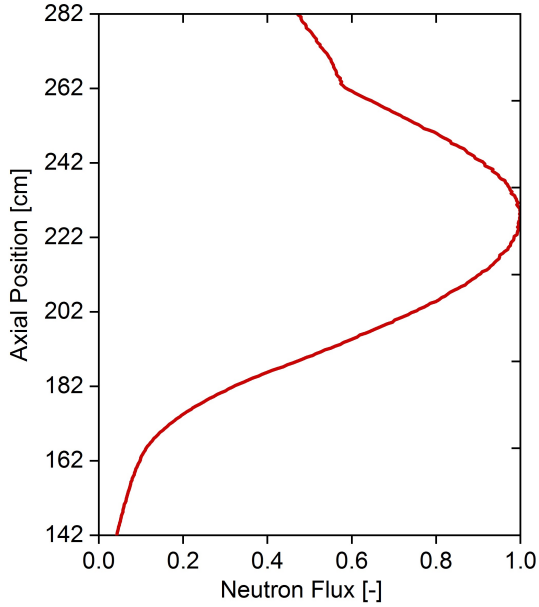

FIGURE B.2: Axial neutron flux in the Serpent infinite pin model; the fuel region is included between 162 cm and 262 cm

The neutron spectrum at the peripheries of the pin fuel region in case of 20 axial nodes is shown in Figure B.3. Node 20 represents the cell on top of the fissile zone while node 1 represents the cell at the bottom the fertile blanket.

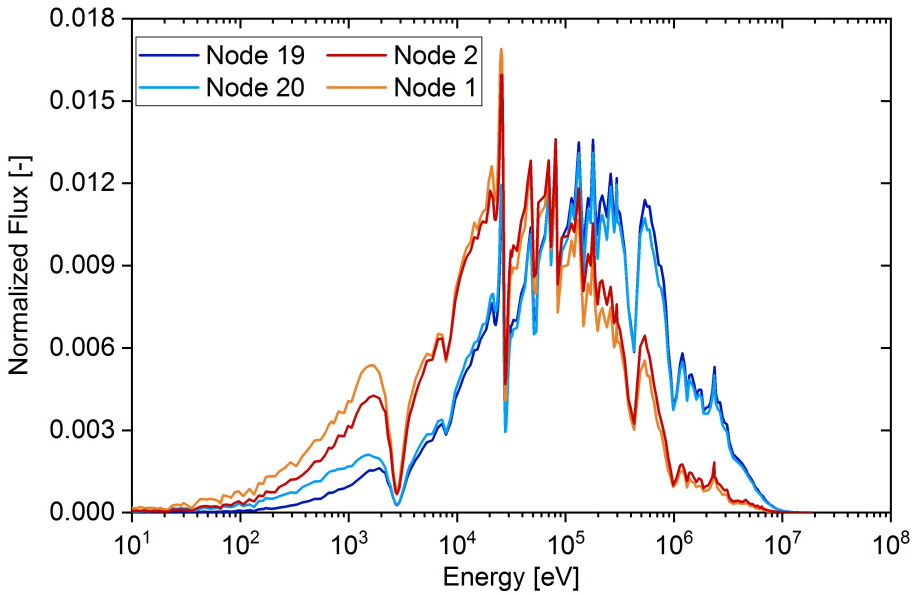

FIGURE B.3: Neutron energy spectra at the two peripheries of the fuel region and in the neighbouring cells

A neutron flux dip at roughly 3 keV can be observed in all the neutron energy spectra. This energy corresponds to a resonance in the elastic scattering cross section of ^{23}Na; 3 keV neutrons are, therefore, likely moderated by the coolant or the sodium plena. For this reason, 3 keV is considered to be the energy boundary between moderated and unmoderated neutrons. The flux at the peripheries, i.e. nodes 20 and 1, is higher than the flux in the respective neighbouring cells in the epithermal energy range below the sodium scattering resonance. On the other side, the flux is higher in nodes 2 and 19 for energies above the sodium resonance. This suggests that the sodium plena at the peripheries of the core act like moderators and reflectors. The induced neutrons thermalization taking place especially at the top of the core results in increased thermal fissions in that zone, as seen in Figure B.4.

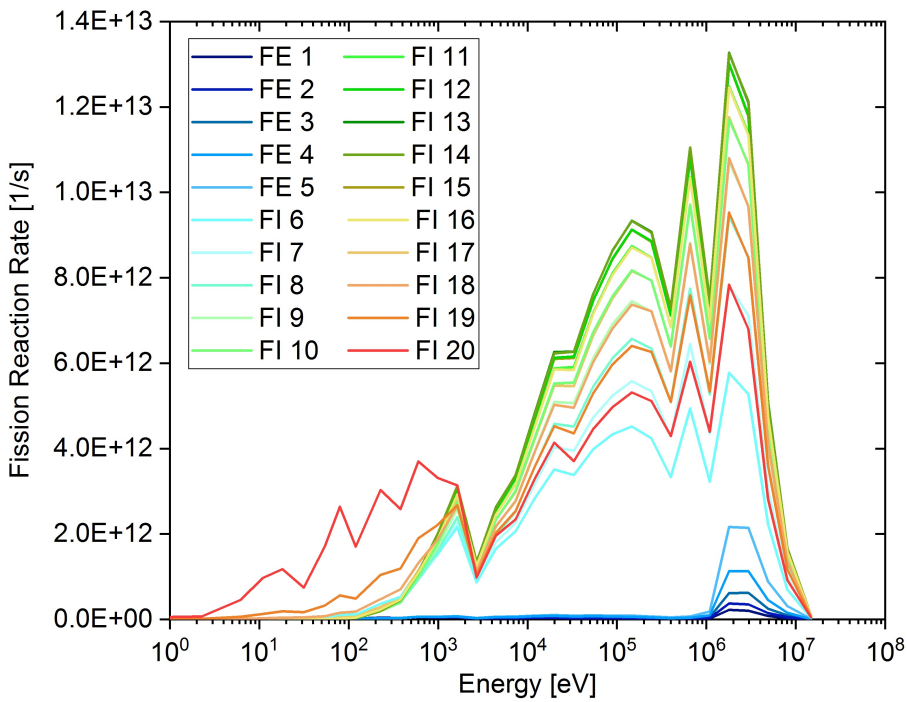

FIGURE B.4: Total fission reaction rate energy spectrum per axial node in a 33 energy groups structure

Similarly, axial fission rate profiles per energy group are displayed in Figure B.5. An energy grid with 33 groups was employed, where group 1 corresponds to the highest energy range and group 33 to the lowest energy range. It can be observed that fast fissions decrease at the top periphery of the core; on the other hand, thermal and epithermal fissions increase steeply in the last few centimetres of the fuel region. The fission reaction rate integrated over all energy groups is represented by the black line in Figure B.5. Overall, the total fissions increase in the periphery, accordingly to the burnup and power profiles observed.
However, the Monte Carlo ESFR full-core models did not employ a fine axial nodalization which could allow to reproduce a similar behaviour. Therefore, there is not other evidence that the observed effect is realistic, and the physics behind this phenomenon should be further investigated. In case this

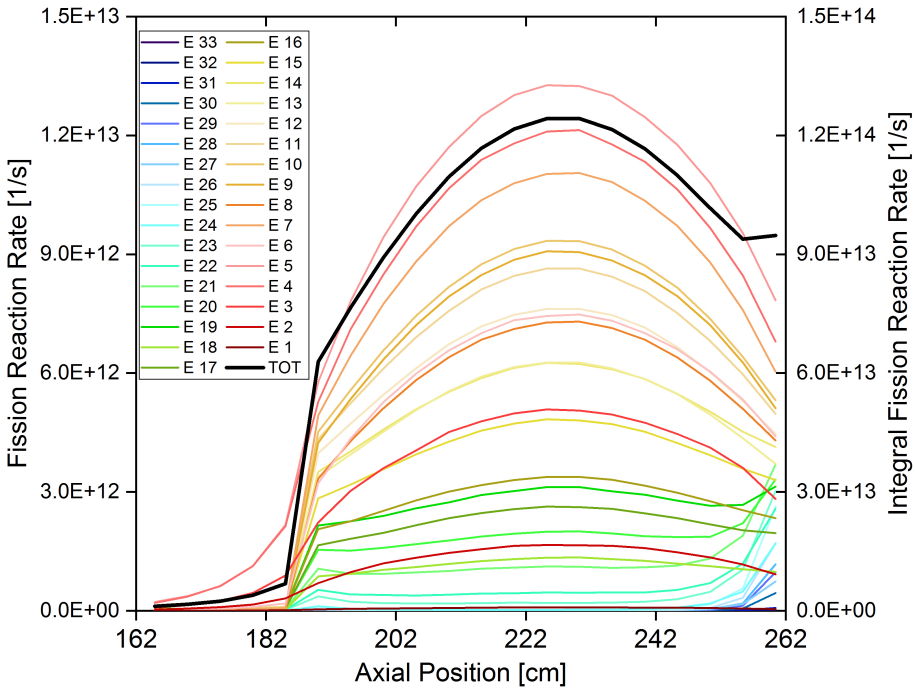

FIGURE B.5: Axial fission reaction rate profiles per energy group; the integral fission reaction rate, coloured in black, refer to the y-axis on the right

behaviour was found to be physical, the dependency of its amplitude on the spatial location in the core, e.g. IF or OF zone, could be assessed.

Appendix C

ESFR safety parameters normalization

Doppler constant and void effect were mapped in the ESFR inner core by a radially infinite Serpent model and a whole-core ERANOS model (see Chapter 3). It resulted that the values calculated by the Serpent infinite model for both Doppler and void were higher than those calculated by the finite ERANOS model by a factor of roughly 1.5. On the other side, Serpent coefficients are comparable to those calculated by ERANOS for the whole-core. In order to understand this phenomenon, an infinite model of a ESFR assembly node was created. The fuel region of an assembly was axially prolonged for 32 meters, and reflective boundary conditions were applied at the two ends. The fuel was homogeneous in the whole model. Radially periodic boundary conditions were applied. Gradually, regions with different heights in the centre of the assembly were perturbed. Two situations were simulated. In one case, the fuel was originally flooded and the perturbation consisted in voiding the sodium inside the wrapper. In the second case, the fuel was originally voided and the perturbation consisted in increasing the sodium density to the nominal value. The two cases are schematically represented in Figure C.1.

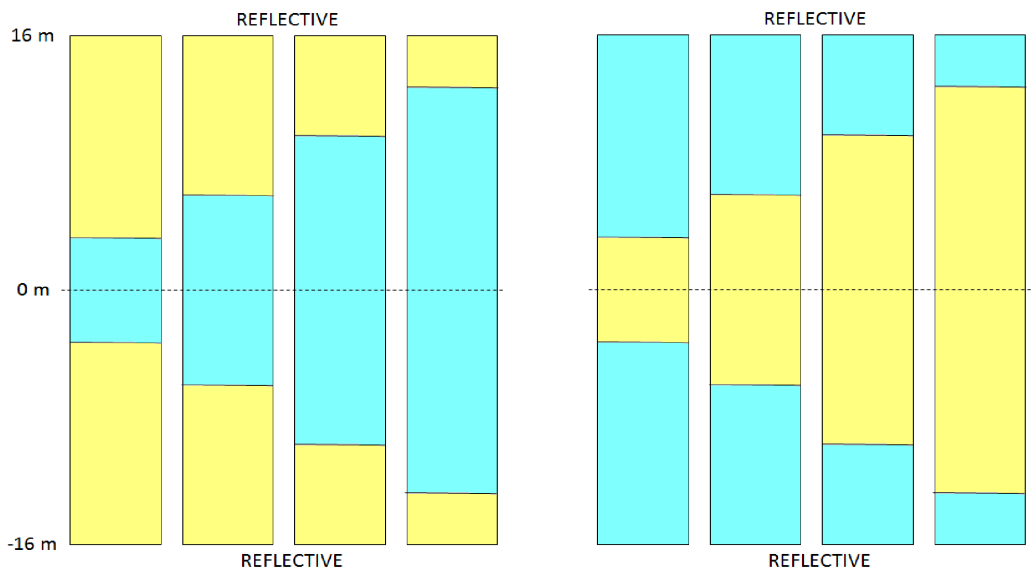

FIGURE C.1: Perturbed regions in the two cases simulated: the blue region represents the voided zone and the yellow region the flooded zone

Since reflective boundary conditions were applied at the top and bottom ends of the model, the reactivity effect generated was expected to be specular. The reactivity effect produced by the perturbations with respect to the completely flooded assembly is shown in Figure C.2.

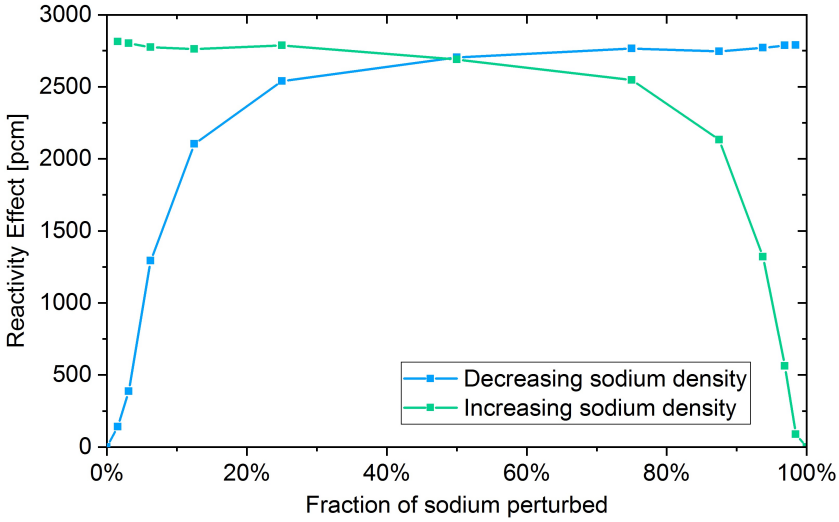

FIGURE C.2: Reactivity effect obtained decreasing and increasing sodium density, for different shares of sodium perturbed

In both cases, the effect reaches saturation when roughly 30% of the assembly is voided. The saturation reactivity effect corresponds to the effect of an infinite core. Before saturation, the reactivity effect increases steeply with the share of sodium voided: when 6% of the total sodium is voided, the reactivity effect is already half of the maximum value. The reason is that when a small region is voided in an infinite assembly, the flux is mostly concentrated in that zone, while it decreases exponentially in the surrounding sodium. Therefore, the importance of the voided region is higher compared to the rest of the assembly, and the reactivity effect grows faster than linearly increasing the voided zone dimensions. A factor of 1.5 between reactivity effect of an infinite core and effect of a finite core is reached when roughly 10% of the sodium is voided, i.e. a region 3 meters long. Surprisingly, this is approximately the diameter of the ESFR inner fuel. In this simplified model, the infinite IF reactivity effect corresponds to the saturated one, the finite IF effect corresponds to roughly 10% of sodium voided, i.e. 3 m, and the whole core effect corresponds to roughly 30% of sodium voided, i.e. 9 m.

Appendix D

ESFR safety parameters mapping

Several feedbacks maps were generated by the radially infinite Serpent model of the ESFR inner fuel and a full core ERANOS model created and utilized at PSI. The feedbacks calculated by both models refer to the ESFR inner core. The Doppler constant and void effect for each of the six batches of the core and different axial nodalizations are shown. In the case of Doppler, 10 and 20 axial nodes were used; in the case of void, 14 and 27 axial nodes including the upper plug and sodium upper plenum were adopted. Especially in the case of the Doppler constant, the maps produced by Serpent suffer from strong stochastic oscillations which make the results impossible to utilize. Since in the ESFR the sodium void effect is stronger than the Doppler coefficient, this behaviour is slightly less visible in the void reactivity maps. On the other hand, ERANOS maps maintain good precision also when a fine nodalization is applied. Therefore, useful information can be inferred from the computed feedbacks maps. For example, in the Doppler constant maps computed by ERANOS, it can be identified that batch IF1 is the freshest in the core while batch IF2 is the most burnt.

D.1 Doppler constant

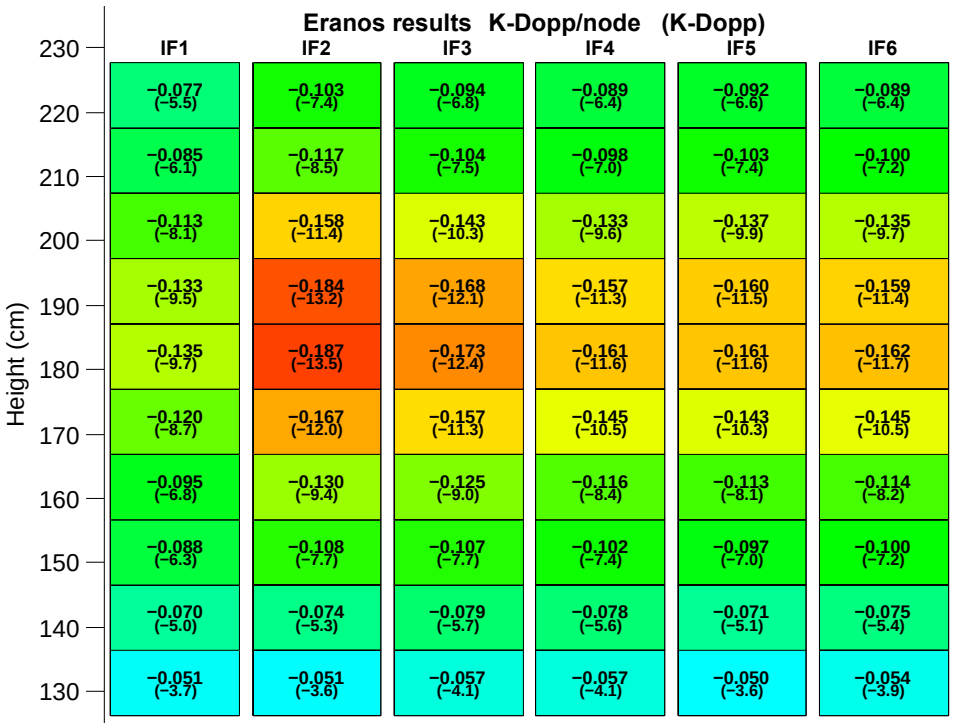

FIGURE D.1: Doppler constant calculated by ERANOS for 10 axial nodes and 6 batches

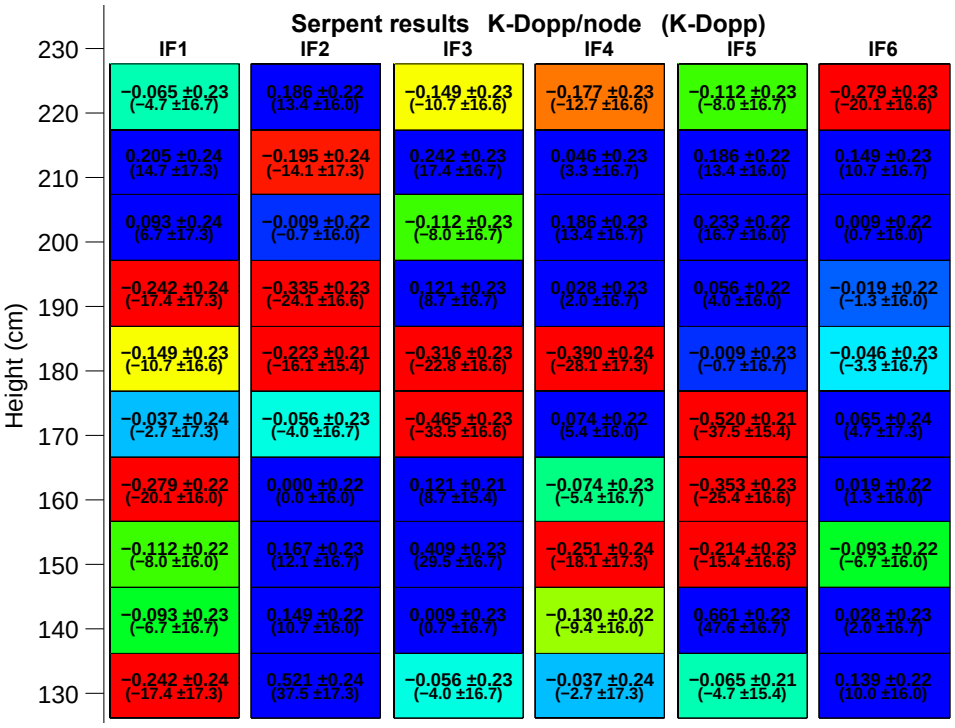

FIGURE D.2: Doppler constant calculated by Serpent for 10 axial nodes and 6 batches

Eranos results K-Dopp/node (K-Dopp)

Height (cm)	IF1	IF2	IF3	IF4	IF5	IF6
230	−0.081 (−2.9)	−0.106 (−3.8)	−0.099 (−3.6)	−0.093 (−3.3)	−0.096 (−3.4)	−0.092 (−3.3)
220	−0.071 (−2.6)	−0.099 (−3.6)	−0.088 (−3.2)	−0.082 (−3.0)	−0.087 (−3.1)	−0.084 (−3.0)
	−0.076 (−2.7)	−0.108 (−3.9)	−0.095 (−3.4)	−0.088 (−3.2)	−0.094 (−3.4)	−0.091 (−3.3)
210	−0.091 (−3.3)	−0.126 (−4.5)	−0.114 (−4.1)	−0.105 (−3.8)	−0.108 (−3.9)	−0.108 (−3.9)
	−0.106 (−3.8)	−0.149 (−5.4)	−0.134 (−4.8)	−0.125 (−4.5)	−0.128 (−4.6)	−0.128 (−4.6)
200	−0.120 (−4.3)	−0.166 (−6.0)	−0.150 (−5.4)	−0.140 (−5.0)	−0.144 (−5.2)	−0.143 (−5.1)
	−0.130 (−4.7)	−0.180 (−6.5)	−0.164 (−5.9)	−0.153 (−5.5)	−0.155 (−5.6)	−0.154 (−5.5)
190	−0.135 (−4.9)	−0.188 (−6.8)	−0.172 (−6.2)	−0.161 (−5.8)	−0.162 (−5.8)	−0.163 (−5.9)
	−0.137 (−4.9)	−0.190 (−6.8)	−0.175 (−6.3)	−0.163 (−5.9)	−0.163 (−5.9)	−0.165 (−5.9)
180	−0.134 (−4.8)	−0.186 (−6.7)	−0.172 (−6.2)	−0.160 (−5.8)	−0.159 (−5.7)	−0.159 (−5.7)
	−0.127 (−4.6)	−0.174 (−6.3)	−0.163 (−5.9)	−0.151 (−5.4)	−0.151 (−5.4)	−0.151 (−5.4)
170	−0.115 (−4.1)	−0.160 (−5.8)	−0.149 (−5.4)	−0.140 (−5.0)	−0.137 (−4.9)	−0.139 (−5.0)
	−0.101 (−3.6)	−0.141 (−5.1)	−0.134 (−4.8)	−0.124 (−4.5)	−0.120 (−4.3)	−0.123 (−4.4)
160	−0.087 (−3.1)	−0.120 (−4.3)	−0.115 (−4.1)	−0.105 (−3.8)	−0.103 (−3.7)	−0.105 (−3.8)
	−0.079 (−2.8)	−0.107 (−3.9)	−0.100 (−3.6)	−0.094 (−3.4)	−0.093 (−3.3)	−0.095 (−3.4)
150	−0.095 (−3.4)	−0.109 (−3.9)	−0.110 (−4.0)	−0.107 (−3.9)	−0.101 (−3.6)	−0.104 (−3.8)
	−0.078 (−2.8)	−0.084 (−3.0)	−0.088 (−3.2)	−0.087 (−3.1)	−0.080 (−2.9)	−0.084 (−3.0)
140	−0.063 (−2.3)	−0.065 (−2.3)	−0.071 (−2.5)	−0.070 (−2.5)	−0.064 (−2.3)	−0.067 (−2.4)
	−0.053 (−1.9)	−0.053 (−1.9)	−0.059 (−2.1)	−0.059 (−2.1)	−0.053 (−1.9)	−0.056 (−2.0)
130	−0.052 (−1.9)	−0.049 (−1.8)	−0.056 (−2.0)	−0.056 (−2.0)	−0.049 (−1.8)	−0.053 (−1.9)

FIGURE D.3: Doppler constant calculated by ERANOS for 20 axial nodes and 6 batches

Serpent results K-Dopp/node (K-Dopp)

Height (cm)	IF1	IF2	IF3	IF4	IF5	IF6
230	0.316 ±0.48 (11.4 ±17.3)	−0.428 ±0.44 (−15.4 ±16.0)	−0.521 ±0.44 (−18.7 ±16.0)	−0.409 ±0.46 (−14.7 ±16.6)	−0.205 ±0.44 (−7.4 ±16.0)	−0.242 ±0.46 (−8.7 ±16.7)
220	−0.576 ±0.44 (−20.7 ±16.0)	0.130 ±0.44 (4.7 ±16.0)	0.409 ±0.48 (14.7 ±17.3)	0.465 ±0.44 (16.7 ±16.0)	−0.223 ±0.46 (−8.0 ±16.7)	0.205 ±0.46 (7.4 ±16.7)
	0.279 ±0.46 (10.0 ±16.7)	0.632 ±0.46 (22.8 ±16.7)	−0.149 ±0.46 (−5.4 ±16.7)	0.019 ±0.46 (0.7 ±16.7)	−0.223 ±0.44 (−8.0 ±16.0)	−0.613 ±0.44 (−22.1 ±16.0)
210	−0.186 ±0.44 (−6.7 ±16.0)	0.353 ±0.44 (12.7 ±16.0)	0.316 ±0.44 (11.4 ±16.0)	0.726 ±0.46 (26.1 ±16.7)	−0.595 ±0.50 (−21.4 ±17.9)	−0.112 ±0.46 (−4.0 ±16.7)
	−0.279 ±0.43 (−10.0 ±15.4)	−0.167 ±0.44 (−6.0 ±16.0)	−0.112 ±0.48 (−4.0 ±17.3)	0.279 ±0.44 (10.0 ±16.0)	0.874 ±0.43 (31.5 ±15.4)	0.205 ±0.46 (7.4 ±16.7)
200	−0.576 ±0.43 (−20.7 ±15.4)	−0.223 ±0.46 (−8.0 ±16.7)	0.149 ±0.48 (5.4 ±17.3)	0.149 ±0.44 (5.4 ±16.0)	0.056 ±0.43 (2.0 ±15.4)	0.093 ±0.43 (3.3 ±15.4)
	−0.056 ±0.41 (−2.0 ±14.7)	0.484 ±0.46 (17.4 ±16.7)	0.577 ±0.48 (20.8 ±17.3)	−0.112 ±0.44 (−4.0 ±16.0)	−0.781 ±0.44 (−28.1 ±16.0)	0.167 ±0.46 (6.0 ±16.7)
190	0.260 ±0.44 (9.4 ±16.0)	−0.297 ±0.43 (−10.7 ±15.4)	0.465 ±0.48 (16.7 ±17.3)	0.037 ±0.44 (1.3 ±16.0)	−0.483 ±0.44 (−17.4 ±16.0)	−0.744 ±0.48 (−26.8 ±17.3)
	0.632 ±0.44 (22.8 ±16.0)	−0.446 ±0.44 (−16.1 ±16.0)	0.688 ±0.46 (24.8 ±16.7)	−0.297 ±0.44 (−10.7 ±16.0)	0.521 ±0.48 (18.7 ±17.3)	0.205 ±0.46 (7.4 ±16.7)
180	0.428 ±0.44 (15.4 ±16.0)	0.819 ±0.45 (29.5 ±16.0)	0.074 ±0.43 (2.7 ±15.4)	−0.093 ±0.48 (−3.3 ±17.3)	−0.093 ±0.46 (−3.3 ±16.7)	0.000 ±0.43 (0.0 ±15.4)
	−0.242 ±0.48 (−8.7 ±17.3)	−0.446 ±0.46 (−16.1 ±16.6)	0.149 ±0.46 (5.4 ±16.7)	−0.297 ±0.43 (−10.7 ±15.4)	−0.242 ±0.46 (−8.7 ±16.7)	0.446 ±0.44 (16.1 ±16.0)
170	0.651 ±0.46 (23.4 ±16.7)	−0.093 ±0.48 (−3.3 ±17.3)	−0.019 ±0.46 (−0.7 ±16.7)	−0.223 ±0.44 (−8.0 ±16.0)	0.000 ±0.46 (0.0 ±16.7)	−0.186 ±0.44 (−6.7 ±16.0)
	−0.037 ±0.44 (−1.3 ±16.0)	−0.855 ±0.41 (−30.8 ±14.7)	−0.112 ±0.44 (−4.0 ±16.0)	0.335 ±0.46 (12.1 ±16.7)	−0.316 ±0.44 (−11.4 ±16.0)	0.093 ±0.44 (3.3 ±16.0)
160	−0.205 ±0.46 (−7.4 ±16.7)	0.353 ±0.44 (12.7 ±16.0)	0.688 ±0.46 (24.8 ±16.7)	−1.189 ±0.48 (−42.8 ±17.3)	−0.539 ±0.43 (−19.4 ±15.4)	−0.130 ±0.43 (−4.7 ±15.4)
	0.260 ±0.44 (9.4 ±16.0)	0.577 ±0.46 (20.8 ±16.7)	0.316 ±0.46 (11.4 ±16.7)	−0.037 ±0.44 (−1.3 ±16.0)	0.465 ±0.41 (16.7 ±14.7)	0.874 ±0.48 (31.5 ±17.3)
150	0.019 ±0.48 (0.7 ±17.3)	0.167 ±0.46 (6.0 ±16.7)	−0.186 ±0.44 (−6.7 ±16.0)	−0.781 ±0.44 (−28.1 ±16.0)	0.465 ±0.46 (16.7 ±16.7)	0.093 ±0.50 (3.3 ±18.0)
	0.967 ±0.45 (34.8 ±16.0)	−0.706 ±0.44 (−25.4 ±16.0)	−1.097 ±0.46 (−39.5 ±16.6)	0.149 ±0.44 (5.4 ±16.0)	−0.056 ±0.50 (−2.0 ±17.9)	0.093 ±0.46 (3.3 ±16.7)
140	0.000 ±0.43 (0.0 ±15.4)	0.242 ±0.52 (8.7 ±18.6)	−0.929 ±0.46 (−33.5 ±16.6)	0.037 ±0.44 (1.3 ±16.0)	0.595 ±0.50 (21.4 ±18.0)	0.800 ±0.46 (28.8 ±16.7)
	0.242 ±0.46 (8.7 ±16.7)	0.316 ±0.44 (11.4 ±16.0)	0.335 ±0.46 (12.1 ±16.7)	−0.613 ±0.46 (−22.1 ±16.6)	−0.130 ±0.44 (−4.7 ±16.0)	1.098 ±0.46 (39.5 ±16.7)
130	−0.056 ±0.44 (−2.0 ±16.0)	−0.465 ±0.43 (−16.7 ±15.4)	0.260 ±0.48 (9.4 ±17.3)	0.484 ±0.46 (17.4 ±16.7)	−0.167 ±0.44 (−6.0 ±16.0)	0.465 ±0.44 (16.7 ±16.0)

FIGURE D.4: Doppler constant calculated by Serpent for 20 axial nodes and 6 batches

D.2 Sodium void effect

Eranos results PCM/kg (PCM)

Height (cm)	IF1	IF2	IF3	IF4	IF5	IF6
300–280	−0.054 (−10.9)	−0.053 (−10.7)	−0.054 (−11.1)	−0.053 (−10.9)	−0.054 (−11.0)	−0.053 (−10.7)
280–260	−0.133 (−27.0)	−0.134 (−27.3)	−0.134 (−27.3)	−0.129 (−26.3)	−0.134 (−27.3)	−0.131 (−26.6)
260–240	−0.331 (−67.3)	−0.354 (−72.0)	−0.303 (−61.5)	−0.296 (−60.1)	−0.342 (−69.5)	−0.307 (−62.4)
240–220	−0.209 (−3.9)	−0.249 (−4.6)	−0.238 (−4.4)	−0.226 (−4.2)	−0.231 (−4.3)	−0.230 (−4.3)
220–200	0.025 (0.7)	−0.033 (−0.9)	−0.036 (−1.0)	−0.021 (−0.6)	−0.008 (−0.2)	−0.010 (−0.3)
200–180	0.441 (12.0)	0.382 (10.4)	0.394 (10.7)	0.400 (10.9)	0.399 (10.9)	0.403 (11.0)
180–160	0.893 (24.3)	0.831 (22.6)	0.780 (21.2)	0.779 (21.2)	0.845 (23.0)	0.773 (21.1)
160–140	1.145 (31.2)	1.084 (29.5)	1.114 (30.4)	1.107 (30.1)	1.090 (29.7)	1.103 (30.0)
140–120	1.170 (31.9)	1.107 (30.2)	1.154 (31.4)	1.145 (31.2)	1.110 (30.2)	1.129 (30.8)
120–100	0.954 (26.0)	0.886 (24.1)	0.883 (24.0)	0.879 (23.9)	0.887 (24.2)	0.848 (23.1)
100–80	0.526 (14.3)	0.438 (11.9)	0.520 (14.2)	0.525 (14.3)	0.451 (12.3)	0.493 (13.4)
80–60	0.144 (3.9)	0.046 (1.2)	0.106 (2.9)	0.122 (3.3)	0.073 (2.0)	0.104 (2.8)
60–40	0.020 (0.5)	0.014 (0.4)	0.023 (0.6)	0.025 (0.7)	0.010 (0.3)	0.018 (0.5)
40–20	−0.010 (−0.3)	0.014 (0.4)	0.006 (0.2)	0.001 (0.0)	0.003 (0.1)	−0.000 (−0.0)

FIGURE D.5: Void Effect calculated by ERANOS for 14 axial nodes and 6 batches

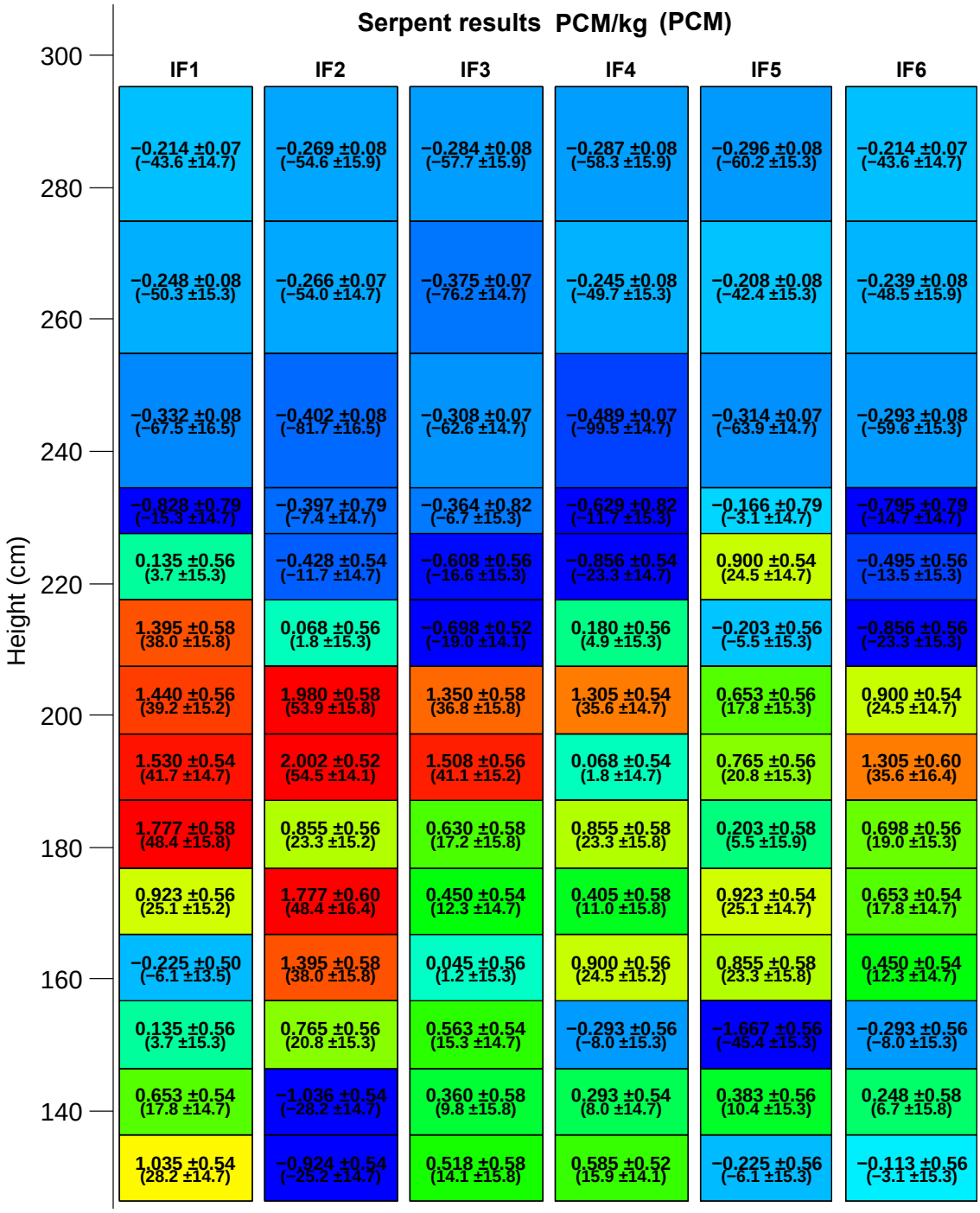

FIGURE D.6: Void Effect calculated by Serpent for 14 axial nodes and 6 batches

Eranos results PCM/kg (PCM)

Height (cm)	IF1	IF2	IF3	IF4	IF5	IF6
300–280	−0.054 (−10.9)	−0.053 (−10.7)	−0.054 (−11.1)	−0.053 (−10.9)	−0.054 (−11.0)	−0.053 (−10.7)
280–260	−0.133 (−27.0)	−0.134 (−27.3)	−0.134 (−27.3)	−0.129 (−26.3)	−0.134 (−27.3)	−0.131 (−26.6)
260–240	−0.331 (−67.3)	−0.354 (−72.0)	−0.303 (−61.5)	−0.296 (−60.1)	−0.342 (−69.5)	−0.307 (−62.4)
240–220	−0.209 (−3.9)	−0.249 (−4.6)	−0.238 (−4.4)	−0.226 (−4.2)	−0.231 (−4.3)	−0.230 (−4.3)
220–200	−0.068 (−0.9)	−0.125 (−1.7)	−0.124 (−1.7)	−0.111 (−1.5)	−0.102 (−1.4)	−0.101 (−1.4)
	0.129 (1.8)	0.071 (1.0)	0.070 (1.0)	0.082 (1.1)	0.092 (1.3)	0.093 (1.3)
	0.337 (4.6)	0.278 (3.8)	0.286 (3.9)	0.294 (4.0)	0.297 (4.0)	0.299 (4.1)
	0.542 (7.4)	0.484 (6.6)	0.499 (6.8)	0.504 (6.9)	0.499 (6.8)	0.505 (6.9)
	0.729 (9.9)	0.671 (9.1)	0.694 (9.5)	0.695 (9.5)	0.682 (9.3)	0.691 (9.4)
200–180	0.885 (12.1)	0.827 (11.3)	0.858 (11.7)	0.856 (11.7)	0.834 (11.4)	0.848 (11.6)
	0.998 (13.6)	0.940 (12.8)	0.979 (13.3)	0.975 (13.3)	0.944 (12.9)	0.962 (13.1)
	1.062 (14.5)	1.004 (13.7)	1.047 (14.3)	1.043 (14.2)	1.006 (13.7)	1.028 (14.0)
	1.074 (14.6)	1.017 (13.9)	1.068 (14.5)	1.060 (14.4)	1.016 (13.8)	1.041 (14.2)
180–160	1.035 (14.1)	0.973 (13.3)	1.035 (14.1)	1.031 (14.0)	0.972 (13.2)	1.004 (13.7)
	0.941 (12.8)	0.877 (11.9)	0.948 (12.9)	0.943 (12.8)	0.875 (11.9)	0.912 (12.4)
	0.800 (10.9)	0.731 (10.0)	0.808 (11.0)	0.806 (11.0)	0.731 (10.0)	0.772 (10.5)
	0.623 (8.5)	0.544 (7.4)	0.625 (8.5)	0.627 (8.5)	0.551 (7.5)	0.593 (8.1)
160–140	0.424 (5.8)	0.330 (4.5)	0.411 (5.6)	0.420 (5.7)	0.347 (4.7)	0.389 (5.3)
	0.222 (3.0)	0.104 (1.4)	0.181 (2.5)	0.198 (2.7)	0.138 (1.9)	0.176 (2.4)
	0.067 (0.9)	−0.008 (−0.1)	0.037 (0.5)	0.049 (0.7)	0.011 (0.2)	0.036 (0.5)
	0.032 (0.4)	0.014 (0.2)	0.030 (0.4)	0.035 (0.5)	0.014 (0.2)	0.026 (0.4)
140–120	0.013 (0.2)	0.018 (0.2)	0.021 (0.3)	0.022 (0.3)	0.013 (0.2)	0.017 (0.2)
	−0.002 (−0.0)	0.023 (0.3)	0.013 (0.2)	0.009 (0.1)	0.009 (0.1)	0.007 (0.1)
	−0.014 (−0.2)	0.017 (0.2)	0.007 (0.1)	0.000 (0.0)	0.004 (0.1)	−0.001 (−0.0)

FIGURE D.7: Void Effect calculated by ERANOS for 24 axial nodes and 6 batches

Serpent results PCM/kg (PCM)

Height (cm)	IF1	IF2	IF3	IF4	IF5	IF6
300–280	−0.214 ±0.07 (−43.6 ±14.7)	−0.269 ±0.08 (−54.6 ±15.9)	−0.284 ±0.08 (−57.7 ±15.9)	−0.287 ±0.08 (−58.3 ±15.9)	−0.296 ±0.08 (−60.2 ±15.3)	−0.214 ±0.07 (−43.6 ±14.7)
280–260	−0.248 ±0.08 (−50.3 ±15.3)	−0.266 ±0.07 (−54.0 ±14.7)	−0.375 ±0.07 (−76.2 ±14.7)	−0.245 ±0.08 (−49.7 ±15.3)	−0.208 ±0.08 (−42.4 ±15.3)	−0.239 ±0.08 (−48.5 ±15.9)
260–240	−0.332 ±0.07 (−67.5 ±14.7)	−0.402 ±0.08 (−81.7 ±16.5)	−0.308 ±0.07 (−62.6 ±14.7)	−0.489 ±0.07 (−99.5 ±14.7)	−0.314 ±0.07 (−63.9 ±14.7)	−0.293 ±0.08 (−59.6 ±15.3)
240–220	−0.828 ±0.79 (−15.3 ±14.7)	−0.397 ±0.79 (−7.4 ±14.7)	−0.364 ±0.82 (−6.7 ±15.3)	−0.629 ±0.82 (−11.7 ±15.3)	−0.166 ±0.79 (−3.1 ±14.7)	−0.795 ±0.79 (−14.7 ±14.7)
220–200	0.495 ±1.16 (6.7 ±15.8)	1.891 ±1.12 (25.8 ±15.2)	−2.433 ±1.21 (−33.1 ±16.5)	0.180 ±1.16 (2.5 ±15.9)	−1.757 ±1.21 (−23.9 ±16.5)	−2.613 ±1.08 (−35.6 ±14.7)
200–180	0.180 ±1.16 (2.5 ±15.9)	0.585 ±1.12 (8.0 ±15.3)	0.810 ±1.08 (11.0 ±14.7)	0.540 ±1.12 (7.4 ±15.3)	−0.495 ±1.16 (−6.7 ±15.9)	0.900 ±1.08 (12.3 ±14.7)
180–160	0.045 ±1.08 (0.6 ±14.7)	−0.766 ±1.08 (−10.4 ±14.7)	−0.180 ±1.21 (−2.5 ±16.4)	−1.577 ±1.12 (−21.5 ±15.3)	0.720 ±1.12 (9.8 ±15.3)	1.801 ±1.12 (24.5 ±15.2)
160–140	−0.270 ±1.12 (−3.7 ±15.3)	−0.450 ±1.12 (−6.1 ±15.3)	0.675 ±1.16 (9.2 ±15.8)	−1.622 ±1.08 (−22.1 ±14.7)	−0.225 ±1.16 (−3.1 ±15.9)	0.630 ±1.21 (8.6 ±16.4)
	−2.568 ±1.12 (−35.0 ±15.3)	1.666 ±1.08 (22.7 ±14.7)	2.160 ±1.12 (29.4 ±15.2)	2.026 ±1.03 (27.6 ±14.1)	2.565 ±1.08 (34.9 ±14.7)	0.360 ±1.08 (4.9 ±14.7)
	1.486 ±1.16 (20.2 ±15.8)	−1.396 ±1.08 (−19.0 ±14.7)	1.171 ±1.08 (15.9 ±14.7)	0.045 ±1.08 (0.6 ±14.7)	−0.090 ±1.12 (−1.2 ±15.3)	−1.441 ±1.03 (−19.6 ±14.1)
	1.035 ±1.16 (14.1 ±15.8)	1.441 ±1.12 (19.6 ±15.3)	2.385 ±1.12 (32.5 ±15.2)	1.396 ±1.12 (19.0 ±15.3)	0.225 ±1.08 (3.1 ±14.7)	0.855 ±1.03 (11.7 ±14.1)
	1.261 ±1.08 (17.2 ±14.7)	0.000 ±1.16 (0.0 ±15.9)	−0.766 ±1.03 (−10.4 ±14.1)	1.351 ±1.08 (18.4 ±14.7)	0.405 ±1.21 (5.5 ±16.4)	−0.180 ±1.12 (−2.5 ±15.3)
	0.270 ±1.16 (3.7 ±15.9)	2.160 ±1.12 (29.4 ±15.2)	−0.180 ±1.12 (−2.5 ±15.3)	0.720 ±1.12 (9.8 ±15.3)	2.160 ±1.03 (29.4 ±14.1)	2.430 ±1.16 (33.1 ±15.8)
	0.000 ±1.08 (0.0 ±14.7)	−0.585 ±1.03 (−8.0 ±14.1)	0.855 ±1.08 (11.7 ±14.7)	0.045 ±1.12 (0.6 ±15.3)	2.160 ±1.21 (29.4 ±16.4)	−0.585 ±1.16 (−8.0 ±15.9)
	0.000 ±1.12 (0.0 ±15.3)	1.621 ±1.16 (22.1 ±15.8)	1.846 ±1.03 (25.1 ±14.1)	1.171 ±1.12 (15.9 ±15.3)	−0.225 ±1.12 (−3.1 ±15.3)	0.090 ±1.12 (1.2 ±15.3)
	−0.045 ±1.12 (−0.6 ±15.3)	2.160 ±1.03 (29.4 ±14.1)	−1.171 ±1.12 (−16.0 ±15.3)	0.225 ±1.12 (3.1 ±15.3)	−0.540 ±1.08 (−7.4 ±14.7)	0.945 ±1.12 (12.9 ±15.3)
	0.900 ±1.12 (12.3 ±15.3)	1.306 ±1.08 (17.8 ±14.7)	−1.441 ±1.16 (−19.6 ±15.9)	−1.036 ±1.12 (−14.1 ±15.3)	−0.721 ±1.08 (−9.8 ±14.7)	−2.388 ±1.12 (−32.5 ±15.3)
	−0.856 ±1.03 (−11.7 ±14.1)	−0.721 ±1.08 (−9.8 ±14.7)	−1.982 ±1.12 (−27.0 ±15.3)	0.720 ±1.08 (9.8 ±14.7)	1.846 ±1.08 (25.1 ±14.7)	−0.901 ±1.12 (−12.3 ±15.3)
	0.225 ±1.12 (3.1 ±15.3)	−2.208 ±1.12 (−30.1 ±15.3)	−1.126 ±1.21 (−15.3 ±16.5)	0.765 ±1.08 (10.4 ±14.7)	0.495 ±1.12 (6.7 ±15.3)	−1.532 ±1.16 (−20.9 ±15.9)
	1.441 ±1.08 (19.6 ±14.7)	2.071 ±1.16 (28.2 ±15.8)	0.315 ±1.08 (4.3 ±14.7)	0.315 ±1.08 (4.3 ±14.7)	−0.360 ±1.16 (−4.9 ±15.9)	−0.721 ±1.12 (−9.8 ±15.3)
	−0.811 ±1.12 (−11.0 ±15.3)	−0.180 ±1.03 (−2.5 ±14.1)	−0.270 ±1.08 (−3.7 ±14.7)	−0.676 ±1.21 (−9.2 ±16.5)	0.270 ±1.12 (3.7 ±15.3)	0.045 ±1.12 (0.6 ±15.3)
	2.115 ±1.08 (28.8 ±14.7)	−3.425 ±1.12 (−46.7 ±15.3)	−1.171 ±1.03 (−16.0 ±14.1)	−0.856 ±1.12 (−11.7 ±15.3)	−0.090 ±1.16 (−1.2 ±15.9)	1.216 ±1.16 (16.6 ±15.8)
	0.225 ±1.12 (3.1 ±15.3)	0.810 ±1.08 (11.0 ±14.7)	−2.298 ±1.16 (−31.3 ±15.9)	−1.351 ±1.08 (−18.4 ±14.7)	0.585 ±1.08 (8.0 ±14.7)	1.306 ±1.16 (17.8 ±15.8)
	0.990 ±1.16 (13.5 ±15.8)	−0.405 ±1.12 (−5.5 ±15.3)	−1.757 ±1.16 (−23.9 ±15.9)	−3.109 ±1.12 (−42.4 ±15.3)	−0.270 ±1.12 (−3.7 ±15.3)	−0.135 ±1.08 (−1.8 ±14.7)

FIGURE D.8: Void Effect calculated by Serpent for 24 axial nodes and 6 batches

Bibliography

1. The Generation IV International Forum. *Generation IV Goals* 2019. https://www.gen-4.org/gif/.
2. Locatelli, G., Mancini, M. & Todeschini, N. Generation IV nuclear reactors: Current status and future prospects. *Energy Policy* **61,** 1503–1520. ISSN: 03014215. http://dx.doi.org/10.1016/j.enpol.2013.06.101 (2013).
3. Lineberry, M. & Allen, T. *The Sodium-Cooled Fast Reactor* in *America's Nuclear Energy Symposium* (Miami, Florida, 2002).
4. Et al. Bettis, E. The Aircraft Reactor Experiment-Operation. *Nucl. Sci. Eng.* **2** (1957).
5. Hombourger, B. A. *Conceptual Design of a Sustainable Waste Burning Molten Salt Reactor* PhD thesis (EPFL, 2018).
6. Vitullo, F., Krepel, J., Kalilainen, J., Prasser, H.-M. & Pautz, A. *Statistical Burnup Distribution of Moving Pebbles in HTR-PM Reactor* in *ICONE26* (London, England, 2018), 1–10.
7. Krepel, J., Pelloni, S., Mikityuk, K. & Coddington, P. EQL3D: ERANOS based equilibrium fuel cycle procedure for fast reactors. *Annals of Nuclear Energy* **36,** 550–561. ISSN: 03064549. http://dx.doi.org/10.1016/j.anucene.2009.01.008 (2009).
8. Krepel, J. & Losa, E. Closed U-Pu and Th-U cycle in sixteen selected reactors: Comparison of major equilibrium features. *Annals of Nuclear Energy* **128,** 341–357. ISSN: 18732100. https://doi.org/10.1016/j.anucene.2019.01.013 (2019).
9. OECD 2006. *Physics and Safety of Transmutation Systems. A Status Report* tech. rep. 3 (2006), 1–120.
10. Krepel, J., Pelloni, S. & Mikityuk, K. Comparison of open and closed U-Pu equilibrium fuel cycles for Generation-IV fast reactors with the EQL3D procedure. *Nuclear Engineering and Design* **250,** 392–402. ISSN: 00295493. http://dx.doi.org/10.1016/j.nucengdes.2012.06.004 (2012).
11. Journet, J., Vambenepe, G., Vergnes, J., Biagi, F. & Sztark, H. *Minor actinides transmutation in oxide fuelled fast reactors* in *Int. Conf. GLOBAL93, Future Nuclear Systems: Emerging Fuel Cycles and Waste Disposal Options,* (Seattle, USA, 1993).
12. Sisl, V., Frybort, J., Krepel, J. & Division, S. *Mixed LEU - Th Initial Core and Running - In Phase for the HTR - PM Reactor* in *Proceedings of HTR* (Warsaw, Poland, 2018).

13. Tomic, G & Krepel, J. *ESFR-SMART core burnup calculation on radially infinite lattice with Monte-Carlo code* in *ICAPP* (2019).

14. Fridman, E. *et al. Initial core performance and burn-up calculations* tech. rep. 754501 (HZDR, CIEMAT, JRC, UPM, IRSN, NNL, PSI, EDF, 2019).

15. Koivisto, T., Hombourger, B. & Krepel, J. *Assessment of waste burning in open cycle of a two fluid chloride MSR* in *ICAPP* (France, Juan-les-pins), 10.

16. Martin, M. V., Aufiero, M., Greenspan, E. & Fratoni, M. Feasibility of a Breed-and-Burn Molten Salt Reactor. *Transactions of the American Nuclear Society* **116,** 3–6.

17. Leppänen, J. *Serpent – a Continuous-energy Monte Carlo Reactor Physics Burnup Calculation Code* tech. rep. (VTT Technical Research Centre of Finland), 157.

18. Pusa, M. & Leppänen, J. Computing the matrix exponential in burnup calculations. *Nuclear Science and Engineering* **164,** 140–150. ISSN: 00295639 (2010).

19. Isotalo, A. E. & Aarnio, P. A. Higher order methods for burnup calculations with Bateman solutions. *Annals of Nuclear Energy* **38,** 1987–1995. ISSN: 03064549. http://dx.doi.org/10.1016/j.anucene.2011.04.022 (2011).

20. Isotalo, A. Comparison of Neutronics-Depletion Coupling Schemes for Burnup Calculations. *Nuclear Science and Engineering* **180,** 286–300. ISSN: 0029-5639 (2015).

21. Isotalo, A. Comparison of Neutronics-Depletion Coupling Schemes for Burnup Calculations–Continued Study. *Nuclear Science and Engineering* **180,** 286–300. ISSN: 0029-5639 (2015).

22. Fiorini, G. L. & Vasile, A. European Commission - 7th framework programme: The collaborative project on European sodium fast reactor (CP ESFR). *Nuclear Engineering and Design* **241,** 3461–3469. ISSN: 00295493. http://dx.doi.org/10.1016/j.nucengdes.2011.01.052 (2011).

23. Mikityuk, K *et al. ESFR-SMART : new Horizon-2020 project on SFR safety* in *IAEA-CN-245-450* (2017), 1–10.

24. Tsige-Tamirat,H. (JRC-IET); Vasile, A. C. *Overview of the ESFR Safety Design Strategy* tech. rep. June (5th Joint IAEA-GIF Technical Meeting/ Workshop on Safety of Sodium-Cooled Fast Reactors, Vienna, Austria 23-24, 2015).

25. Rineiski, A *et al.* Core Safety Measures in Esfr-Smart. *PHYSOR 2018: Reactor Physics Paving The Way Towards More Efficient Systems,* 3401–3412 (2018).

26. Krepel, J., Pelloni, S., Bortot, S., Panadero, A.-l. & Mikityuk, K. *Mapping of Sodium Void Worth and Doppler Effect for Sodium-cooled Fast Reactor* in *ICAPP* **2** (Nice (France)).

27. Rineiski, A., Meriot, C., Coquelet-Pascal, C., Krepel, J. & Fridman, E. *Specification of the new core safety measures* tech. rep. 754501 (KIT, EDF, CEA, PSI, HZDR, 2018).

28. Varaine, F. *et al.* Pre-conceptual design study of ASTRID core. *International Congress on Advances in Nuclear Power Plants 2012, ICAPP 2012* **1,** 572–579 (2012).

29. Kim, Y. I. *et al.* BN-600 full MOX core benchmark analysis. *Proceedings of the PHYSOR 2004: The Physics of Fuel Cycles and Advanced Nuclear Systems - Global Developments,* 249–261 (2004).

30. Darnowski, P. & Uzunow, N. Minor actinides impact on basic safety parameters of medium-sized sodium-cooled fast reactor. *Nukleonika* **60,** 171–179 (2015).

31. LeBlanc, D. Molten salt reactors: A new beginning for an old idea. *Nuclear Engineering and Design* **240,** 1644–1656. ISSN: 00295493. http://dx.doi.org/10.1016/j.nucengdes.2009.12.033 (2010).

32. Hombourger, B. Breed-and-Burn Fuel Cycle in Molten Salt Reactors. *European Physical Journal - Nuclear Sciences and Technologies,* 1–19 (2019).

33. Hombourger, B., Krepel, J., Mikityuk, K. & Pautz, A. *Fuel Cycle Analysis of a Molten Salt Reactor for Breed - and - Burn Mode* in *ICAPP* (Nice (France)), 910–916.

34. Kasam, A. A. *Conceptual design of a breed & burn molten salt reactor* PhD thesis (University of Cambridge, 2018).

35. Kopecky, J, Sublet, J.-C., Simpson, J. A., Forrest, R. A. & Nierop, D. Atlas of Neutron Capture Cross Sections IAEA NUCLEAR DATA SECTION. https://inis.iaea.org/collection/NCLCollectionStore/{_}Public/28/060/28060364.pdf (1997).

36. Aufiero, M. *et al.* An extended version of the SERPENT-2 code to investigate fuel burn-up and core material evolution of the Molten Salt Fast Reactor. *Journal of Nuclear Materials* **441,** 473–486. ISSN: 00223115. http://dx.doi.org/10.1016/j.jnucmat.2013.06.026 (2013).

37. Krepel, J., Hombourger, B., Fiorina, C. & Mikityuk, K. *Comparison of Several Recycling Strategies and Relevant Fuel Cycles for Molten Salt Reactor* in *ICAPP* (Nice (France)), 865–873.

38. Křepel, J. *et al.* Fuel cycle advantages and dynamics features of liquid fueled MSR. *Annals of Nuclear Energy* **64,** 380–397. ISSN: 03064549 (2014).

39. Mourogov, A. & Bokov, P. M. Potentialities of the fast spectrum molten salt reactor concept: Rebus-3700. *12th International Conference on Emerging Nuclear Energy Systems 2005, ICENES 2005* **1,** 444–470 (2005).